Characterisation of Fibrinogen Deposition and its Associations with Neuronal Loss and Microglial Alterations in the Multiple Sclerosis Motor Cortex

Maximillian George Crane

Christ Church

University of Oxford

A thesis submitted for the degree of

Doctor of Philosophy

Michaelmas Term 2025

Abstract

In multiple sclerosis (MS), a chronic inflammatory and demyelinating disease of the central nervous system (CNS), neurodegeneration underlies the gradual accrual of irreversible disability. A key mechanism of this neurodegenerative process is the establishment of persistent low-grade inflammation in the CNS. Fibrinogen, a plasma protein that is part of the acute phase reaction and is integral to the clotting cascade has been demonstrated to trigger microglial inflammatory responses by binding to the CD11b/CD18 receptor. Previous work has demonstrated fibrinogen to be negatively associated with neuronal density in layer 5 of the motor cortex. However, the mechanisms of this, and specific neuronal vulnerabilities, are currently unknown.

This thesis extensively characterises the deposition of fibrinogen in a large cohort of postmortem MS cases. We show that fibrinogen is extremely spatially heterogenous, and that deposition type is crucial to pathological outcomes. By using novel image analysis methods, we have shown that fibrinogen is associated with reduced neuronal density across, with the strongest effects in intermediate sized neurons (91-150μm^2 cell body). Microglial-targeted laser-capture microdissection and proteomics provided insight into the microglial response to fibrinogen in the MS motor cortex, suggesting a shift towards glycolysis, alongside a specific reduction in inhibitory synaptic components (GAD1, GABRB2), as well as the key integrin adaptor kindlin3, and synapse loss-associated protein. Kindlin3 was validated within microglia/macrophages, with positive cells demonstrated to have an altered morphology with shorter, branches

in high fibrinogen cases. Finally, we confirmed at the local scale that fibrinogen variability robustly negatively associates with neuronal density.

Collectively these results demonstrate that the deleterious effects of fibrinogen are present at small scales within cases, and that microglia show a significant phenotypic change which may underlie this. This highlights the crucial need to investigate neurodegenerative processes within microenvironments, and to consider vascular pathology as an essential contributor to this.

Acknowledgements

This thesis represents the culmination of several years of enjoyable work. At times this has not been easy, but as with most things, with the support of friends and colleagues all challenges were surmountable. I am forever grateful for support and encouragement provided throughout this time.

Special thanks to the Medical Research Council Doctoral Training Partnership for funding this work, and to the MS patients who kindly historically donated their brains without which this study would not have been possible. It is my most eager hope that the outcomes of it in some small way contribute to improved experiences for those suffering from MS and other neurodegenerative diseases.

I would like to express my thanks to my supervisor, Professor Gabriele De Luca, whose enthusiasm for neuropathology has been infectious, and whose guidance and mentorship has been invaluable. Thanks too to all current and past members of the De Luca lab, including Adele Smart, Aimee Avery, Alex Waldman, Andrew Lockhart, Buse Ünlü, Jonathan Attwood, Jonathan Pansieri, Margaret Esiri, Marco Pisa, and Sydney Yee, for providing a welcoming and positive environment in which to work. I have enjoyed working with you all very much.

Heartfelt thanks to my parents and family for their support throughout my academic career, and for their continuing support for all my endeavours.

A huge thank you is reserved for Marin Vukšić, without whose humour and support this work would have been much more difficult. I will forever be grateful for the kindness you have shown.

Most importantly, I am exceptionally lucky to have been supported by my partner, Sumana, throughout this work. Without your unshakable belief and optimism this work would not have been possible. It is my only hope that I can show the same support to you as you work to become an exceptional scientist and physician, and in all else you do.

Statement of Originality

I, Maximillian George Crane, declare that the work presented in this thesis is my own. Any contribution made by colleagues is explicitly acknowledged in the thesis.

M. G. Crane
Christ Church, Oxford

Table of Contents

List of figures

List of tables

Abbreviations

MS	Multiple sclerosis
CTCF	CCCTC-binding factor
GWAS	Genome-wide association studies
SNPs	Single-nucleotide polymorphisms
miRNAs	MicroRNAs
tPA	Tissue plasminogen activator
CNS	Central nervous system
CSF	Cerebrospinal fluid
RRMS	Relapsing-remitting MS
SPMS	Secondary progressive MS
PPMS	Primary progressive MS
EDSS	Expanded disability status scale
DALYs	Disability-adjusted life years
MHC	Major histocompatibility complex
EBV	Epstein-Barr virus
NFL	Neurofilament light
EAE	Experimental autoimmune encephalopathy
BBB	Blood-brain barrier
SVD	Small vessel disease
NAWM	Normal-appearing white matter
NAGM	Normal-appearing grey matter
WM	White matter
AD	Alzheimer’s disease
ROS	Reactive oxygen species
FFPE	Formalin-Fixed and Paraffin-Embedded
WSIs	Whole slide images
FOV	Field of view
MCA	Multiple Correspondence Analysis
OLS	Ordinary least squares
ROI	Region of interest
LMM	Linear mixed models
AIC	Akaike information criterion
BIC	Bayesian information criterion
CVD	Cardiovascular disease
SVD	Small vessel Disease
LCM	Laser capture microdissection
GSEA	Gene set enrichment analysis
VIF	Variance inflation factors

Chapter 1 | Introduction

1.1 Fibrinogen

Fibrinogen, a crucial blood-clotting protein, plays multifaceted roles in health and disease that extend far beyond its classical function in haemostasis. Understanding the complex regulation and structure of fibrinogen is essential for appreciating its involvement in pathological processes, particularly in contexts where blood-brain barrier disruption allows fibrinogen to enter the central nervous system. This introduction explores the molecular biology of fibrinogen and its emerging role in multiple sclerosis (MS), where its presence in the brain parenchyma may contribute to neurodegeneration through interactions with local immune cells. By examining fibrinogen's structure, regulation, and pathological roles, we can better understand potential therapeutic approaches for MS and other neurodegenerative conditions where vascular integrity is compromised.

1.1.1 Structure and transcriptional regulation of the fibrinogen genes

Fibrinogen is primarily produced by hepatocytes, with the production of functional fibrinogen protein requiring the coordinated expression of the genes encoding the fibrinogen α, β, and γ chains, the *FGA*, *FGB*, and *FGG* genes respectively. These genes are located as a cluster along an ~65kb stretch of chromosome 4 (4q23-q32)[1]. FGG and FGA share the same orientation towards FGB, which is orientated and transcribed in the opposite direction (3'-5')[1]. Early studies of fibrinogen gene expression in a human liver cancer cell line, HepG2, demonstrated that increased expression of any one fibrinogen chain gene

resulted in a coordinated increase in expression across the other two[2,3]. This tightly coordinated expression is essential for functional fibrinogen production, and has been shown to result from a diverse range of transcription factor binding sites common to the promoters of *FGA*, *FGB*, and *FGG*s as well as local chromatin structure[4,5].

A chromatin loop across the full length of the fibrinogen gene cluster is mediated by cluster-flanking CCCTC-binding factor (CTCF) binding sites that bring regulatory elements of the fibrinogen genes into greater proximity. Loss of one of these CTCF binding sites greatly reduces fibrinogen expression. Although, this chromatin structure is more frequent in hepatocytes, it is not unique to them, and appears to be independent of other transcription factors or cytokines, such as IL6 or TNFα, that are known to increase fibrinogen expression[6].

Binding sites for the transcription factors HNF1 and C/EBP, which are highly expressed in the liver[7–9], are located within the 5'-proximal promoters upstream of *FGA*[10] and *FGB*[11]. Approximately equidistant between FGB and FGA lies a conserved non-coding region with binding sites for C/EBPα and HNF4α, an essential positive regulator of HNF1[12]. This region exhibits enhancer activity for the entire fibrinogen gene cluster[13]. A similar enhancer, located between FGA and FGG, has also been shown to enhance FGA promoter enhancing activity[14].

IL6 response elements are located immediately upstream of the proximal promoters of *FGA* and *FGB*[11,15,16], as well as *FGG*[17]. Importantly the effect of these IL6 response elements is diminished by IL1β. For *FGG*, this mechanism has been demonstrated to occur via IL1β, which inhibits JAK/STAT signalling by

activating p38 and MK2 activity, thereby triggering the phosphorylation and internalisation of the IL6-binding receptor gp130[18,19].

Glucocorticoid response elements have been reported in model systems to induce fibrinogen transcription[20–23]. In human *FGB* a glucocorticoid response element is located between ~-2900 and -1500 base pairs upstream of the transcriptional start site[24], a position notably more distal than that of the IL6 response elements.

Additional regulators of fibrinogen expression have recently been identified. For instance, knockdown of *EEPD1* decreases fibrinogen production in HepG2 cells, whereas knockdown of LEPR, *PDIA5*, *PLEC*, *SHANK3*, and *CPS1* leads to an increase in fibrinogen production[25].

Circulating fibrinogen levels in the population vary considerably (~1.5-4.0 g/L)[26], and show significant variability in heritability (~40%)[27]. It is therefore crucial to appreciate the diverse range of factors capable of influencing the expression of the fibrinogen genes.

1.1.2 Genetic variation and fibrinogen function and circulating levels

1.1.2.1 Congenital fibrinogen deficiency disorders

A corollary of the tightly coordinated expression of *FGA*, *FGB*, and *FGG* is that variation in any one of the fibrinogen genes influences the expression of the other two and alters circulating fibrinogen expression or function. Congenital fibrinogen deficiencies are a group of rare bleeding disorders caused by mutations of the fibrinogen genes. Functionally, these mutations can result in a complete absence

of fibrinogen (afibrinogenemia), reduced fibrinogen levels (hypofibrinogenemia), reduced fibrinogen function despite normal circulating levels (dysfibrinogenemia), or both reduced functionality and circulating levels (hypodysfibrinogenemia)[28]. The range of causative mutations for congenital fibrinogen deficiency disorders has expanded substantially, with the number of validated mutations growing from 170 in 2000 to 1023 as of 2024, as catalogued by the European Association for Haemophilia and Allied Disorders Coagulation Factor Variant Database[29,30].

1.1.2.2 Single-nucleotide polymorphisms

Large scale genome-wide association studies (GWAS) have identified single-nucleotide polymorphisms (SNPs) across a wide range of genes that correlate with circulating fibrinogen levels, with significant differences in the prevalence of these SNPs among diverse populations. The largest GWAS of plasma fibrinogen levels to date identified SNPs in 54 genetic loci associated with varying concentrations of fibrinogen[31]. Within the fibrinogen genes, the rare missense mutation of rs14868582 in *FGG* exerts the largest effect and is liked with lower circulating fibrinogen concentration. Outside these genes, a strong association was observed for rs149290349, a missense mutation in *ZFP36L2*, that is associated with increased fibrinogen levels. Notably, 5 SNPs with minor allele frequencies of at least 10% were found to be more common in populations of African ancestry. Despite the large scale of this study and others[32], the currently identified SNPs only explain about 4.8% of the variance in circulating fibrinogen levels.

1.1.3 Epigenetic variation and circulating fibrinogen levels

An epigenome-wide association study of cytosine-phosphate-guanine methylation in 18,037 individuals identified 83 methylations sites across 61 loci associated with circulating fibrinogen levels[33]. Many of these loci are linked to inflammatory pathways. For example, hypomethylation of *SOCS3,* a gene that may act as a negative regulator of STAT3[34], showed the strongest association with increased circulating fibrinogen levels. Although current data on epigenetic influences are limited, it is likely that epigenetics will play an important role in explaining the variance in fibrinogen levels observed across populations.

1.1.4 Post-transcriptional regulation of fibrinogen genes

MicroRNAs (miRNAs) have been shown to influence the expression of coagulation factors in the human liver[35]. Fort et al[36] demonstrated that in HuH7 hepatoma cells that at least 27 miRNAs can modulate fibrinogen expression post-transcriptionally, altering protein levels by between -63% and 129%. In this model, 23 of the miRNAs reduced fibrinogen production. Beyond their direct action on fibrinogen synthesis, miRNAs may also regulate fibrinogen levels indirectly via enhancers or repressors of fibrinogen transcription. For instance, miR-18a, whose production is induced by IL6 and STAT3 activity, has been proposed to enhance IL6-mediated increases in fibrinogen production, partly through the inhibition of the STAT3 inhibitor PIAS3[37].

1.1.5 Fibrinogen chain isoforms

Two major splice variants of fibrinogen are recognised: the *FGA* alternate product (αEC), and the more thoroughly studied *FGG* alternate product (γ').

αEC is a splice variant that arises from the splicing of exon V of *FGA*, resulting in an extended α chain with a distinct C terminus globular region, accounting for ~1% of circulating fibrinogen molecules in humans[38]. Functionally, αEC differs from the more common α chain, influencing fibrin fibre structure within clots and potentially altering their mechanical properties[39] and integrin-binding capacity[40].

The γ' variant is generated via polyadenylation-mediated substitution that replaced the 4 terminal amino acids of *FGG* exon 10 with 20 amino acids from intron 9, producing an elongated carboxyl terminus[41–43]. Under normal conditions, γ' comprises ~15% of circulating fibrinogen monomers[44]. However, γ' expression increases more markedly in response to IL6 stimulation compared with the ordinary γ chain[45], and the proportion of γ' within fibrin clots affects clot properties, with higher γ' levels reducing fibrinolysis[46]. The functional relevance of γ' in clot structure will be explored in more depth in later sections.

1.1.6 Fibrinogen protein structure

Fibrinogen is assembled in a stepwise manner in the endoplasmic reticulum. Initially, individual fibrinogen chains form Aα-γ and Bβ-γ complexes via disulfide bonds. The subsequent addition of a third chain forms $(A\alpha B\beta\gamma)_1$ half-molecules, with the pathway involving Bβ-γ to $(A\alpha B\beta\gamma)_1$ being predominant, while the Aα-γ complexes largely serve as a surplus pool[47]. The functional fibrinogen hexamer,

which circulates in the blood, is generated by N-terminal interactions that dimerise these half-molecules, resulting in a symmetrical hexamer approximately 45 nm in size and weighing around 340 kDa[48–50].

Traditionally, fibrinogen is described as a coiled-coil molecule, with the N-terminus located centrally in the E region, and the C terminal globular domains extending outwards. In the hexamer, the Bβ and γ chains form βC (knob-B) and γC (knob-A) nodules in the D regions. The C-terminal globular domain of the Aα chains comprise an unstructured αC connector and partially structured αC domain that is flexible enough to facilitate intra- and inter-hexamer interactions. Consequently, the overall structure of the hexamer can be described as trinodular, with a D-E-D configuration[4,51].

1.1.7 Proteolytic processing of fibrinogen and fibrin formation

Fibrinogen is cleaved by thrombin, which removed the small fibrinopeptides Fpa (16 amino acids) and FpB (14 amino acids) from the N termini of Aα and Bβ chains. This cleavage exposes 4 central knobs (2 A, 2 B) that interact with corresponding 'holes' in the D domains of adjacent fibrinogen monomers, thereby promoting the formation of half-staggered protofibrils[4,51,52]. Protofibril formation is influenced by local mechanical forces, pulling forces of up to 40pN cam strengthen the A-knob:A-hole interaction[53], and by ion binding, high-affinity calcium binding, for example, further strengthens this A-knob:A-hole bond[54]. Protofibril formation is therefore responsive to diverse local environments. Protofibrils undergo lateral aggregation to from fibrin fibres[55], a process that is enhanced by the αC domains[56–58].

In addition to lateral aggregation and lengthening of fibrin fibres, fibre branching is required for the formation of a fibrin clot. Fibre branching may occur via trimolecular junctions (where a protofibril binds the end of another through a single γC nodule)[59], or via tetrameric junctions (where 2 protofibrils aggregate laterally before diverging into two separate fibres)[60]. These processes, lateral aggregation and branching of fibres, are likely to represent competing yet complementary mechanisms that adapt clot formation to local environmental conditions.

Importantly, this thrombin-mediated process is strongly regulated at a local level. For instance, the inhibition of thrombin by circulating antithrombin and tissue factor pathway inhibitor ensures that thrombin generation via the coagulation cascade only occurs when thromboplastin (tissue factor) on subendothelial pericytes and fibroblasts binds factor VII, thereby initiating factor X activation and subsequent thrombin production[61].

1.1.8 Structural properties of fibrin networks

Fibrin plays an essential role in the clotting response by providing mechanical stability and a suitable surface for further reactions. Individual fibrin fibres are highly extensible and elastic, and they become stiffer when strained[62]. Covalent cross-linking of fibrinogen α and γ chains, to form γ-γ and α-α dimers by FXIIIa transglutaminase activity[63], further increases fibrins resistance to stress by increasing stiffness via compaction of fibres[64] and stabilising branch points to reduce rupturing[65]. Each type of dimer may influence fibre properties in nuanced

ways; for example, α-α dimers increase both elasticity and stiffness, while γ-γ dimers primarly enhance stiffness but may reduce extensibility[66].

The structural properties allow fibrin networks to reorient, align binding sites, and deform without incurring structural damage - properties that are crucial for clots functioning in dynamic environments[51,67].

1.1.9 Fibrinolysis

Fibrin not only provides the matrix for clot stability but also serves as a substrate for its own degradation, a process which is primarily mediated by plasmin. Tissue plasminogen activator (tPA) and plasminogen colocalise on fibrin allowing activation of plasminogen[68]. Plasminogen is conformationally regulated, with its binding to fibrin proposed to expose the cleavage site Arg561, and pro-activation site Lys77 for activation, allowing tPA or other enzymes such as urokinases to convert plasminogen to plasmin[69].

Once active, plasmin cleaves fibrin fibres transversely[56,70,71]. Mathematical models of simple fibre degradation suggest plasmin's action along protofibrils may be processive[72], and that it is likely that fibrin cleavage also triggers longitudinal sliding that pulls fibres apart due to inherent tension of the structure[73]. Modelling also predicts that cleavage of fewer than 50% of protofibrils across a fibre can be sufficient to destabilise a fibre, although these mechanisms require experimental validation[74]. The transverse cleavage of fibrin fibres results in a

variety of degradation products, many of which have immunomodulatory properties[75].

1.1.10 Factors influencing fibrin network properties

The properties of protofibrils and fibrin fibres are influenced by a variety of factors, including the concentration of thrombin during fibrin formation and the proportion of γ' within fibres. Fibres high of γ', or those produced in high thrombin conditions, tend to reduce the packing density of protofibrils, resulting in lower stiffness, which may lead to mechanically weaker clots[76]. Conversely, thicker fibres, often produced under low thrombin conditions, form rougher, more permeable fibrin networks that are susceptible to fibrinolysis, and less effective in stopping bleeds. In contrast, thinner fibres generated under high thrombin conditions form denser networks that are more resistant to fibrinolysis[77]. This adaptability of fibrin to form clots with varying biomechanical properties likely reflects an evolutionary response to the need for caried clot characteristics in different physiological contexts.

1.1.11 Immunomodulatory functions of fibrinogen and fibrin

Both, fibrinogen and fibrin are recognised to have promotive roles in immune cell activation. Fibrinogen monomers are relatively poor ligands for the CD11b/CD18 integrin receptor, which is widely expressed on immune cells. However, the formation of fibrin exposes a cryptic epitope that binds to CD11b/CD18 with high affinity[78,79]. Additionally, fibrinogen can bind to TLR4, a receptor highly expressed by monocytes and tissue-resident macrophages such as mciroglia[80,81], thereby

activating a diverse range of immune cells including monocytes[80–82], neutrophils[83,84], and eosinophils[85].

Beyond these direct interaction with immune cells, fibrinogen acts as a bridging molecular via its interaction with ICAM1. This interaction provides a mechanism for monocyte adhesion to the vascular endothelium[86]. The immunomodulatory capabilities of fibrinogen become particularly relevant in the context of MS, where disruption of the blood-brain barrier permits fibrinogen entry into the central nervous system, triggering immune cell activation. This link between vascular dysfunction and immune activation represents a crucial point where fibrinogen may influence disease progression. Understanding MS pathology and epidemiology is therefore essential for contextualising fibrinogen's potential role in the disease process. The relevance of this capacity to interact with immune cells will be explored throughout this thesis, primarily in the context of MS and other neurodegenerative diseases.

1.2 Multiple sclerosis

Multiple sclerosis is a chronic inflammatory disease of the central nervous system (CNS) that is characterised by both demyelinating and neurodegeneration. It results from a complex interplay between genetic predisposition and environmental exposures. MS profoundly impacts patients' lives, often causing significant disability over the lifespan and imposing a considerable economic burden[87].

1.2.1 Natural history of multiple sclerosis

MS typically presents in the early 30s[88], although up to 10% of patients may develop symptoms before the age of 18[89]. Diagnosis is primarily based on the McDonald criteria, which emphasise the dissemination in time and space of inflammatory demyelinating lesions within the CNS and the detection of cerebrospinal fluid (CSF)-specific oligoclonal bands[90].

At diagnosis, ~85-90% of patients show a relapsing-remitting MS phenotype (RRMS), characterised by episodes of acute neurological dysfunction (relapses) interspersed with reduction in neurological dysfunction and relative stability (remission). Relapse rates are more frequent in the early stages of the disease and gradually decrease over time[91]. Importantly, the number of early relapses in RRMS does not correlate well with long-term disability[92,93]. In contrast, the recently described phenomenon of silent progression or progression independent of relapse activity is associate with poorer long-term outcomes[93,94]. Lesion location, however, appears to be a significant predictor for long-term disability worsening[95]. Over time, RRMS patients may transition to a secondary progressive MS (SPMS) phenotype, which is characterised by a gradual accumulation of disability in the absence of relapses. Although historically around 50% of RRMS patients were thought to convert to SPMS[88], the widespread use of modern disease-modifying treatments may have reduced this rate[93,95].

The remaining ~10-15% of patients present with primary progressive MS (PPMS), which is marked by a progressive clinical course with few or no relapses. PPMS typically shows a later age of onset of ~40 years, and is extremely rare in paediatric populations[96]. The low number of PPMS cases makes it challenging to

define the natural history of the disease, however, recent data from a German cohort of patients indicate that disability accrues slowly, with expanded disability status scale (EDSS) exceeding 4.0 by 6.9 years – and that 33.3% of patients receive a disability pension within a decade[97]. In addition to accumulating disability, MS has been associated with reduced life expectancy[98], with excess mortality becoming evident ~20 years after onset[99].

1.2.2 Epidemiology of multiple sclerosis

The most recent global burden of neurological disease study[100] shows that ~1.9 million people suffer from MS worldwide, with the burden of associated disability amounting to roughly 973,000 disability-adjusted life years (DALYs). Between 1990-2021, the prevalence of MS increased by ~88%, while DALYs increased by ~70% - a trend that likely reflects improvements in clinical care for MS, including the introduction of modern disease-modifying therapies[101,102].

MS epidemiology is complex, with a highly skewed prevalence towards western European ancestry, high female-to-male sex ratio, local discrepancies, and a persistent latitude gradient. No single factor underpins these phenomena; rather, MS risk arises from a complex multifaceted interaction between genetic and environmental factors.

MS displays an uneven global epidemiological pattern, with populations of western Europe ancestry showing high prevalence rates ranging from ~100 to 316 per 100,000[103104]. In regions outside western Europe, individuals of western European descent still show a higher prevalence than the local population; for example in New Zealand the overall prevalence is ~72 per 100,000, but among

those of Maori ancestry, it is ~20 per 100,000[105,106]. In Japan, prevalence is ~23 per 100,000[107]. Recent studies have demonstrated that genetic ancestry is a primary determinant of MS risk. Certain immunogenetic variants in the major histocompatibility complex (MHC) region e.g. HLA DRB1*1501, which emerged under positive selection against pathogens like tuberculosis during the Yamnaya migration from the Pontic-Caspian steppe into western Europe ~5000 years ago, are now recognised as major contributors to MS susceptibility[108–110].

Latitude, serving as a proxy for ultraviolent radiation exposure and, by extension, endogenous vitamin D levels, is strongly associated with both MS prevalence and age of onset. Each degree of increasing latitude is associated with an increase of ~4.3 per 100,000 in age-standardised prevalence[111]. Among individuals of predominantly European ancestry, residing between latitudes of 19.0-39.9 is associated with a onset that is, on average, 1.9 years later than those living between latitudes 50.0-56.0[112].

Of all major neurological diseases, MS has the highest female-to-male ratio[100] (currently this ratio is ~3.0:1.0)[104]. Several studies report an increasing ratio over time in RRMS/SPMS[113,114], with one study linking this to increased urbanisation[115]. However, other studies, even within relatively similar geographic areas, have not reported this trend[116,117]. Notably, in contrast to RRMS/SPMS, the sex ratio in PPMS is much closer to 1.0:1.0[118], suggesting differing underlying susceptibility mechanisms. Overall, the female-to-male ratio in MS appears to increase over time, and decrease with latitude[119], exemplifying the complex interplay between genetic and environmental factors in MS susceptibility.

1.2.2.1 Risk factors associated with multiple sclerosis susceptibility

A variety of environmental and genetic factors have been robustly demonstrated to increase MS risk, with factors often displaying interaction effects that further heighten susceptibility[120].

Prior Epstein–Barr virus (EBV) infection, for instance, is associated with an approximately 32-fold increase in MS risk and is present in over 99% of MS cases, as demonstrated by a pivotal study from Bjornevik et al.[121]. This study found that the association was independent of other known risk factors and specific to EBV rather than to other viruses. This study also demonstrated EBV infection to precede MS development, suggesting a causative role in MS pathogenesis. EBV has been mechanistically linked to MS through the presence of cross reactive antibodies between EBV EBNA1 and gliaCAM, observed in ~20-25% of MS cases[122]. Further examples of cross reactivity have been demonstrated between EBNA1 and ANO2, with 14.6% of MS cases displaying anti-ANO2 antibodies[123], and between antibodies against EBV BRRF3 and septin-9, a neuronally-expressed cytoplasmic protein, with MS patients having higher titres of anti-BRRF3[124].

The latitudinal gradient of increasing MS prevalence[111,112] is intimately linked to ultraviolet radiation exposure, and by extension vitamin D. Low circulating vitamin D levels are associated with greater MS risk[125] and increased axonal injury as indicated by CSF neurofilament light (NFL) levels[126]. The influence of vitamin D appears to be strongest during adolescence[127]. This is supported by work in a rat experimental autoimmune encephalopathy (EAE) wherein vitamin D supplementation during adolescence, but not in pre- or postnatal or adult periods,

reduced inflammation severity[128]. These effects are believed to be immunomodulatory and are thought to occur downstream of the initial MS-triggering events[129].

Smoking also increases the risk of developing MS, with an odds ratio of ~1.4. This relationship has been demonstrated across geographies and is dose-responsive[130,131], but occurs even in those passively exposed to smoke[132]. Interestingly, chewed tobacco appears to have a protective effect, two Swedish studies have reported a decreased MS risk in regular snuff users (odds ratio ~0.83)[133], suggesting strongly that tobacco smoke rather than nicotine heightens MS risk. Tobacco smoke is deleterious to vascular health, with this extending to the blood-brain barrier (BBB), which may be impaired in smokers[134]. Levels of proinflammatory markers associated with Alzheimer's disease (AD) risk are higher in the CSF of smokers than non-smokers[135], whilst white matter microstructural integrity is seen to be reduced in smokers with small vessel disease (SVD)[136], providing CNS evidence of smoking's negative effects that may be relevant to MS.

Obesity, particularly during early life, is associated with increased MS risk in both females and males[137–139]. This relationship appears to be dose-responsive, with higher body mass indices exerting a more pronounced effect on MS risk[140], and there is some evidence to suggest this effect is stronger in females[141]. The role of obesity in MS susceptibility is further supported by the association of genetically-influenced body mass index with MS risk[142]. Although the precise mechanistic connection remains unclear, it may involve obesity-induced

elevations in proinflammatory cytokines and the activation of microglia by fatty acids, thereby promoting a chronic neuroinflammatory state[143–145].

To date, ~236 genetic variants have been associated with increased susceptibility to MS, with the MHC region harbouring the highest number of associated variants, and the X chromosome only 1. Importantly, no single variant is sufficient to confer MS; rather, risk is conferred through a polygenic effect[146]. GWAS have identified SNPs that are particularly enriched in peripheral immune cells and microglia, collectively accounting for ~48% of the total genetic risk for MS[147]. However, when environmental influences are considered, the overall risk attributable solely to these genetic variants is lower. For example, although having an affected sibling increases an individual's risk by about sevenfold, MS remains a relatively rare condition even among families with a history of the disease[148], and hints at this role of polygenicity even in individuals with similar environmental exposures.

Among the genetic risk factors, the MHC class II allele, HLA-DRB1*15:01, is the major contributor in individuals of northern European ancestry, with an odds ratio of ~3.9[149]. HLA-DRB1*15:01 positive individuals tend to have an onset about 1 year earlier and may experience increased rates of disability and CNS atrophy[149–151]. The risk conferred by HLA DRB1*15:01 is additive[149] and interacts with environmental as well as lifestyle factors to drive high susceptibilities in those homozygous for the allele. For example, heterozygotes with HLA DRB1*15:01 and previously infected with EBV have an odd ratio of ~10.0, with this increasing to ~19.5 in homozygotes. Similar effects are seen for adolescent obesity and smoking[152].

Risk factors for MS should be considered as interlinked, and analyses of risk factor effects appropriately adjusted to isolate individual contributions to variables of interest.

1.2.3 Pathology of multiple sclerosis

1.2.3.1 Pathogenesis

The clinical efficacy of therapies targeting B cells—which significantly reduce the annualised relapse rate and brain atrophy in both RRMS and PPMS[153–156], suggests a key role for B cells in MS that is largely independent of antibody production. This is supported by the observation that B cell depletion does not result in major changes in CSF oligoclonal bands[157,158]. Clonally expanded B cells are found both in the periphery and CNS of MS patients[159–161] forming a peripheral-CNS axis that may begin within the cervical lymph nodes, which serve as the main site for brain lymphatic drainiage[162–164]. These multifunctional B cells not only secrete proinflammatory cytokines but also act as antigen-presenting cells, thereby shaping the $CD4^+$ T cell response[165,166]. In ~50% of SPMS cases, $CD20^+$ B cells may form tertiary lymphoid-like structures in the meninges, where their presence is associated with more severe demyelination, neuronal loss, and an earlier disease onset[167–170]. Single-cell RNA sequencing of these structures in EAE suggests resident B cells are highly similar to, albeit more activated, than B cells in the lymph nodes[171].

These B cell-mediated processes, which are amenable to inhibition by effective therapies, may occur downstream of initial $CD4^+$ cell activation by antigen-presenting cells and subsequent formation of inflammatory lesions within the

CNS parenchyma[172]. The precise mechanisms triggering this initial immune activation remain to be elucidated.

The resulting chronic immune activation within the CNS, characterised by the interplay of microglia, astrocytes, B cells, and $CD8^+$ T cells, may act together to drive compartmentalised pathological processes that are deleterious, and eventually fatal, to neurons[172,173]. Over time this leads to disease progression and irreversible disability accrual.

1.2.3.2 Pathological features of multiple sclerosis

1.2.3.2.1 Demyelinated lesions

Demyelinated lesions are the hallmark of MS pathology. Lesions occur in both the white and grey matter, and are initially perivenular in distribution, but may fuse as pathology spreads. The pathology of MS relating to lesions has been extensively reviewed by Hans Lassmann over the years[174–178], and is briefly summarised here.

White matter lesions may present as active, inactive, or mixed active/inactive phenotypes, with limited remyelination of inactive lesions seen. Active lesions are notable for the presence of numerous activated ‘foamy’ macrophages engaged in myelin phagocytosis[179], and express high levels of NADPH oxidase[180]. Inactive lesions typically display an acellular core, marked oligodendrocyte loss, variable axonal depletion, and substantial astrocytic gliosis that forms a glial scar[181] The perilesional areas are often bordered by variably active microglia, and inactive lesions continue to exhibit low-level axonal loss over time[182]. Mixed

active/inactive lesions, which exhibit features of both active and inactive lesions, tend to persist for extended periods and are more common in progressive forms of MS than in RRMS[183]. Remyelination of lesions, resulting in so-called shadow plaques, is relatively infrequent and varies between individuals, influenced by lesion location[184].

Grey matter lesions are generally associated with less severe inflammation compared to white matter lesions. These lesions are classed into 4 types: leukocortical (type 1) lesions occur across the deeper cortical layers and spread into the subcortical white matter, intracortical (type 2) lesions are small, cortically-restricted and perivenular, subpial lesions (type 3) are frequent and confined to layers 1-4, and type 4 lesions which represent cortex-spanning lesions that do not encroach into the subcortical white matter. Subpial lesions tend to be more common in SPMS, particularly in patients with meningeal tertiary lymphoid-like B cell structures[168].

1.2.3.2.2 Disruption of the blood-brain barrier in multiple sclerosis

Disruption of the BBB is a feature of both MS lesions and normal-appearing tissue. Early studies demonstrated that white matter lesions exhibit structural abnormalities in tight junction proteins such as ZO-1 and occludin, correlating with leakage of fibrinogen. Active lesions have the highest proportion of affected vessels, and the extent of microglial/macrophage activation in both lesions and normal-appearing white matter (NAWM) is associated with greater vessel abnormalities [185186]. Similar findings have been reported using junctional adhesion molecule A as a marker, confirming that vessel disruption is a common feature in active lesions[187]. Further comparisons of grey matter in controls,

SPMS, and PPMS patients have identified tight junction abnormalities in normal-appearing grey matter (NAGM) in SPMS, but not in PPMS, relative to controls[188]. There is also evidence of downregulation of claudin-11 in the MS BBB, although this has been documented in only a single case[189].

Fibrinogen and its insoluble form, fibrin, are useful indicators of BBB disruption in MS. Extensive fibrinogen deposition is observed in white matter (WM) lesions[190] and in the motor cortical NAGM, where deposition patterns can vary between perivascular and extracellular forms[191].

The early involvement of BBB disruption in MS pathology was first highlighted in 1990, when gadolinium-enhanced MRI showed that BBB breakdown precedes clinical symptoms and other imaging signs of new lesions[192,193]. More recently, the critical role of BBB integrity and vascular factors in MS has been increasingly recognised as fundamental to disease pathogenesis[194].

1.3 Fibrinogen and neurodegeneration

The unique properties of fibrinogen, as described in Section 1.1, can, under certain local conditions, lead to sustained proinflammatory effects. Such effects underpin the established role of fibrinogen as a contributor to neurodegenerative pathology[195].

On extravasation across an impaired BBB, which is a feature of a variety of neurodegenerative diseases including MS[194] and AD[196], fibrinogen can be converted to fibrin and the cryptic CD11b/CD18 binding epitope exposed[78,79].

Microglia and monocyte-derived macrophages bind this epitope leading to a proinflammatory phenotype. This proinflammatory response is not innately pathogenic, instead it likely provides functionality for innate immune cells to combat pathogens that might be present at a wound site elsewhere in the body; however, in the context of the CNS parenchyma this response can be prolonged and deleterious.

Mechanistic studies have elucidated a variety of roles for fibrinogen in EAE and related models. Collectively, these studies reveal that fibrinogen-related pathology is an early event that precedes demyelination[197] and that the interaction of fibrinogen with CD11b/CD18 on microglia initiates axonal damage[198]. Supporting these experimental findings, postmortem analyses of the motor cortex in MS cases have shown that subjects with high levels of extracellular fibrinogen deposition exhibit reduced neuronal density in layer 5 compared with cases with low fibrinogen deposition[191]. This evidence suggests that the injurious effects of fibrinogen persist even at the time of death.

In AD, fibrinogen has been shown to interact directly with amyloid-β (Aβ), thereby promoting fibrin formation and impeding fibrinolysis[199]. Additionally, individuals with AD homozygous for the major non-familial AD genetic risk factor apolipoprotein E ε4 show increased fibrinogen deposition in the brain[200], with fibrinogen also associating with reactive microglia in AD postmortem tissue[201]. In the 5XFAD mouse model of AD, fibrinogen drives spine elimination and cognitive impairment—an effect that can be prevented by inhibiting reactive oxygen species (ROS) or by genetic knockout of CD11b[202]. These observations suggest a putative mechanism by which fibrinogen influences disease outcomes in AD.

It is important to note that the mechanisms outlined above are not disease-specific; rather, they are consequences of fibrinogen's conversion to fibrin and its capacity to elicit an immune response via the CD11b/CD18 receptor. Consequently, such neurotoxic effects are likely common to any condition marked by reduced BBB integrity. Examples of these conditions include, but are not limited to, multiple sclerosis, Alzheimer's disease, Parkinson's disease, amyotrophic lateral sclerosis, Huntington's disease, ischemia, small vessel disease, and the ageing prrocess[203,204].

Further investigation into the effects of fibrinogen once it extravasates into the brain may, therefore, provide broad insights and potential therapeutic targets across multiple neurodegenerative disorders.

1.4 Aims and objectives

This thesis will focus on the associations between fibrinogen, neurons, and microglia in the MS motor cortex. The hypothesis of this thesis is that fibrinogen acts a driver of neurodegeneration by influencing microglial polarisation towards a chronic proinflammatory state.

To assess this hypothesis, the following aims have been set:

1) To quantitatively characterise a large cohort of MS and control motor cortex cases, determining the relationships between fibrinogen deposition and neuronal density, and selecting a clinical and demographic factor matched cohort for subsequent analyses.

2) To identify novel microglial proteins influenced by extracellular fibrinogen deposition via laser-capture microdissection and proteomic analyses
3) To quantitatively validate selected proteomic hits within the matched cohort, relating identified proteins to other pathological, clinical, and demographic variables.

This thesis aims to enhance our knowledge of fibrinogen deposition in the MS motor cortex, determine its relationship to pathological outcomes, and identify novel factors than may underlie this association.

Chapter 2 | Diversity of fibrinogen deposition patterns and their associations in the multiple sclerosis motor cortex

2.1 Introduction

Fibrinogen, a key component of the coagulation cascade, can extravasate into the CNS parenchyma and contribute to neuroinflammation in MS and a wide range of other neurological conditions[195,205]. While the link between fibrinogen and neuronal damage has been elegantly explored in model systems, the corollaries of fibrinogen deposition in the human brain are poorly understood. A previous study from our laboratory provided valuable insights into the overall association between fibrinogen and neuronal density in the MS motor cortex[191]. However, this study was limited by a relatively coarse-grained approach, and did not capture the intricate spatial heterogeneity of fibrinogen deposition patterns. Given the diverse changes seen in individual CNS cell types, anatomical locations, and tissue microenvironments in response to inflammatory stimuli[206–208], this represents a crucial gap in our understanding of where, and how, fibrinogen elicits its deleterious effects. We hypothesise that this spatial distribution is intricately linked to neurodegeneration, and therefore essential to understanding fibrinogens functional impact.

This chapter addresses this gap in our understanding by providing a high-resolution analysis of fibrinogen deposition and its association with neuronal density across a large cohort of MS and control motor cortex cases. We employ IHC with tailored image analysis techniques to map and quantify fibrinogen

deposition and neuronal densities in extensive detail, elucidating their associations in this critical region.

2.2 Methods

2.2.1 Study population

A human autopsy cohort of pathologically confirmed MS cases (n = 71) and control cases (n = 7) sourced from the Multiple Sclerosis and Parkinson's Tissue Bank at Imperial College, London, was used. Appropriate ethical approval was obtained (REC 08/MRE09/31+5) and all tissue was used in strict compliance with the conditions of the UK Human Tissue Act (2004).

DNA from MS cases was previously genotyped to determine HLA-DRB1*1501 status. All MS and control cases had Formalin-Fixed and Paraffin-Embedded (FFPE) tissue preferentially sampled from the medial precentral gyrus (motor cortex) available for neuropathological analyses. There was overlap between this cohort (n = 78) and cohorts previously used to study the neuropathology of the MS motor cortex[191].

2.2.2 Immunohistochemistry

Serial 6μm-thick FFPE sections of the motor cortex were cut using a microtome prior to air-drying and storage. Sections were labelled with primary monoclonal antibodies against fibrinogen, NeuN, and PLP (**Table 2.1**) and visualised via DAB (Dako REAL EnVision Detection System, Agilent, K5000711-2). Following DAB incubation and washes sections were counterstained with Harris haematoxylin.

Whole slide images (WSIs) at 40X magnification were obtained for each stained section using an Aperio ScanScope AT Turbo slide scanner (Leica Biosystems).

Table 2.1. IHC antibodies

Antigen	Host species	Antigen-retrieval	Dilution	Supplier	Catalogue number
Fibrinogen	Mouse	Autoclave Tris-EDTA (pH 9.0)	1:700	Abcam	Ab58207
NeuN	Mouse	Autoclave Tris-EDTA (pH 9.0)	1:400	Millipore	MAB377
PLP	Mouse	Microwave citrate (pH 6.0)	1:1000	BioRad	MCA839G

2.2.3 Binary categorisation of fibrinogen deposition type presence

Each fibrinogen WSI from the full postmortem cohort (n = 78) was assessed using QuPath quantitative pathology software[209] for the following fibrinogen staining patterns: non-neuron positive cells in grey matter, neuron positive cells, positive neurites, capillary, extracellular grey matter, extracellular white matter, positive axons in white matter, positive oligodendrocytes, non-oligodendrocyte positive cells in white matter, depth of sulcus cellular/processes, perivascular grey matter, perivascular white matter. Cases were manually inspected at a zoom approximating a 20X magnification field of view (FOV). Cases were classified as positive for a deposition pattern if the pattern occurred in at least 2 FOVs separated by >500μm.

Representative images of each deposition type are shown in **Figure 2.2**.

2.2.4 Clustering of MS cases by binary fibrinogen deposition patterns

A combined dataset of demographic and clinical features and binary fibrinogen deposition patterns was used to assess how combinations of fibrinogen deposition patterns within MS cases (n = 71) differ with regards to demographic and clinical features.

The 12 fibrinogen deposition patterns categorised according to **2.2.3.** were used within each MS case. Columns were first checked to ensure all values were binary. Multiple Correspondence Analysis (MCA) with 5 components was performed using the Prince[210] Python library to reduce the dimensionality of the data. K-means clustering was performed on the MCA data using an optimal K of 7 as determined by the silhouette score method. Resulting clusters of cases were visualised via a heatmap showing the proportion of cases within each cluster featuring each fibrinogen deposition pattern.

2.2.5 Semi-quantitative scoring of extracellular grey matter and capillary fibrinogen deposition

Extent of fibrinogen deposition in extracellular and capillary compartments was quantified via semi-quantitative scoring in approximate 40X FOVs (0.361mm x 0.270mm) systematically placed along trajectories spaced following established methods[191] in fibrinogen WSIs. Briefly, trajectories spanning layer 1 – layer 6 of the cortex were spaced at 2mm intervals along the cortex, within each trajectory 2 FOVs were placed side-by-side in layers 1, 2, 4, 5, and 6, whilst 4 FOVs were placed in layer 3. Following initial placement, adjustments were made to avoid areas with the presence of demyelination as assessed on a proximal PLP-stained

WSI, resulting in only NAGM trajectories being used for fibrinogen assessment. FOV images were exported for semi-quantitative scoring.

Semi-quantitative scoring was performed by two expert observers blinded to each other's scores, within each FOV for extracellular grey matter and capillary fibrinogen deposition patterns (**Figure 2.1**). Scores were categorised as 0 (pattern absent), 1 (pattern mild/infrequent), 2 (pattern moderate/frequent), 3 (pattern severe/very frequent). Reliability of semi-quantitative scores was assessed via intraclass correlation coefficient.

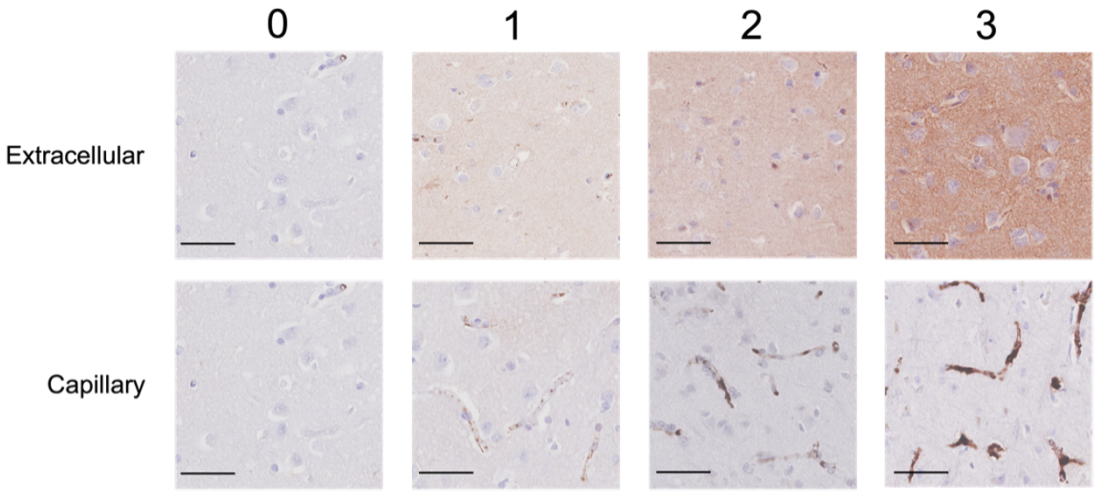

Figure 2.1 Semi-quantitative scoring guide for extracellular and capillary fibrinogen deposition.

Fields of view were scored as follows: 0 (appears absent), 1 (mild/infrequent), 2 (moderate/frequent), 3 (severe/very frequent). Scale bars represent 50μm.

2.2.6 Construction of aligned full tissue sections from WSIs

Representative MS cases for high and low extracellular grey matter fibrinogen deposition were selected and sectioned at 4μm thickness. 10 Sections were used per case with every second section (8μm step size) used. Sections were stained for fibrinogen as outlined in **2.2.2**.

Fibrinogen DAB WSIs were loaded into QuPath and rough full tissue annotations created and exported as geoJSONs. Subsequent image processing of WSIs was performed using OpenSlide Python. WSIs were down sampled by a factor of 4 and original colour (RGB) and greyscale DAB channel images extracted. geoJSONs were loaded using GeoPandas and affine transformation applied to scale the geoJSON to the down sampled WSI. Scaled geoJSONs were rasterized as white pixels onto a black mask with the same dimensions as the down sampled WSI using OpenCV-Python. Binary masks were then applied to the WSI, and greyscale DAB images inverted to give strong DAB pixels high intensity values. Tight tissue outlines were extracted from within the rough tissue mask by thresholding using Otsu's method followed by morphological opening and closing, and binary hole filling. This resulted in refined tissue masks that captured full tissue sections with negligible non-tissue pixel inclusion.

The centroid of refined tissue masks was calculated via connected component analysis. Deviation of refined tissue centroid from image centre was calculated before padding was applied to the refined tissue centroid to centre it in the image, giving an evenly padded mask. Corresponding transformations were applied to the respective image. This process was applied to all input masks and their

respective images per MS case to give an ordered series of refined tissue masks. The central image from each series of WSIs was determined and used as a fixed reference image for tissue alignment. The series of refined tissue masks was then sequentially aligned by overlaying each refined tissue mask's centroid with the reference image mask and rotating the aligning mask around the centroid of the reference in 1.0° increments with area overlap between aligning and reference images calculated at each increment. The optimal angle of rotation was then selected as the angle maximising area overlap and applied to the aligning image refined tissue mask and its associated image.

Aligned images were then written to sequential pages of a .tiff file in the desired order, outputting an original colour .tiff and greyscale DAB .tiff of now aligned full tissue sections.

2.2.7 Construction of aligned full tissue z-stacks and analysis of DAB x, y, z axis distribution

The .tiff files constructed following **2.2.6.** were read using the tifffile python library. Each slice in the .tiff files was down sampled using OpenCV-Python and nearest neighbour interpolation to dimensions of 1000 x 1000 pixels. Black pixels and near-black were removed from DAB .tiffs and white and near-white pixels removed from original colour .tiffs. DAB .tiffs pixel values were aggregated across all slices across cases to calculate global maximum and minimum values, before each slice was normalised using these globally-derived values. Normalised pixels within each slice were classified into quintiles, and per-quintile areas, bounding boxes, and centroids measured.

Image slices from original colour .tiffs and the processed slices from DAB .tiffs were plotted onto a 3D surface using Matplotlib to present the full aligned tissue stack in 3D, allowing changes in pixel intensity through the tissue to be visualised.

To assess the distribution of high fibrinogen pixels throughout the stacks quintile 4 and 5 pixels were recorded as their combined proportion of total pixels within each slice of the processed DAB .tiffs. Quintile 4/5 combined proportion was then plotted against its slice index to create a scatter plot and ordinary least squares (OLS) regression performed with quintile 4/5 proportion as the dependent variable.

2.2.8 Motor cortex ROI fibrinogen segmentation, spatial normalisation and aggregation

2.2.8.1 Extraction and consistent orientation of fibrinogen DAB ROIs

Fibrinogen DAB WSIs were manually annotated in QuPath to identify each cortical layer and the rough orientation of the cortical areas surface (left/right/up/down). Annotations were ~1.5mm in length to allow for efficient memory usage later in the analyses. Annotations were exported as geoJSONs. WSIs were loaded at native resolution using OpenSlide Python and geoJSONs processed sequentially. The bounding box of each geoJSON was applied to the WSI to extract the tissue image, with pixels falling outside of the annotation region of interest (ROI) set to 0, preserving the original annotation within a black bounding box. The DAB channel was then extracted and inverted to give greater intensity values to darker (more DAB) areas.

A binary mask of non-black pixels corresponding to the annotation ROI was then created, rotated based on file name ('left' = -90°, 'right' = 90°, 'bottom' = 180°, 'top' = 0°), and finely rotated between -45° to 45° in 1° increments with horizontal non-zero pixel width from the centroid measured at each increment. This resulted in all annotation ROIs being oriented in the same plane, as if the cortical surface was up and the white matter down.

2.2.8.2 Segmentation of fibrinogen object clusters within ROIs

Within each reoriented annotation ROI fibrinogen positive object clusters were identified by applying Otsu thresholding within annotation ROIs, with objects <1000 pixels in area removed, before erosion and dilation with a large structural element (12 pixels) was performed to separate distinct objects. Further object filtering was then applied to remove objects with an average pixel intensity <70% of the mean of all detected objects, objects >12000 pixels in area, objects with an aspect ratio >3.0, and objects with a solidity of <0.85. To remove very proximal or isolated objects k-d trees was used for nearest neighbour searches within 150 pixels of each object's centroid. Objects were removed if their centroid was <35 pixels or >150 pixels of another object's centroid. This approach removed artefacts and filtered out objects composed of small or intermediate blood vessels or isolated cells. Given this set of spatially indexed refined objects, object clusters were constructed. Seed objects were defined as an object with at least 3 neighbour objects within a 300-pixel radius of the seed object centroid. Breadth-first search was used to aggregate neighbouring objects within a 300-pixel radius of each object in a clusters centroid to iteratively build out clusters to include spatially contiguous objects until no further objects could be added, giving a

complete object cluster. The convex hull of the cluster was identified by computing the minimum bounding polygon of cluster-edge objects that encompassed all other objects within the cluster. Clusters with a convex hull area <40000 pixels (very small clusters) or with >40% black pixels (clusters with substantial overlap at annotation ROI edge) were removed. Within valid clusters object identification was performed again with 10% reduced size and intensity thresholds. Within object clusters object count along with mean, median, and SD of object size were recorded, along with cluster convex hull dimensions. Distance between the centroids of unique cluster pairs was calculated and normalised by the sum of the radii of the cluster pair to give a scale-invariant measure of proximity. Statistics were recorded in their raw form and aggregated at the ROI level to give per-ROI measures of total coverage.

GeoJSONs of object cluster convex hulls were saved.

2.2.8.3 Segmentation of fibrinogen object clusters within ROIs

Extracellular fibrinogen deposition within annotation ROIs were identified by using a dataset of case-specific extracellular grey matter fibrinogen measurement geoJSONs after fibrinogen objects had been segmented. These geoJSONs were applied to each WSI at the start of its processing to extract raw inverted dab pixel intensity values. Non-object pixels had a threshold applied via Otsu's method to identify broad regions; this was then used to establish an upper threshold for extracellular fibrinogen pixels dynamically based on the values of the input extracellular geoJSONs. The lower threshold was set to the 5^{th} percentile of the input geoJSONs intensities, whilst the upper threshold was set to 1.7* Otsu threshold. In cases with uniformly intense fibrinogen DAB signal the lower

threshold was >1.7* Otsu threshold, and the upper threshold was adjusted to the 95th percentile of input geoJSON intensities. Contiguous extracellular fibrinogen patches were joined using connected component labelling, and area filtered to remove patches with <25000-pixel areas or >40% black pixel proportion. Gaps within valid extracellular fibrinogen objects were filled via binary hole filling to give final extracellular fibrinogen masks. The area, ROI % coverage, centroid, and radius of each object were recorded along with mean, median, minimum, and maximum pixel intensity values. The bounding box of object convex hull was recorded. Distance between the centroids of unique extracellular object pairs was calculated and normalised by the sum of the radii of the extracellular object pair to give a scale-invariant measure of proximity. Statistics were recorded in their raw form and aggregated at the ROI level to give per-ROI measures of total coverage.

GeoJSONs of extracellular fibrinogen objects convex hulls were saved.

2.2.8.4 Column-wise tiling and rearrangement of fibrinogen DAB ROIs

To facilitate the downstream spatial comparisons of fibrinogen deposition within each cortical layer, the complex polygonal annotation ROIs required transformation to a common spatial framework.

Annotation ROI bounding boxes were tiled with 50x50 pixel squares, giving columns of regular tiles. Tiles we processed in a column-wise manner, iterating vertically from top to bottom. Valid tiles with >80% non-black pixels had column index, row index, pixel coordinates, average intensity, and interpolation status recorded for subsequent analysis. Black tiles were labelled.

Within the first column the highest valid tile was identified and first row index recorded. Subsequent column first tiles were aligned to this by padding the top or bottom of the column with new black tiles, giving a uniform valid top edge and flattening the image. Within the flattened image black tiles were interpolated using a random valid tile interpolation strategy. Due to the flat valid top edge interpolation only influenced tiles in the lower areas of the image. A mask of interpolated tiles was saved for later analyses. Percentage of interpolated tiles within each column was assessed and columns with >50% interpolation dropped. The output of this was a flattened rectangular annotation ROI .png image, alongside flattened images created using the extracellular fibrinogen deposition masks from 1.2.8.3 and interpolated masks. Output images for full annotation ROI, masked extracellular fibrinogen, and interpolation were given the ‘full’, ‘patches’, and ‘interpolated’ suffixes respectively.

2.2.8.5 Size normalisation and area-weighted aggregation of flattened fibrinogen DAB ROIs

Input image filenames were parsed to identify image type (‘full’, ‘patches’, ‘interpolated’), case ID, and cortical layer. Anatomically relevant target image sizes were defined at 5000x500 pixels for L1, L2, L4, 5000x1250 pixels for L3, and 5000x1000 pixels for L5 and L6. Flattened images were scaled to target size using PIL with the LANCZOS filter to preserve image quality. Within each case ID, image type, and layer, size-normalised images were aggregated using an original-ROI area weighted approach to preserve the greater contribution of larger input annotation ROIs.

All aggregated image .png files within each image type were normalised using the global minimum and maximum intensity across the full sub-cohort of MS cases (n = 40) and scaled to the 0-255 range. Images were not normalised by cortical layer to allow for accurate layer-layer comparisons. The final outputs of this image processing pipeline were per-case size and intensity normalised images of full and extracellular grey matter fibrinogen deposition suitable for spatial analyses within each cortical layer.

2.2.9 Cohen's d heatmaps of normalised fibrinogen DAB ROIs

Normalised fibrinogen images of each type produced following **2.2.8.5**. were grouped into the low and high extracellular grey matter fibrinogen deposition groups to be used for proteomic analyses. For each image type ('full', 'patches', 'interpolated') images from each cortical layer were loaded using PIL to convert them to 2D NumPy arrays of fixed layer-specific dimensions. Within each group mean and variance at each pixel position recorded. The pooled standard deviation of both groups was calculated by averaging the group variances and taking the square root. The difference in group means at each pixel position was divided by the pooled standard deviation to give a Cohen's d value at each pixel.

Cohen's d was visualised using matplotlib as a heatmap with a custom yellow, red colourmap to account for the low fibrinogen group serving as a baseline where fibrinogen was variably absent. Each cortical layer used the same colour mapping to facilitate layer-layer comparisons.

Cohen's d values were binned into 0.5 increments between 0.0 – 4.0, and the proportion of pixels within each layer falling within each bin plotted as bar plots.

2.2.9.1 Horizontal profile analysis of Cohen's d heatmap

Variation across the normalised space of each image type and layer's Cohen's d heatmap was measured by horizontal profile analysis. Heatmaps generated following 1.2.9. were converted using PIL to give 2D NumPy arrays with a Cohen's d value at each pixel. A window of 50x50 pixels with a stride of 25x25 pixels was used for sliding window analysis from left-right of each heatmap. Within each window mean and variance of Cohen's d were calculated to quantify central tendency and dispersion.

The change in Cohen's d across the heatmap was plotted as a grey line trace for each horizontal window, and an average trace calculated from the mean of all traces at each x-coordinate position and plotted as a black line. The characteristics of this average trace were quantified as total transitions across the full horizontal profile of ±0.2 Cohen's d with the x-coordinate at which this threshold was crossed recorded, distance in x pixels between transition points was recorded, along with direction of transition (up/down), and slope of transition.

The count of total, up, and down transitions within each cortical layer was plotted as a bar plot.

2.2.10 Segmentation of NeuN objects from DAB WSI

FFPE sections were stained for NeuN and processed to give WSIs as in **2.2.2**. Layer-specific annotations within each WSI were manually drawn using QuPath and exported as geoJSON files.

WSIs were loaded using OpenSlide Python and annotation images extracted by applying annotation geoJSON masks to obtain the annotation bounding box. Pixels outside of the annotation ROI were set to black to preserve only data from within the ROI. The DAB channel was then extracted and inverted to give strongly DAB-positive objects high pixel intensity values. Pixel dimensions were derived from the WSI metadata.

Within each case extracted annotation ROIs layers 2 – 6 were processed individually to account for area-area staining intensity shifts. NeuN objects were identified via Otsu's method, followed by morphological opening (disk radius 3), object <50-pixel removal, binary hole filling, and smoothing (disk radius 12). Objects with an area >1000μm^2 were excluded. Layer 1 annotations had the average Otsu threshold of all layer 2 annotations within the case applied.

Objects were classified as small (30-75μm^2), intermediate (76-170μm^2), large (171-250μm^2), and very large (251+μm^2) based on previous manual measurements of cell sizes. Segmentation was visualised per size class and for all objects onto a black space and onto the raw annotation ROI at full resolution (small = red), intermediate = green, large = blue, very large = yellow).

2.2.10.1 NeuN object measurements

The size-classified NeuN objects created following **2.2.10.** were individually processed to obtain highly granular measurements of morphology and local neuronal density. All objects were iterated through, with object area (μm^2), average pixel intensity, eccentricity, circularity, and aspect ratio recorded. Local

neuronal densities (objects/mm^2) were recorded within an 80μm radius of each object's centroid, along with the average non-object pixel intensity in this area.

Measurements were aggregated at the annotation ROI level, with mean and variability in each measurement, along with overall object density and densities for each object class (cells/mm^2) recorded, along with the proportional contribution of each size class to the total object count.

Data for individual objects and full annotations was saved as separate .csv files. Annotation-level data was cleaned conservatively using a 1.5* IQR method with any row containing a value outside of this range in the density of small, intermediate, or large neurons dropped.

2.2.11 Linear mixed models

Linear mixed models (LMM) were used to account for the nested structure of measurements within cases. WSI-derived .csv datasets were loaded in Pandas dataframe and merged via case IDs with case demographic and clinical metadata to give wide merged datasets for use in LMMs. Variable types were enforced within each column with continuous variables asset to numeric, and binary categorical data to Boolean.

Given the vastly different scales of variables within datasets (e.g. overall neuronal density and mean circularity) continuous predictor and dependent variables were standardised via z-score transformation to have a mean of 0.0 and SD of 1.0 using scikit-learn's StandardScaler function. Interaction terms were manually

created by multiplying pairs of standardised predictors. Choice of interaction terms leveraged domain-specific knowledge.

LMMs were specified to select any combination of layer annotation classes as input data, the dependent variable, predictors, interaction terms, and whether inter-layer fixed effects should be included. Data was filtered to match the model specification, and the LMM fitted using the Statsmodel library with maximum likelihood estimation. All models successfully converged. Random intercepts for case ID were included to account for case-case variability across the cohort. Model outputs were subjected to BH correction to control the false discovery rate. Multicollinearity amongst predictors was assessed using the variance inflation factor method and models adjusted accordingly.

LMM goodness of fit was assessed for different biologically relevant combinations of predictors by calculating Akaike information criterion (AIC) and Bayesian information criterion (BIC), with the combination of predictors that minimised these values selected.

2.2.12 Statistical analyses

Statistical testing was performed using SciPy's statistical functions. Where two groups were present, the choice of test was determined by assessing the normality of each group's data via Shapiro-Wilk test. If one group in a comparison's data was non-normally distributed a Mann-Witney U test was used. If both groups were normally distributed an independent t test was used. All tests were two-sided. Where more than two groups were present a one-way ANOVA followed by Tukey's honest significant difference post-hoc test was used.

BH correction to control false discovery rate was selectively applied depending on the goals of the analysis, with BH correction not applied where the analysis was exploratory and subject to later confirmation via another method. For example, this procedure was followed for the grouped analyses of individual NeuN objects, where significant outputs were used to inform the development of LMMs.

All output correlation coefficient *p* values from Pearson correlations, OLS and LMM regression models were BH corrected.

2.3 Results

2.3.1 Demographic and clinical features of overall study population

Demographic and clinical features of the MS and control cohort used for this study are shown in **Table 2.2**. All MS cases had a progressive clinical course (12.6% = PPMS, 87.4% SPMS). Due to the focus of this study being within MS differences resulting from fibrinogen, and the small number of control cases available, detailed statistical comparisons between the demographic and clinical features of MS and control cases were not performed.

Table 2.2. Demographic and clinical features of cohort

	MS (*n* = 71)	**Control (*n* = 7)**
Sex (% female)	73.2	42.9
Disease subtype	PPMS = 9 SPMS = 62	N/A
Brain weight (g)	1164 (*n* = 70, 800 – 1557)	1278 (*n* = 7, 1072 – 1465)
Postmortem interval (yrs)	16.2 (*n* = 71, 6.0 – 31.0)	27.4 (*n* = 7, 10.0 – 52.0)
CSF pH	6.9 (*n* = 52, 5.7 – 9.2)	7.4 (*n* = 7, 7.2 – 7.8)
Disease duration (yrs)	28.9 (*n* = 71, 7.0 – 57.0)	N/A
Time onset – wheelchair (yrs)	18.1 (*n* = 62, 2.0 – 45.0)	N/A
Age at death (yrs)	62.8 (*n* = 71, 40.0 – 92.0)	74.8 (*n* = 7, 68.0 – 85.0)

To assess the relationships among demographic and clinical factors within MS, partial OLS regression analyses were performed for MS cases with values available for all demographic and clinical variables (**Figure 2.2**, *n* = 46). Within this analysis each demographic and clinical variable was in turn used as the dependent variable with all other variables as predictors, allowing the individual

contributions of each variable to be assessed. Continuous variables were standardised to a mean of 0 and SD of 1.

Within this subset of MS cases, several significant associations remained after BH-correction for multiple comparisons (**Figure 2.2.**). Female sex was associated with reduced brain weight (β = -084, 95% CI = -1.36 - -0.31, p = 0.003). Disease duration demonstrated positive associations with age at death (β = 0.40, 95% CI = 0.15 – 0.65, p = 0.002) and time onset-wheelchair (β = 0.46, 95% CI = 0.22 – 0.71, p = 0.001). CSF pH was positively associated with brain weight (β = 0.33, 95% CI = 0.10 – 0.57, p = 0.007).

Figure 2.2. Partial OLS regression matrix of demographic and clinical variables within MS *cases*.

Regression results for MS cases for which all demographic and clinical variables were available (n = 46). Significant coefficients are highlighted in green.

2.3.2 Fibrinogen deposition patterns in the motor cortex

Fibrinogen demonstrated striking heterogeneity in deposition patterns. Cell body, extracellular, and neurite/glial process deposition patterns previously[191] were validated in this larger cohort. In total, 12 distinct fibrinogen deposition patterns were recorded. Well-delineated cells with strongly astrocytic morphologies (**Figure 2.3B**) were a common feature in the superficial cortical layers with more sparse presence throughout the deeper cortical layers. These cells were often

observed near blood vessels, where processes could be seen to contact the vessels. Equally well-delineated cells with neuronal morphologies, including dendritic and axonal processes, were recorded throughout the cortical layers (**Figure 2.3C**). Both grey matter deposition patterns occurred in clusters of positive cells and were not a uniform feature across tissue sections. Capillaries in the grey matter showed a range of fibrinogen staining intensities, with intraluminal and endothelial deposition noted (**Figure 2.3D**). Extracellular deposition was present in both the grey matter (**Figure 2.3E**) and white matter (**Figure 2.3F**). In both locations strongly stained patches (red arrow) could appear adjacent to areas with a very low staining (blue arrow). Within the white matter fibrinogen-positive axons (**Figure 2.3G**) and cells with oligodendroglial morphologies (**Figure 2.3H**) and astrocytic morphologies (**Figure 2.3I**) were seen. Exacerbation of cellular staining, particularly of cells with astrocytic morphology, was commonly seen at the depths of sulci (**Figure 2.3J**). Perivascular deposition in the extracellular space was seen in both the grey (**Figure 2.3K**) and white (**Figure 2.3L**) matter.

Each deposition pattern was variably present across the cohort, with capillary and extracellular grey matter deposition the most frequent patterns and perivascular whiter matter and white matter axonal deposition patterns the least frequent (**Figure 2.3M**). MS and control cases did not differ with respect to the proportions of cases displaying each deposition type.

2.3.3 Correlations between fibrinogen deposition types and demographic and clinical variables

To assess if the binary presence of a given deposition pattern within a case was associated with other deposition pattern or demographic and clinical factors Pearson correlations were recorded between each pair of variables and resulting *p* values corrected for multiple comparisons (**Figure 2.3N**). No significant correlations were recorded between fibrinogen deposition patterns and demographic and clinical variables. Significant correlations were present between demographic and clinical variables, with these very similar to the previous partial OLS models (**Figure 2.2**). Between deposition types, fibrinogen-positive neuron deposition positively correlated with non-neuron fibrinogen-positive cells in the grey matter (r = 0.63, 95% CI = 0.41 – 0.76, p <0.001), and fibrinogen-positive neurites (r = 0.79, 95% CI = 0.66 – 0.88, p <0.001). Extracellular grey matter fibrinogen deposition associated with non-neuron fibrinogen-positive cells in the grey matter (r = 0.52, 95% CI = 0.27 – 0.70, p = 0.002), fibrinogen-positive neuron deposition (r = 0.73, 95% CI = 0.56 – 0.84, p <0.001), and fibrinogen-positive neurites (r = 0.59, 95% CI = 0.36 – 0.75, p <0.001). Amongst white matter deposition patterns extracellular deposition was positively correlated with non-oligodendrocyte cellular staining (r = 0.45, 95% CI = 0.18 – 0.65), and oligodendrocyte fibrinogen-positive cells associated with non-oligodendrocyte fibrinogen-positive cells (r = 0.66, 95% CI = 0.46 – 0.79, p <0.001)

Notably amongst the non-significant correlations capillary fibrinogen deposition was negatively correlated with both grey and white matter extracellular

deposition, and all cellular deposition types. Extracellular grey matter fibrinogen deposition was near to significance in its negative correlation with brain weight (r = -0.35, p = 0.01).

2.3.4 Clustering of MS cases by presence/absence of fibrinogen deposition patterns and analysis of demographic and clinical variables

As individual fibrinogen patterns did not significantly correlate with demographic and clinical variables, the effects of combinations of deposition patterns within a case was investigated.

MCA analysis with 5 components was used to reduce the dimensionality of the binary deposition patten data, before cases were clustered using K-means with an optimal K of 7 as identified by silhouette score (**Figure 2.3O**). The resulting 7 clusters differed in their proportions of cases displaying each deposition pattern, but no pattern was unique to only one cluster (**Figure 2.3P**).

Clusters were assessed for effects in each demographic and clinical variable. One-way ANOVA suggested a moderate effect of borderline significance of cluster on age at death (p = 0.066). This was investigated via Tukeys HSD post-hoc test which showed no significant difference between clusters with regards to age at death (**Figure 2.3Q**).

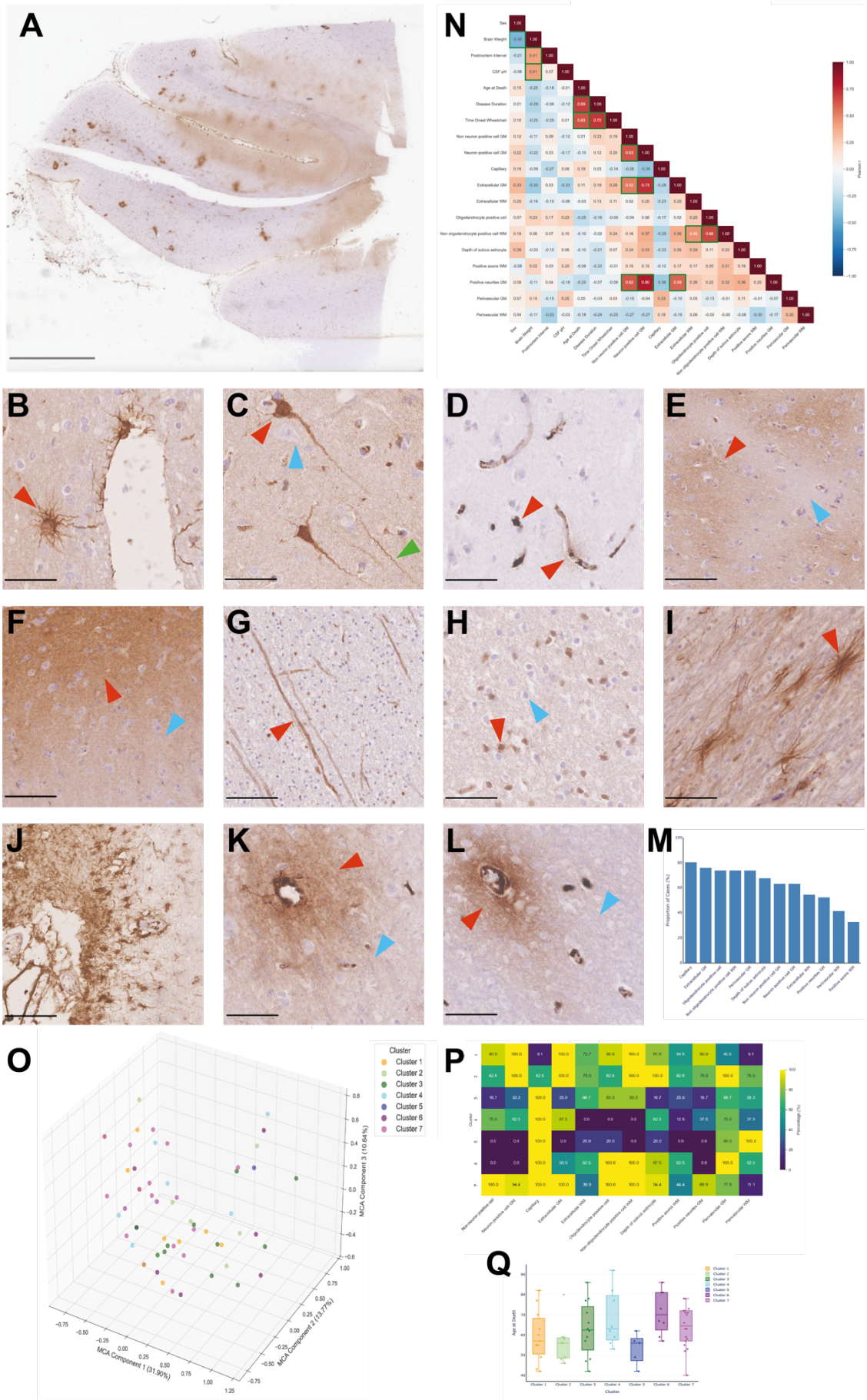
A
N
B
C
D
E
F
G
H
I
J
K
L
M
O
Cluster
Cluster 1
Cluster 2
Cluster 3
Cluster 4
Cluster 5
Cluster 6
Cluster 7
MCA Component 1 (31.90%)
MCA Component 2 (13.77%)
MCA Component 3 (10.64%)
P
Q

Figure 2.3. Fibrinogen deposition patterns are diverse and correlate poorly with demographic and clinical data.

A, Representative motor cortical section stained for fibrinogen and displaying typical spatial heterogeneity in deposition types. **B-L**, Representative images of fibrinogen deposition types. **B**, Fibrinogen-positive cells with strongly astrocytic morphologies (red arrow) adjacent to a blood vessel in the grey matter. **C**, Fibrinogen-positive neurons (red arrows) adjacent to fibrinogen-negative neurons (blue arrow). A fibrinogen-positive neurite (green arrow) is visible. **D**, Capillaries containing fibrinogen in the grey matter. **E**, Extracellular staining of fibrinogen in the grey matter with areas of intense staining (red arrow) and relative paucity (blue arrow). **F**, Extracellular staining of fibrinogen in the white matter (red) showing increasing gradient from the proximal grey matter (blue arrow). **G**, Axonal fibrinogen staining in the white matter (red arrow). **H**, Fibrinogen-positive cells with oligodendrocyte-like morphology (red arrow) adjacent to fibrinogen-negative cells. **I**, Fibrinogen-positive cells with strongly astrocytic morphologies (red arrow) in the white matter. **J**, Widespread cellular staining at the depth of a sulcus. **K**, Grey matter vessel with fibrinogen extravasation. **L**, White matter vessel with fibrinogen extravasation. **M**, Proportion of post-mortem MS and control cohort (n = 78) displaying each deposition type. **N**, Significant Pearson correlations were only seen between demographic and clinical variables or between fibrinogen deposition patterns. **O**, Multiple correspondence analysis plot of combinations of fibrinogen patterns clustered via K-means with optimal K as determined by the silhouette score method. **P**, Proportion of cases within each cluster displaying each fibrinogen deposition pattern. **Q**, No significant differences between clusters for age at death as measured by Tukey's HSD post-hoc. Multiple comparisons corrected via BH method. Significant Pearson correlations highlighted in green. Scale bars represent 5mm (A), 50μm (B, C, D, H, I, K, L) or 100μm (E, F, G, J).

2.3.5 Semi-quantitative scoring of extracellular grey matter and capillary fibrinogen deposition

Semi-quantitative scores were used to assess the extent of extracellular grey matter and capillary fibrinogen deposition which was highly variable between and within cases (**Figure 2.4A-D**). both semi-quantitative scoring methods had excellent interrater reliability (extracellular grey matter ICC = 0.93, capillary ICC = 0.90).

Extracellular fibrinogen deposition did not differ when comparing MS cases to controls within any of the cortical layers, but did differ between the superficial (layers 1, 2, 3) and deeper cortical layers (**Figure 2.4G**, p <0.001).

Capillary fibrinogen deposition was generally higher in MS cases compared to control with this reaching significance in layers 1 (p = 0.007) and 2 (p = 0.002). Capillary deposition was higher in the deeper cortical layers (**Figure 2.4H**, p <0.001).

2.3.6 Distribution of extracellular grey matter fibrinogen deposition scores in layer 5 of the motor cortex across MS cases

Given the previous finding in our laboratory of extracellular fibrinogen deposition negatively correlating with neuronal density in layer 5[191], the relationship between fibrinogen and neurons was to be further investigated using a larger demographically and clinically matched cohort of MS cases with high and low extracellular fibrinogen deposition.

Within layer 5 MS cases had a range of 0.50 to 2.11 for extracellular grey matter fibrinogen score. The average score was 1.44, with the average SD being 0.83 (**Figure 2.4I**). This demonstrates the significant intra-case heterogeneity seen within a single deposition type.

2.3.7 Linear mixed model of demographic and clinical factors and capillary semi-quantitative score on extracellular grey matter fibrinogen score

To preserve the variability seen within cases for semi-quantitative scoring of extracellular fibrinogen, and to account for between case differences, a LMM was developed (**Figure 2.4J**). The inclusion of all demographic and clinical variables in this model reduced the number of MS cases that could be used (n = 46). Despite this, when compared to models with fewer demographic and clinical predictors, and more cases, the results in common predictors were relatively static.

When controlling for other predictors, capillary semi-quantitative score emerged as a significantly negatively associated with extracellular grey matter semi-quantitative score (β = -0.121, 95% CI = -0.227 - -0.015, p = 0.025). This effect size was small, with each 1 unit increase in capillary semi-quantitative score associated with a -0.121 change in extracellular fibrinogen semi-quantitative score. CSF pH was borderline significant for a negative association with extracellular score (β -0.227, 95% CI = -0.457 - -0.002, p = 0.052).

Time from onset to wheelchair was the only predictor positively associated with extracellular fibrinogen score (β = 0.385, 95% CI = 0.079 – 0.69, p = 0.014).

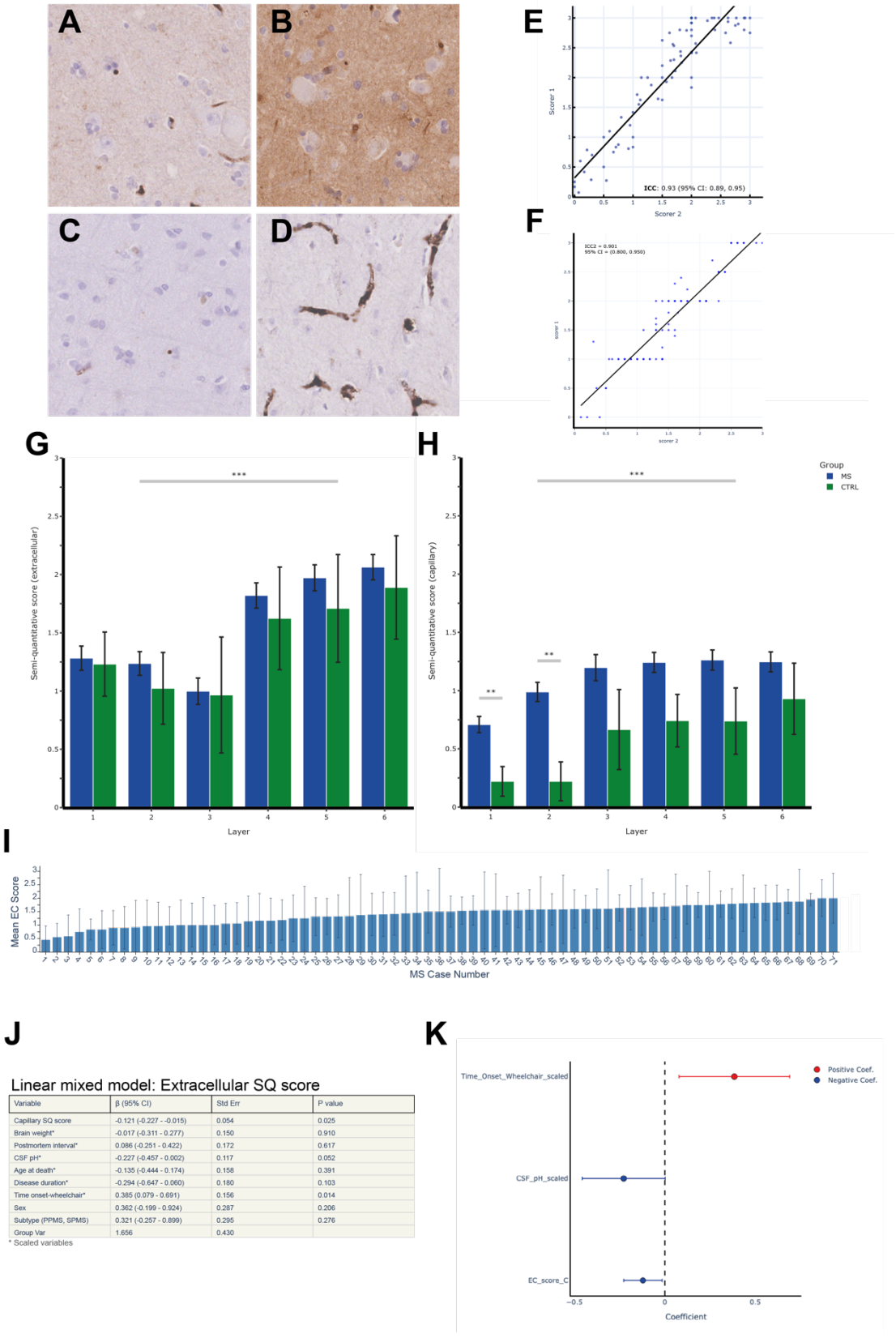

Figure 2.4. Semi-quantitative scoring of extracellular grey matter and capillary fibrinogen deposition patterns across the cortical layers. A-D, Representative images of low and high semi-quantitatively scored tissue for extracellular grey matter (A, B) and capillary (C, D). **E**,**F**, Inter-rater reliability as measured by intraclass correlation coefficient shows excellent reliability for extracellular grey matter (**E**, ICC = 0.93) and capillary (**F**, ICC = 0.90) semi-quantitative scores. **G**, Extracellular grey

matter fibrinogen deposition is increased in deeper cortical layers L4, L5, L6 ($p < 0.001$) but does not differ between MS and control cases across any cortical layer. **H**, Capillary fibrinogen deposition is consistently higher in MS cases than controls across all cortical layers, with this reaching significance in L1 ($p = 0.07$) and L2 ($p = 0.002$). Deeper cortical layers L4, L5, L6 show increased capillary fibrinogen deposition ($p < 0.001$). **I**, The distribution of L5 extracellular grey matter semi-quantitative scores across MS cases ($n = 71$) shows notable heterogeneity (mean score = 1.44, mean SD = 0.83). **J-K**, Linear mixed modelling of the effects of different variables on extracellular grey matter semi-quantitative scores within MS cases (J) with significant correlations visualised via forest plot (K). Error bars in G, H represent ±SEM, error bars in I represent ±SD. Independent t-tests were used in the statistical analyses in G, H.

2.3.8 Distribution of fibrinogen within representative high and low extracellular deposition WSI z-stacks

The extensive variability in fibrinogen deposition within WSIs had not previously been assessed through the z axis of FFPE tissue blocks, presenting a significant limitation when comparing fibrinogen-stained sections to other markers on adjacent/semi-adjacent slides. To address this limitation a custom WSI alignment pipeline was developed to allow DAB pixels to be quantified for full tissue areas across adjacent/semi-adjacent 4μm sections.

Briefly, this pipeline involved manually roughly annotating tissue areas on WSIs, before precise tissue extraction was achieved using Otsu's method and the resulting tissue masked cleaned. Tissue on slides is often in different rotational planes, even when prepared by a technically skilled expert, it therefore requires alignment to be used comparatively in the z dimension. Alignment across extracted tissue masks was achieved by identifying the centroid of each tissue mask, aligning centroids, setting a common canvas size, and performing fine rotation to maximise area overlap, with the optimal transformations then applied

to the WSI itself to yield spatially aligned WSIs of the original composite image and the DAB channel (**Figure 2.5A**).

To quantify fibrinogen deposition across slides, representative high (MS067) and low (MS216) extracellular fibrinogen deposition cases were selected. Blocks were sectioned at 4μm and every second section stained for fibrinogen across 10 sections, giving a z-depth of 80μm. Alignment was performed across these sections to give full WSI z-stacks (**Figure 2.5B, D**). Section 10 of MS216 did not stain successfully and was excluded.

2.3.8.1 Quantification of fibrinogen deposition across WSI z stacks

Slices from both DAB channel z-stacks were globally normalised to allow intra and inter-stack comparisons of DAB pixel values. Pixels were classified into quintiles based on DAB pixel intensity, with the proportion of pixels of each quintile in each slice and spatial properties of each quintile area recorded. Quintiles were visualised across each z-stack (**Figure 2.5C, E**).

When looking at average proportions of pixels in each quintile across the full z-stack, MS067, the representative high extracellular fibrinogen deposition case had a higher proportion of pixels in quintiles 4 and 5; whilst the representative low extracellular fibrinogen deposition case, MS216, had a greater proportion of pixels in quintiles 1 and 2 (**Figure 2.5F**). However, when assessing the proportion of quintile 4/5 pixels across each slice of the stack (**Figure 2.5G**), MS216 showed a significant association between slice index and stack and quintile 4/5 proportion (adjusted R^2 = 0.428, p = 0.033). MS067 showed no association between slice index and quintile 4/5 proportion (adjusted R^2 = 0.058, p = 0.248).

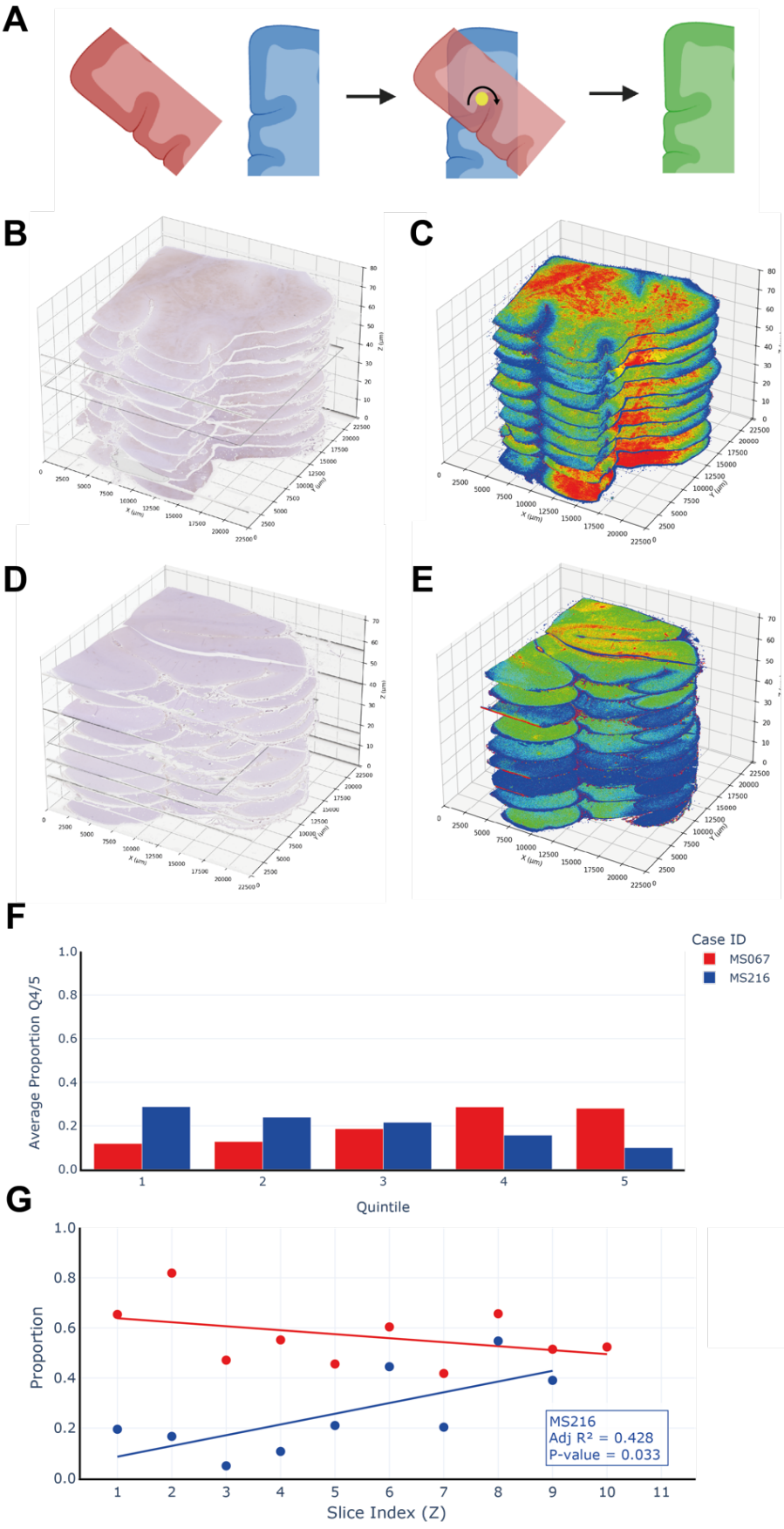
A
B
C
D
E
F
Case ID
MS067
MS216
Average Proportion Q4/5
Quintile
G
Proportion
MS216
Adj R² = 0.428
P-value = 0.033
Slice Index (Z)

Figure 2.5. Fibrinogen deposition quantified across representative whole-slide image stacks.

A, Schematic showing the WSI alignment process of tissue extraction followed by centroid alignment, canvas equalisation, and fine rotational alignment. **B**, Raw whole-slide image stack of 10 semi-adjacent 4μm-thick sections from MS067 a representative high extracellular grey matter fibrinogen deposition case. **C**, MS067 whole-slide image stack DAB channel pixels coloured by quintile (1 = blue, 2 = cyan, 3 = green, 4 = yellow, 5 = red). **D**, Raw whole-slide image stack of 9 semi-adjacent sections from MS216, a representative low extracellular grey matter fibrinogen deposition case. **E**, MS216 whole-slide image stack pixels coloured by quintile. **F**, MS067 shows a greater proportion of pixels in quintiles 4 and 5 than MS216. **G**, MS216 shows a significant increase in quintile 4/5 pixel proportions over the stack (R^2 = 0.428, p = 0.033).

2.3.9 Demographic and clinical features of proteomic study population

To assess the relationship between fibrinogen and neuropathological measures in more depth, a subset of 40 cases was selected for proteomic analysis (**Table 2.3**). MS cases within this sub-cohort were matched for demographic and clinical variables and differed only in their layer 5 extracellular fibrinogen deposition semi-quantitative score (p <0.001). This sub-cohort of high (F+) and low (F-) MS cases was used for more granular quantification of neuropathological measures and later proteomic analyses.

Table 2.3. Demographic and clinical features of proteomic cohort

	F+ (*n* = 20)	F- (*n* = 20)	*P* value
Sex (% female)	75	70	0.73
Disease subtype	SPMS = 20	SPMS = 20	1.0
Brain weight (g)	1140 (*n* = 20, 932 – 1370)	1204 (*n* = 20, 885 – 1557)	0.22
Postmortem interval (yrs)	15.95 (*n* = 20, 7.0 – 31.0)	16.55 (*n* = 20, 7.0 – 28.0)	0.78
CSF pH	6.87 (*n* = 12, 6.4 – 7.6)	7.22 (*n* = 15, 6.5 – 9.2)	0.12
Disease duration (yrs)	28.2 (*n* = 20, 11.0 – 50.0)	31.9 (*n* = 20, 17.0 – 56.0)	0.30
Time onset – wheelchair (yrs)	17.7 (*n* = 17, 4.0 – 35.0)	20.9 (*n* = 17, 3.0 – 33.0)	0.38
Age at death (yrs)	60.9 (*n* = 20, 42.0 – 82.0)	72.9 (*n* = 20, 43.0 – 86.0)	0.59
Layer 5 extracellular SQ score	2.53 (*n* = 20, 2.0 – 3.0)	0.96 (*n* = 20, 0.0 – 1.8)	<0.001

2.3.10 Normalisation of ROIs within cortical layers to allow spatial comparisons of fibrinogen deposition across cases

The variability in shape of cortical layers across motor cortical blocks presents a challenge when seeking to understand how fibrinogen deposition varies within and between cortical layers of a large cohort. To overcome this and quantify how fibrinogen spatially varies between the F+ and F- groups, a custom ROI normalisation pipeline was developed to fit ROIs to a common space per cortical layer (**Figure 2.6A**, **B**).

In brief, multiple layer-specific annotations of up to ~1.5mm length were manually drawn per case. ROI images were exported, oriented to a common directional plane, and raw deposition features of extracellular fibrinogen deposition (patch size, patch-patch distance, patch pixel intensity descriptive statistics) and object clusters (object size descriptive statistics, cluster size, cluster-cluster distance) extracted and masked for use in isolation. Images of the full ROI and masked regions of each deposition type were then flattened from their original complex polygonal shapes to minimal rectangles of native ROI width. Flattened ROIs of each layer class were then scaled to a common size per layer and combined via size-weighted aggregation to give a single representative size-normalised image per layer and deposition type per case (**Figure 2.6C**).

2.3.11 Analysis of extracellular fibrinogen patches and object clusters between high and low extracellular fibrinogen MS cases

Analysis of raw deposition type data extracted prior to ROI normalisation (**Figure 2.6C**) for fibrinogen object clusters suggests a higher density of fibrinogen-positive objects, primarily cells of different types, within each cluster in F+ cases (**Figure 2.6D**). However, after correcting for multiple comparisons this only reached significance in layer 3 (p = 0.006). No difference was significant difference was observed between F+ and F- cases for positive object size (**Figure 2.6E**).

No significant differences were seen between F+ and F- cases regarding extracellular fibrinogen patch-patch distance (**Figure 2.6F**) or mean extracellular fibrinogen patch pixel intensity (**Figure 2.6G**).

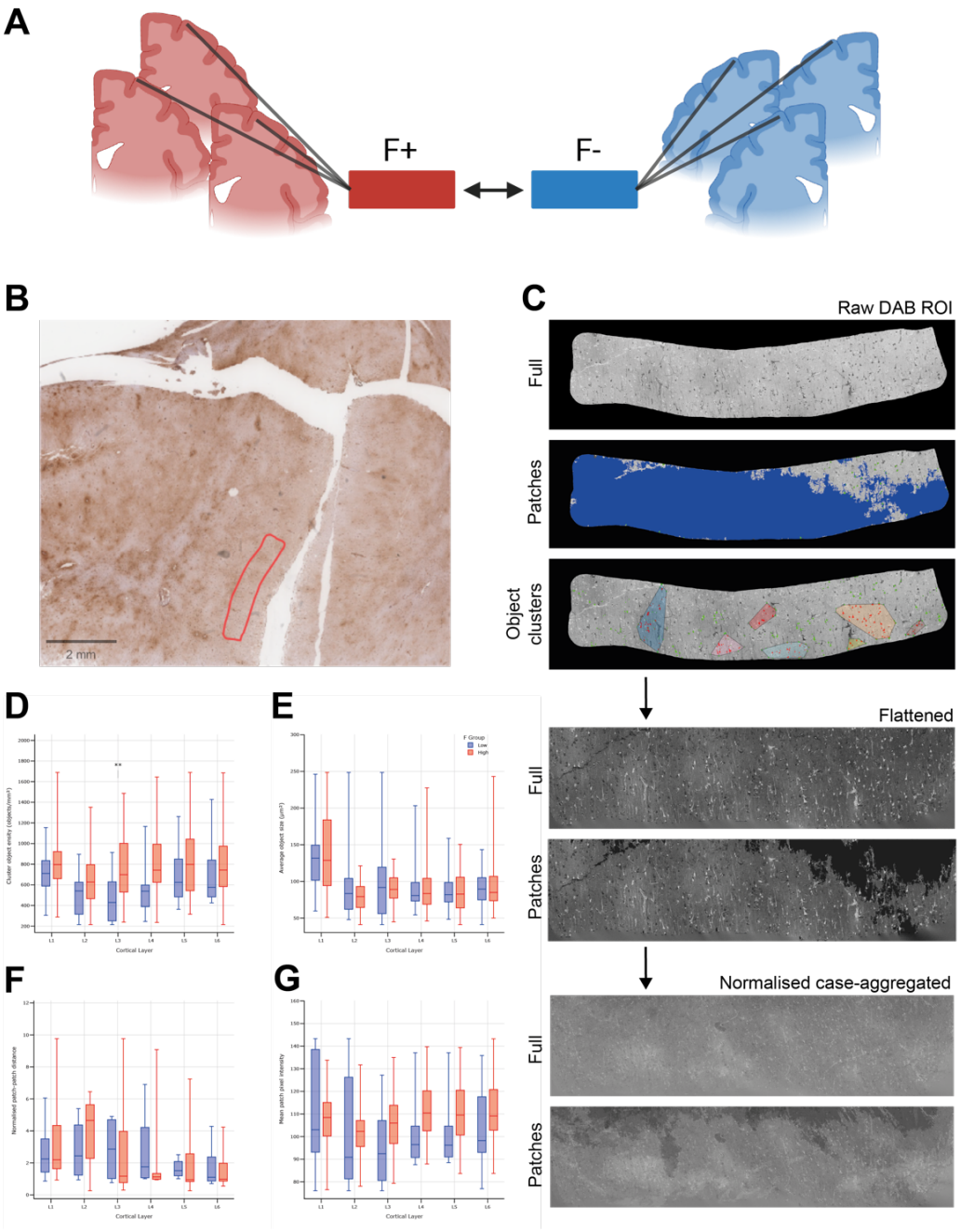

Figure 2.6. Region of interest normalisation for group-group spatial analysis of fibrinogen deposition in the motor cortex.

A, The diverse morphology of the motor cortex requires regions of interest to be mapped to a common framework for spatial analyses. **B**, Representative image of fibrinogen in the motor cortex with a layer 3 region of interest overlaid. **C**, Overview of the normalisation process. Raw regions of interest are extracted from the DAB channel of whole-slide images before fibrinogen patches (extracellular fibrinogen) and object clusters (discrete, fibrinogen-positive objects) are identified and masked and pixel, morphological, and spatial data gathered. Tissue within regions of interest is column-wise flattened to a native width, and a minimum rectangle created via random adjacent interpolation to fill required black pixels. Rearranged regions of interest are scaled to a common framework per cortical layer, and combined per case to give a size-weighted aggregated image that is later normalised across the full cohort. **D-G**,

analysis of raw data from ROIs. **D**, Density of objects within object clusters is consistently higher in F+ cases with this reaching significance in layer 3 ($p = 0.005$). No significant differences were recorded between F+ and F- groups in object cluster object size (**E**), patch-patch normalised distance (**F**), or patch mean pixel intensity (**G**). Data for each variable and within each layer was assessed for normality via Shapiro-Wilk test, and independent t-test or Mann-Whitney U test performed followed by BH correction for multiple comparisons.

2.3.12 Analysis of variation in effect size of extracellular fibrinogen deposition between high and low extracellular fibrinogen deposition cases

To determine if the difference in extracellular fibrinogen deposition between F+ and F- cases was spatially consistent, the normalised extracellular fibrinogen deposition images were compared. Normalised images were cohort-wide normalised to facilitate inter-group comparison. As these images were of exact and fixed dimensions, Cohen's d was calculated at each pixel position to show the extracellular fibrinogen effect size between groups. This was visualised as a heatmap of Cohen's d values (**Figure 2.7B**).

The proportion of pixels within 0.5 Cohen's d increments increased from cortical layers 1 through 6 (**Figure 2.7C**). Effect sizes of 0.5-1.0 were most common within layer 1 (0.66), with a downward shift seen at layer 2 where this was still the most common bucket (0.62) but the 1.0-1.5 bucket accounted for a substantial portion of pixels (0.29). Layer 3 showed a further shift towards larger effect sizes with the 1.5-2.0 bucket most prevalent (0.44) and a large contribution from the 2.0-2.5 bucket (0.25). Layer 4 was the only layer to have the greatest proportion of its pixels in the 2.0-2.5 bucket (0.41), along with a notable proportion of 2.5-3.0 (0.12) and 3.0-3.5 (0.01) pixels. Layer 4 represented the peak of overall effect

size across the cortical layers. Layers 5 and 6 showed very similar proportional contributions from each bucket, with the 1.5-2.0 bucket most frequent (layer 5 = 0.44, layer 6 = 0.46) and large contributions from the 2.0-2.5 bucket (layer 5 = 0.34, layer 6 = 0.30). Layer 5 was the only layer to feature pixels in the 3.5-4.0 bucket (0.04).

2.3.12.1 Horizontal profile analysis of extracellular fibrinogen deposition effect size variation in each cortical layer

Local variation in effect size across the normalised images was quantified within each cortical layer by using left-right sliding windows to measure the mean Cohen's d in small, overlapping regions. Results of this analysis were plotted as a line trace (**Figure 2.7D**), and each transition of ±0.2 mean Cohen's d recorded (**Figure 2.7E**).

The total transitions within each cortical layer differed, showing an increase from layer 1 to layer 4, followed by a plateau in layers 5 and 6. The contribution of up and down transitions were constant across cortical layers (**Figure 2.7E**).

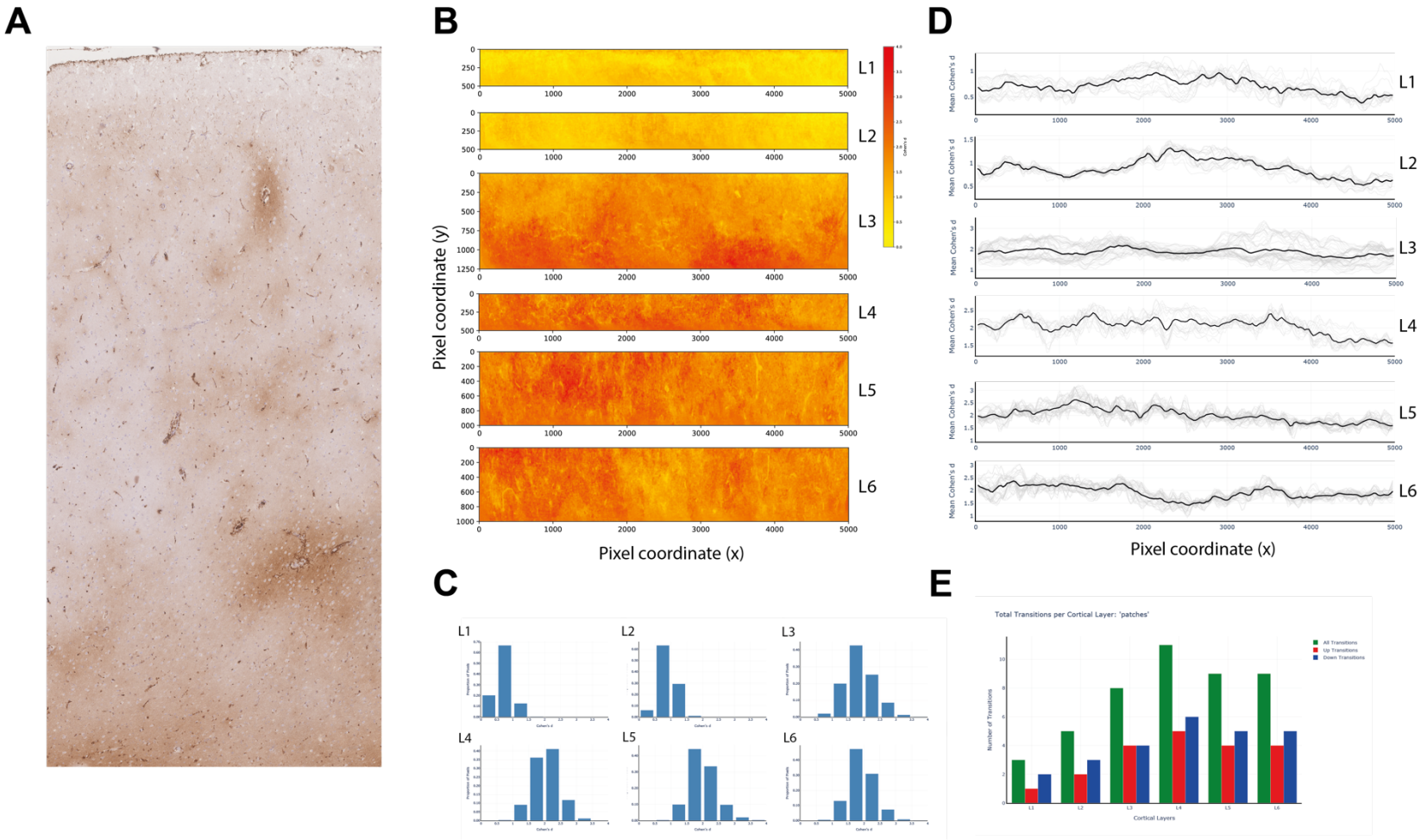

Figure 2.7. Normalisation of ROIs in high and low extracellular fibrinogen deposition cases reveals spatial heterogeneity in effect sizes.

A, Representative image of extracellular fibrinogen deposition spanning the layers of the motor cortex. **B**, Layer-by-layer heatmaps of Cohen's d were created by comparison of pixel intensities across normalised ROIs in F+ and F- MS cases. **C**, Proportions of total pixels in 0.5 Cohen's d buckets by cortical layer. **D**, Horizontal profile analysis of average Cohen's d in 50 x 50 pixel sliding windows across each cortical layer. Visualisations show average trace (black) and raw traces (grey), to illustrate

spatial variations in Cohen's d between high and low extracellular fibrinogen deposition groups. **E**, The number of ± 0.2 Cohen's d transitions in the horizontal profile analysis increases from layer 1 to layer 4. The proportion of transitions up or down does not vary by cortical layer.

2.3.13 Segmentation of neurons using NeuN DAB WSIs

Neuronal densities within the proteomic sub-cohort (n = 40) of MS cases was assessed via NeuN DAB staining. Consistent staining was achieved in 36 of these cases. Within these cases NeuN stained both pyramidal and granular neurons (**Figure 2.8A**) and facilitated the easy identification of the cortical layers.

Images were manually annotated to identify the cortical layers, and resulting layer-specific ROIs processed using a custom analysis pipeline. Neurons were classified based on cell area into small (30-75μm^2), intermediate (76-170μm^2), large (171-250μm^2), and very large (251+μm^2) classes (**Figure 2.8B**). Accuracy of image segmentation was assessed by overlaying cell masks onto the original DAB image (**Figure 2.8C, D**) and manually assessing assigned cell classifications and unclassified cells.

Each identified cell was measured to record morphological features (area coverage, circularity, eccentricity, aspect ratio) and local neuronal density within 80μm of the cell's centroid (**Figure 2.8E**). Individual measurements were saved and aggregated at the ROI level as summary statistics per measurement along with overall neuronal densities in total and per size class. ROI-level measurements were conservatively cleaned using a 1.5* IQR method to remove outliers, with any ROI with an outlier in any neuronal density dropped from future analysis.

Across the 36 cases with usable NeuN sections this pipeline recorded the expected compositions of each cortical layer, with layers 2 and 4 showing a greater proportion of small neurons, representing granule neurons, whereas

layers 3, 5, and 6 showed greater proportions of intermediate and large neurons, representing pyramidal neurons (**Figure 2.8F**). Layer 1's proportions reflect the very small number of cells detected due to its generally aneuronal nature. In total, 370,049 neurons were measured in the cleaned data, with 3014 in layer 1, 56,950 in layer 2, 122,249 in layer 3, 64,831 in layer 4, 59,778 in layer 5, and 63,227 in layer 6, providing a rich dataset for subsequent analyses.

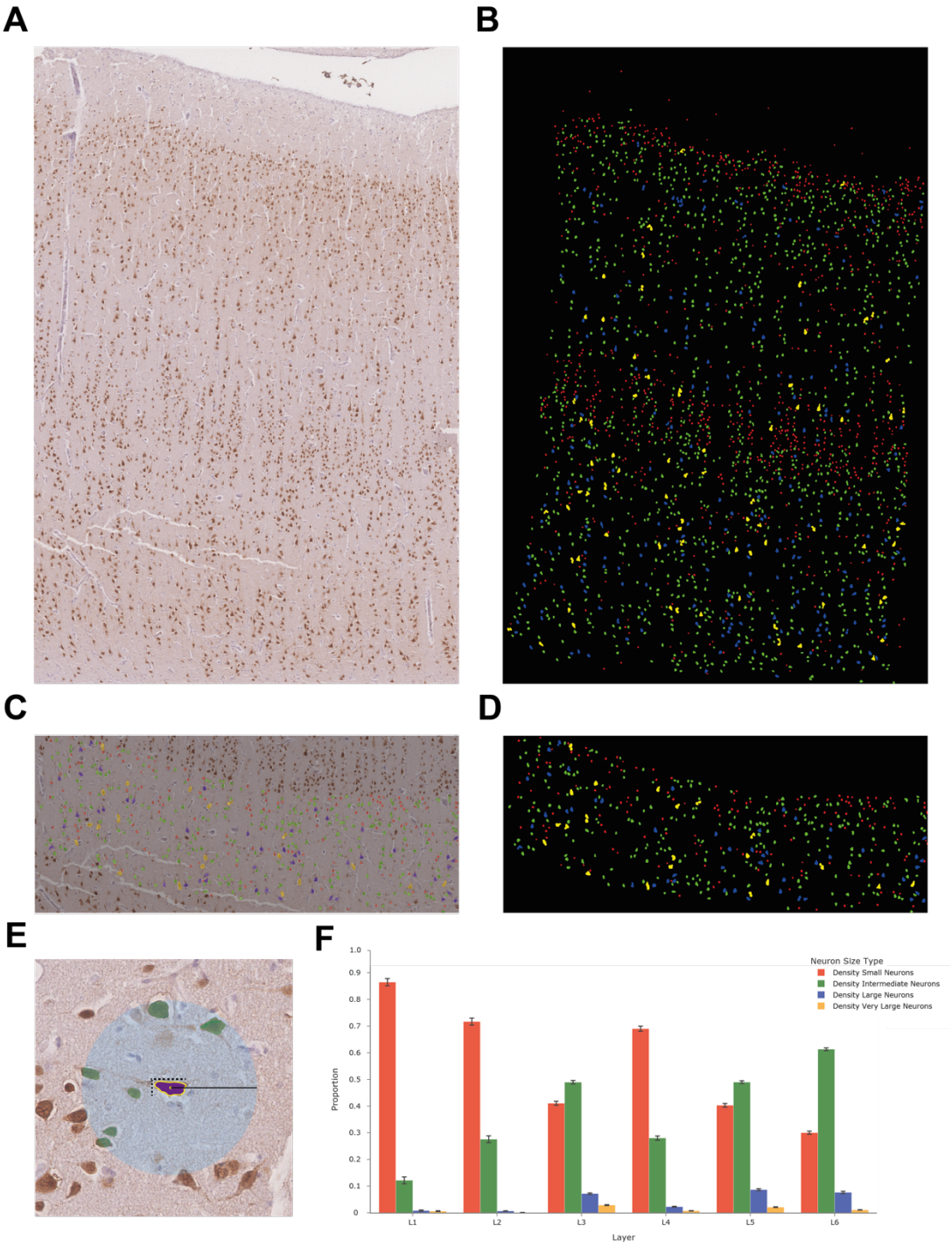

Figure 2.8. Segmentation of NeuN DAB stains allows large scale neuronal data acquisition with high granularity.

A, Representative image of NeuN DAB staining across the cortical layers. **B**, Segmentation of NeuN objects by Otsu's method and morphological operations. NeuN objects are classified by area into small (red, 30 - 75μm^2), intermediate (green, 76 – 17030 - 75μm^2), large (blue, 171 - 250μm^2), and very large (yellow, 251μm^2+) categories. **C**, Size-classified objects overlaid on original NeuN image in layer 5. **D**, Layer 5 segmented objects. **E**, Schematic of data gathered per NeuN object. Size, circularity, eccentricity, aspect ratio are recorded to provide morphological data. Local

NeuN densities are gathered per NeuN object within an 80μm radius of the object's centroid. Individual NeuN object data is recorded and aggregated at the ROI level with variability in all recorded metrics calculated per ROI. **F**, Proportions of each NeuN object size class by cortical layer. Across the cohort of 39 MS cases 370,049 NeuN objects were measured (L1 = 3014, L2 = 56950, L3 = 122,249, L4 = 64831, L5 = 59778, L6 = 63227).

2.3.14 Neuronal density and morphology differences between high and low extracellular fibrinogen deposition MS cases

MS cases in the F+ group showed significantly reduced overall neuronal density in layers 4 (p = 0.016) and 5 (p = 0.038) of the motor cortex (**Figure 2.9A**). This result was not consistent across neuronal size classes (**Figures 2.9B-E**). Small neuron density was significantly reduced in layer 3 (p = 0.027), layer 5 (p = 0.037), and layer 6 (p = 0.011). Intermediate neuron density was only significantly reduced in layer 4 (p = 0.011), which was also the only layer with significantly lower large neuron density (p = 0.006). Very large neurons were lower in layer 3 (p <0.001) and layer 4 (p = 0.002).

2.3.14.1 Local neuronal density differences in small and intermediate size neurons

Local neuronal densities provide a more granular measure of the variability around a given neuron. Small neurons (**Figure 2.9F, G**) showed significantly lower local neuronal density surrounding small neurons in the F+ group in layer 3 (p = 0.017) and layer 5 (p = 0.002), with layer 4 on the cusp of significance (p = 0.051). The standard deviation of local neuronal density surrounding small neurons was reduced only in layer 5 (p = 0.002).

Intermediate size neurons (**Figure 2.9H, I**) in the F+ group had significantly lower local neuronal densities in layer 3 (p = 0.042), layer 4 (p = 0.006), and layer 5 (p = 0.002). Standard deviation of surrounding neuronal density was only significantly reduced in layer 5 (p = 0.003).

2.3.14.2 Differences in neuron size within size classes

The F+ group showed significant changes in neuronal size (**Figures 2.9J-M**). Reduced size was observed in small neurons in layer 4 (p = 0.044), and large neurons in layer 3 (p <0.001). Intermediate neurons showed increased size in layer 3 p = 0.015). Across all neurons the standard deviation of cell size was reduced in layer 3 (p <0.001) and layer 4 (p = 0.004).

2.3.14.3 Differences in neuron morphology overall and within size classes

Morphological measures suggested more circular and less elongated neurons in the F+ group (**Figure 2.9N-T**). For total neurons mean aspect ratio was lower in layer 4 (p = 0.002) and was less variable in layer 3 (p = 0.003), layer 4 (p = 0.006), and layer 5 (p = 0.043). Circularity in total neurons was increased in layer 4 (p = 0.008) and layer 5 (p = 0.043). Variability in circularity was significantly lower in layer 3 (p <0.001), layer 4 (p <0.001), and layer 5 (p = 0.001).

These changes in circularity in the F+ group varied by neuron type (**Figure 2.9R-T**). Small neurons only showed increased circularity in layer 4 (p = 0.015). Whereas intermediate neurons showed significantly increased circularity across

layer 3 (p = 0.036), layer 4 (p = 0.009), layer 5 (p <0.001), and borderline significance for layer 6 (p = 0.059). Large neuron circularity was increased in layer 3 (p <0.001), layer 5 (p = 0.002), and borderline significance in layer 6 (p = 0.063).

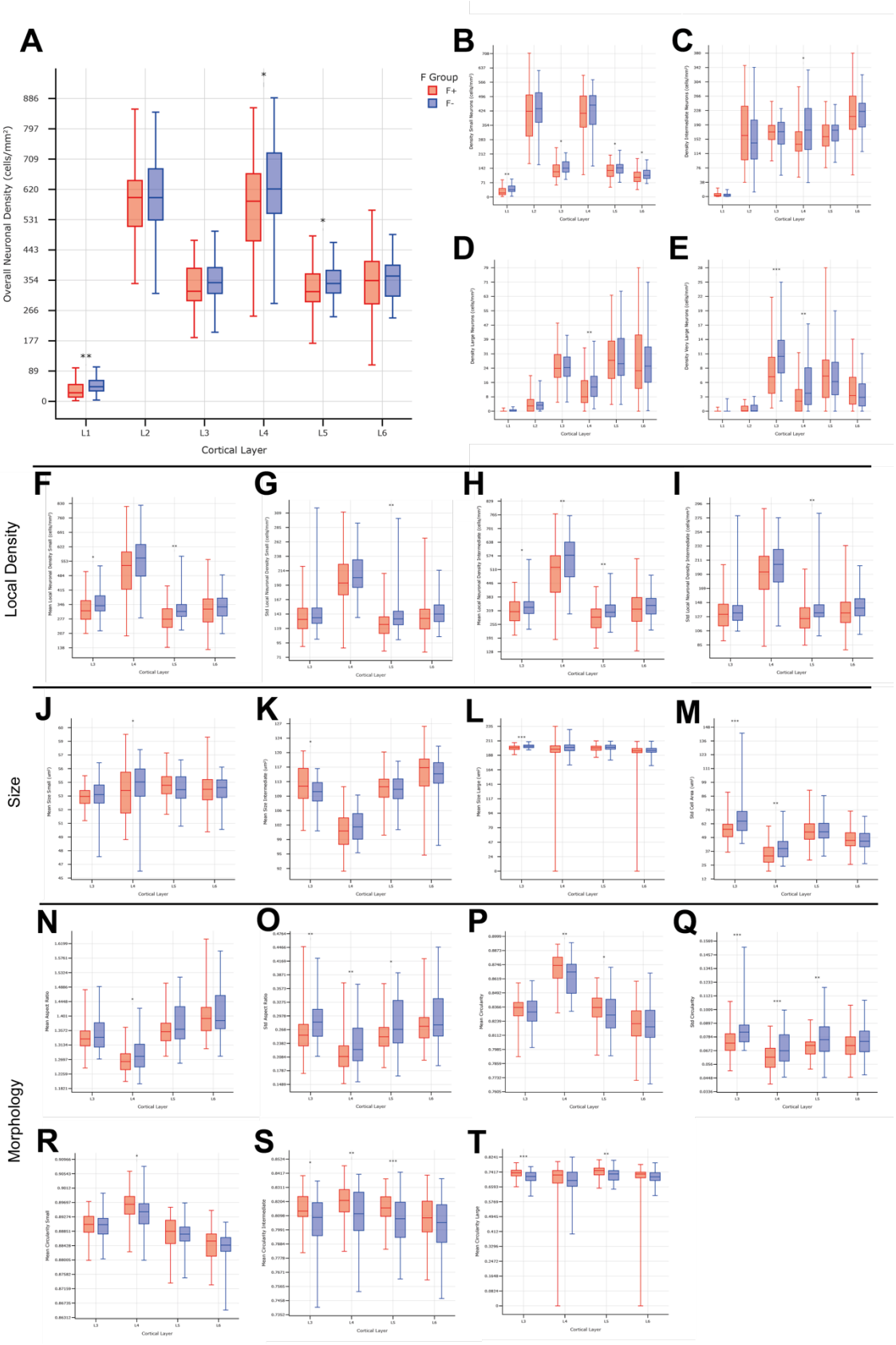

Figure 2.9. High extracellular fibrinogen MS cases show morphological changes and reduced neuronal densities.

A, Overall neuronal density is significantly reduced in F+ cases compared to F- cases. **B-E**, Reduced neuronal densities are observed in each neuronal size class but

differences are nonuniformly distributed across the cortical layers. **F-I**, Local measurements of neuronal density show significantly lower neuronal densities and standard deviation of neuronal density in F+ cases. **J-L**, Average neuronal size is reduced in F+ cases in layer 3 only. **M**, Standard deviation of neuronal size is reduced in F+ cases in layers 3 and 4. **N-Q**, Aspect ratio and circularity are altered in F+ cases and their standard deviations are reduced across layers 3, 4, and 5. **R-T**, Circularity of small, intermediate, and large neurons is increased in F+ cases but neuron size classes do not show uniform changes across the cortical layers. Statistical analyses performed within each layer were selected by testing for normality via Shapiro-Wilk test followed by independent t-test or Mann-Whitney U test. Multiple comparisons correction was not used.

2.3.15 Linear mixed models of the effects of demographic, clinical, genetic, and morphological variables on neuronal density in MS cases.

Linear mixed models were used to investigate the individual influence of demographic and clinical variables, HLA DRB1*1501 status, and layer 5 extracellular fibrinogen semi-quantitative score on neuronal densities.

In these models all continuous predictors and dependent variables were scaled to have a mean of 0 and SD of 1.0. Consequently, β represents the effect on the dependent variable in SD of a 1 SD increase in the predictor whilst holding all other predictors at their mean. HLA DRB1*1501 positive status was treated as a Boolean.

Interaction terms between predictors were explored but were found to not improve model fit and lack significance. The results of these models are shown in **Table 2.4**.

2.3.16 Small neuron associations

Layer 5 extracellular fibrinogen semi-quantitative score significantly negatively associated with small neuron density across layers 3, 4, and 5. This effect size was greatest in layer 4 (β = -0.215, p = 0.001), and smaller in layer 3 (β = -0.091, p = 0.002) and layer 5 (β = -0.060, p = 0.015).

Local small neuron density SD positively associated with small neuron density across all cortical layers assessed.

Mean circularity of small neurons positively associated with small neuron density across all layers, with a particularly large association in layer 4 (β = 0.992, p <0.001). Overall neuronal circularity SD negatively related to small neuron density in layers 4, 5, and 6. Mean eccentricity of small neurons was positively associated with small neuron density in layer 4 (β = 0.577, p <0.001) and layer 6 (β = 0.112, p <0.001).

2.3.16.1 Intermediate neuron associations

The association between layer 5 extracellular fibrinogen semi-quantitative score and neuronal density was strongest in intermediate neurons, with significant negative relationships with intermediate neuron density in layer 3 (β = -0.181, p = 0.002), layer 4 (β = -0.188, p <0.001), layer 5 (β = -0.209, p = 0.002, and layer 6 (β = -0.168, p = 0.018).

Local intermediate neuronal density SD was positively related to intermediate neuronal density across all cortical layers assessed.

Mean circularity of intermediate neurons demonstrated a very strong positive relationship with intermediate neuron density across all cortical layers assessed. Overall neuronal circularity showed a positive association with intermediate neuron density in layer 4 only (β = 0.625, p <0.001). Mean eccentricity of intermediate neurons was positively associated intermediate neuronal density at a lesser but still strong level.

Mean size of intermediate neurons positively related to intermediate neuron density in layer 4 (β = 0.500, p = 0.012) layer 5 (β = 0.735, p <0.001), and layer 6 (β = 0.723, p <0.001).

Intermediate neurons showed the highest inter-case variance of the three neuron classes investigated.

2.3.16.2 Large neuron associations

The relationship between layer 5 extracellular fibrinogen semi-quantitative score and large neuronal density was non-significant across all cortical layers assessed. However, this relationship approached significance in layer 3 (β = -0.099, p = 0.061) and layer 5 (β = -0.166, p = 0.087).

Local density surrounding large neurons was not significantly associated with large neuron density in any cortical layer.

Mean circularity of large neurons was strongly positively associated with large neuronal density across all cortical layers assessed. SD of total neuronal

circularity was positively associated with large neuron density across all cortical layers.

Mean size of large neurons was positively associated with large neuron density in layer 3 (β = 1.782, p = 0.021) and layer 5 (β = 2.743, p =<0.001).

2.3.16.3 HLA-DRB1*1501 positivity and neuronal density

HLA-DRB1*1501 positive status was associated with significantly reduced layer 4 densities of small (β = -0.379, p = 0.018) and intermediate (β = -0.298, p = 0.004) neurons. Intermediate neurons in layer 5 (β = -0.208, p = 0.105) and layer 6 (β = -0.263, p = 0.078) were close to significance.

Table 2.4. Extracellular fibrinogen and neuronal density linear mixed models

Regression coefficients from linear mixed models to assess the influence of extracellular fibrinogen on neuronal density

	Layer 3 (n = 33)		Layer 4 (n = 34)		Layer 5 (n = 32)		Layer 6 (n = 36)	
Small neuron models	β (95% CI)	Adj *p* value	β (95% CI)	Adj *p* value	β (95% CI)	Adj *p* value	β (95% CI)	Adj *p* value
HLA-DRB1*1501 positive	0.016 (-0.103 - 0.135)	0.795	-0.319 (-0.583 - -0.055)	0.018	0.007 (-0.088 - 0.102)	0.885	0.005 (-0.075 - 0.085)	0.896
Circularity SD	-0.062 (-0.135 - 0.010)	0.093	-0.196 (-0.349 - 0.043)	0.012	-0.111 (-0.168 - -0.005)	<0.001	-0.089 (-0.133 - -0.044)	<0.001
Mean circularity small	0.211 (0.066 - 0.357)	0.004	0.992 (0.669 - 1.316)	<0.001	0.122 (0.014 - 0.230)	0.027	0.125 (0.058 - 0.192)	<0.001
Mean size small	0.079 (-0.034 - 0.192)	0.172	0.052 (-0.131 - 0.234)	0.578	0.005 (-0.087 - 0.098)	0.909	0.021 (-0.053 - 0.095)	0.572
Local small density SD	0.104 (0.037 - 0.170)	0.002	0.418 (0.285 - 0.550)	<0.001	0.200 (0.147 - 0.252)	<0.001	0.169 (0.121 - 0.218)	<0.001
Mean eccentricity small	0.113 (-0.004 - 0.229)	0.058	0.577 (0.367 - 0.788)	<0.001	0.057 (-0.022 - 0.136)	0.160	0.112 (0.051 - 0.172)	<0.001
L5 extracellular SQ score	-0.091 (-0.149 - -0.033)	0.002	-0.215 (-0.343 - -0.086)	0.001	-0.060 (-0.109 - -0.011)	0.016	-0.023 (-0.061 - 0.015)	0.227
Age at death	0.007 (0.000 - 0.013)	0.044	0.006 (-0.008 - 0.020)	0.384	0.002 (0.003 - 0.008)	0.431	0.000 (-0.005 - 0.004)	0.909
Disease duration	-0.005 (-0.012 - 0.002)	0.150	-0.010 (-0.024 - 0.005)	0.190	-0.001 (-0.007 - 0.005)	0.776	0.003 (-0.001 - 0.008)	0.174
Group Var	1.005		0.755		0.625		0.703	
Intermediate neuron models								
HLA-DRB1*1501 positive	-0.103 (-0.340 - 0.134)	0.394	-0.298 (-0.500 - -0.096)	0.004	-0.208 (-0.460 - 0.044)	0.105	-0.263 (-0.556 - 0.030)	0.078
Circularity SD	0.035 (-0.125 - 0.195)	0.667	0.652 (0.475 - 0.829)	<0.001	-0.077 (-0.222 - 0.068)	0.299	0.008 (-0.193 - 0.210)	0.934
Mean circularity intermediate	3.521 (2.115 - 4.928)	<0.001	4.310 (3.148 - 5.472)	<0.001	3.378 (1.939 - 4.817)	<0.001	4.665 (2.811 - 6.518)	<0.001
Mean size intermediate	0.323 (-0.064 - 0.710)	0.102	0.500 (0.111 - 0.888)	0.012	0.735 (0.393 - 1.078)	<0.001	0.723 (0.347 - 1.099)	<0.001
Local intermediate density SD	0.149 (0.007 - 0.292)	0.040	0.290 (0.172 - 0.408)	<0.001	0.199 (0.071 - 0.328)	0.002	0.479 (0.290 - 0.669)	<0.001
Mean eccentricity intermediate	0.399 (0.005 - 0.794)	0.047	0.584 (0.186 - 0.982)	0.004	0.732 (0.353 - 1.111)	<0.001	1.198 (0.697 - 1.698)	<0.001
L5 extracellular SQ score	-0.181 (-0.297 - -0.064)	0.002	-0.188 (-0.292 - -0.083)	<0.001	-0.209 (-0.340 - -0.079)	0.002	-0.168 (-0.307 - -0.029)	0.018
Age at death	0.001 (-0.012 - 0.014)	0.926	-0.005 (-0.016 - 0.005)	0.325	0.000 (-0.014 - 0.015)	0.982	0.003 (-0.013 - 0.019)	0.683
Disease duration	-0.008 (-0.022 - 0.005)	0.227	-0.006 (-0.017 - 0.005)	0.308	-0.006 (-0.021 - 0.009)	0.450	-0.004 (-0.021 - 0.013)	0.666
Group Var	1.327		0.329		1.627		1.167	
Large neuron models								
HLA-DRB1*1501 positive	-0.138 (-0.350 - 0.073)	0.200	-0.072 (-0.242 - 0.097)	0.404	-0.298 (-0.664 - 0.068)	0.110	-0.228 (-0.599 - 0.144)	0.230
Circularity SD	0.618 (0.435 - 0.802)	<0.001	0.514 (0.390 - 0.638)	<0.001	0.673 (0.413 - 0.993)	<0.001	1.110 (0.842 - 1.378)	<0.001
Mean circularity large	3.359 (2.117 - 4.600)	<0.001	0.640 (0.317 - 0.964)	<0.001	5.148 (3.354 - 6.942)	<0.001	1.985 (1.027 - 2.943)	<0.001
Mean size large	1.781 (0.264 - 3.298)	0.021	-0.124 (-0.544 - 0.296)	0.562	2.743 (1.150 - 4.336)	<0.001	0.253 (-1.106 - 1.612)	0.715
Local large density SD	-0.216 (-0.461 - 0.029)	0.083	0.017 (-0.048 - 0.082)	0.614	0.229 (-0.062 - 0.521)	0.123	0.182 (-0.145 - 0.510)	0.276
Mean eccentricity large	-0.381 (-1.118 - 0.355)	0.310	-0.331(-0.578 - -0.083)	0.009	0.780 (-0.240 - 1.800)	0.134	-1.873(-2.617 - -1.128)	<0.001
L5 extracellular SQ score	-0.099 (-0.203 - 0.005)	0.061	-0.058 (-0.144 - 0.029)	0.190	-0.166 (-0.356 - 0.024)	0.087	0.009 (-0.170 - 0.188)	0.922
Age at death	0.000 (-0.012 - 0.011)	0.961	-0.002 (-0.010 - 0.006)	0.600	0.004 (-0.025 - 0.016)	0.685	-0.001 (-0.021 - 0.018)	0.888
Disease duration	-0.015 (-0.027 - -0.003)	0.013	-0.006 (-0.014 - 0.003)	0.221	-0.012 (-0.034 - 0.010)	0.285	0.002 (-0.019 - 0.023)	0.856
Group Var	0.308		0.217		0.431		0.192	

2.4 Discussion

The extensive heterogeneity of fibrinogen deposition, coupled with demographic and clinical variability, complicates our understanding of fibrinogen extravasation-specific effects within the MS motor cortex. In this study we address these challenges by conducting fine-grained analysis of how fibrinogen deposition types relate to demographic and clinical variables, vary spatially, and impact neuronal densities across a large human postmortem cohort. We demonstrate that extracellular fibrinogen exerts a mild negative effect on neuronal density, and that this effect varies by neuronal size and cortical layer. Our study suggests intensive fibrinogen deposition is required for significant neuronal loss, presenting vascular integrity as a promising target for therapeutic investigation.

Each of the fibrinogen deposition patterns described in this study (**Figure 2.3B-L**) have been described previously other neurological conditions, or animal models, but not in MS. Early work by Lømberg and Torvik using a rat model of focal BBB disruption demonstrated uptake of fibrinogen by lesion-proximal neurons and passing axons within minutes of lesioning. Fibrinogen positivity within neurons lasted 48-96 hours before clearance[211]. More recently perivascular as well as neuronal and astrocytic fibrinogen-positivity has also been demonstrated to occur within hours of concussion in a swine model, with positive area decreasing, but remaining elevated to baseline over 6-72 hours[212]. A study of tissue surgically resected from a variety of brain regions in epileptic patients showed extensive fibrinogen-positivity of neurons and glial cells in the area surrounding the surgical site in all cases, and that the burden of positivity positively correlated with time between electrode insertion and extraction[213]. Beyond these relatively acute examples, fibrinogen deposition has been recorded in human

neuropathological studies of cardiovascular disease (CVD) (perivascular)[214], periventricular white matter hyperintensities (white matter astrocyte, neuron, perivascular)[215,216], SVD (astrocyte, neurite, capillary, WM axon, perivascular)[204,217], AD (extracellular, neuron, grey matter astrocyte, microglia, perivascular)[201,218], and cerebral malaria (perivascular, grey matter astrocyte)[219].

Collectively this body of work suggests fibrinogen deposition into different compartments within the brain to be a general mechanism of extravasation, with intracellular fibrinogen likely to be transient. Our findings that the presence of intracellular fibrinogen deposition types positively correlate with each other and with extracellular fibrinogen, but do not correlate with demographic or clinical features (**Figure 2.3N**) supports this interpretation. It is reasonable that the clusters of cases identified from fibrinogen deposition types did not differ with regards to demographic and clinical variables for the same reason (**Figure 2.3O-Q**).

The mechanism of fibrinogen uptake into the diverse range of cells in which it is seen in the cortex has not been delineated. However, a promising candidate for this is endocytic cell surface receptor LRP1, which has been demonstrated as binding fibrinogen[220], likely via the N-terminus of fibrinogen α chain[221]. LRP1 has been demonstrated to mediate neuronal[222] and astrocytic[223] endocytosis of Aβ in human cell lines and the APP/PS1 mouse model of AD. α-Synuclein endocytosis by neurons and subsequent spread has also been demonstrated in model systems[224]. A large number of studies have demonstrated neuronal and astrocytic LRP1 expression in AD samples[225]. Oligodendrocyte progenitor cell LRP1 has been described and investigated in a range of mouse models[226,227], including in EAE and cuprizone models of inflammatory demyelination[228]. Given LRP1 is the only known endocytic receptor of

fibrinogen present on each of the cell types intracellular fibrinogen was observed within in this study, it is most likely a significant facilitator of intracellular fibrinogen in the MS motor cortex.

We demonstrate that in addition to exhibiting diverse deposition patterns, fibrinogen intensity shows significant spatial variability over small tissue depths (**Figure 2.5**), and across single sections (**Figure 2.7**). The primarily hepatic production of circulating fibrinogen[4], as well as robust animal models showing fibrinogen extravasation in the brain only after BBB disruption[211,212], and the perivascular deposition observed in our study (**Figure 2.3K,L**) and others[201,204,214–219], strongly supports impaired BBB integrity as the gateway to fibrinogen deposition in the MS motor cortex. The differences we observed in magnitude of effect size and frequency of effect size transitions for extracellular fibrinogen deposition (**Figure 2.7B-E**) therefore likely reflect the layer-specialised nature of cortical vascular supply and differences in vascular density[229,230], coupled with the myriad locally-variable triggers of BBB impairment seen in MS[231] and ageing[232].

Our study's most notable findings are the confirmation of reduced overall neuronal density in the motor cortex of F+ MS cases (**Figure 2.9A**), the identification that this effect differs by cortical layer and neuron size (**Figure 2.9B-E**), that neurons in F+ cases display altered morphologies (**Figure 2.9N-T**), and the delineation of the independent effect size of extracellular fibrinogen deposition on small, intermediate, and large neuronal densities in layers 3-6 (**Table 2.4**). We also report for the first time a consistent negative association between HLA DRB1*1501 positive status and neuronal density, with this reaching significance in layer 4 small and intermediate

neurons (**Table 2.4**). Together these findings support the hypothesis that neurodegeneration is a feature within the NAGM of the MS motor cortex.

Fibrinogens effects on neuroinflammation and deleterious neuronal consequences are thought to occur primarily downstream of microglia binding fibrinogen via the CD11b/CD18 receptor, and resulting ROS production[233]. This mechanism has been shown to induce dendrite and dendritic spine loss in the 5XFAD AD mouse model, with spine loss preventable by either ROS inhibition or CD11b KO[202]. The binding of fibrinogen to Aβ, leading to persistent degradation-resistant fibrin has also been reported in mice[234], with work in organotypic hippocampal cultures demonstrating synapse loss inhibitable via lecanemab application[235]. Neuronal loss attributable to fibrinogen has been shown in murine TBI, with this loss prevented in mice lacking FGGs CD11b/CD18 binding motif[236]. The direct interaction between fibrinogen and neurons has only explored in mouse neural cultures, where soluble fibrinogen caused neuronal death downstream of ROS, nitrite, and superoxide production[237].

The focus on extracellular grey matter fibrinogen deposition (**Figure 2.3E**, **Figure 2.4G**) and its relation to neuronal densities (**Table 2.4**) in this study likely reflected an investigation of the both extravasated soluble fibrinogen and persistent fibrin aggregates that arise from thrombin-mediated cleavage of fibrinogen and require proteolytic cleavage to clear[4,51]. It is prudent to consider that these forms of fibrinogen/fibrin may interact differently with neurons and glial cells. As previously discussed, neurons and astrocytes likely possess endocytic capacity for fibrinogen via the LRP1 receptor binding the fibrinogen α chain[220,221], providing an avenue for uptake of soluble fibrinogen. However, within fibrin aggregates the α chain is at least partially obstructed by the half-staggered structure of the individual fibres[51,58]. Microglial

CD11b/CD18 has the capacity to bind fibrinogen at multiple locations of the β and γ chains[238], with at least the γ chain epitope at amino acids 377-395 bindable within fibrin aggregates[78,79]. Notably, inhibition or ablation of this epitope minimises the proinflammatory microglial response to fibrinogen in a variety of animal models[202,236,239]. The non-vessel associated extracellular deposition we see may therefore represent a chronic, low-level, source of microglial inflammation leading to synapse loss, and subsequent neuronal death. Different neuron sizes may respond differently to this by virtue of the proportional effect of synapse loss varying by cell size, or larger neurons having greater antioxidant reserve.

In summary, we expand upon our understanding of fibrinogen deposition and sequelae in the MS motor cortex, positioning fibrinogen as a locally variable mediator of neuronal loss. Future work assessing the direct spatial relationships between fibrinogen, microglia, and neurons within distinct tissue microenvironments and model systems, combined with *in vivo* imaging of cerebrovascular disruption, offer the potential to understand fibrinogen's neurodegenerative effects in practise.

Chapter 3 | Proteomic analysis of microglia in layer 5 of the multiple sclerosis motor cortex in high and low extracellular fibrinogen contexts

3.1 Introduction

In the preceding chapter, we demonstrated the extensive heterogeneity of fibrinogen deposition in the MS motor cortex, confirming the negative association between extracellular fibrinogen and neurons of varying sizes across the cortical layers. While this work offers insights into the variability of fibrinogen deposition and its consequences, the mechanisms driving these responses remain poorly understood. Microglia are well established as the primary effectors of the neuroinflammatory cascade following fibrinogen extravasation, with microglial interactions with the CD11b/CD18 integrin receptor facilitating deleterious responses to both soluble fibrinogen and aggregated fibrin[205,233]. However, the microglial response to fibrinogen within the context of the human brain is poorly understood, particularly at a region-specific or spatially resolved level. This presents a major obstacle to understanding how microglial might exert their neurotoxic effects in MS.

To elucidate the mechanisms underlying this response in the MS motor cortex, we employed laser capture microdissection (LCM) and mass spectrometry to obtain layer 5-specific microglia-enriched proteomic profiles from the NAGM of a large cohort of well-characterised MS and control cases. This approach allowed us to isolate and interrogate the protein composition of a specific cellular population within an area of the cortex vulnerable to neurodegeneration. This work significantly expands our understanding of fibrinogen-microglia mediated mechanisms in the pathology of MS.

3.2 Methods

3.2.1 Study population

A sub-cohort (n = 40) of the human autopsy cohort of pathologically confirmed MS cases (n = 71) and control cases (n = 7) obtained from the Multiple Sclerosis and Parkinson's Tissue Bank at Imperial College, London, was used. Appropriate ethical approval was obtained (REC 08/MRE09/31+5) and all tissue was used in strict compliance with the conditions of the UK Human Tissue Act (2004).

MS cases within this sub-cohort were matched for demographic and clinical variables, as well as HLA DRB1*1501 status. MS cases were grouped as F+ or F- as determined by extracellular fibrinogen deposition semi-quantitative score in layer 5. Details of this cohort are shown in **Table 2.3**.

3.2.2 Immunohistochemistry

For LCM use serial 10μm-thick sections of the motor cortex were cut using a microtome and mounted onto DIRECTOR slides (Leica Microsystems) prior to air-drying and storage. At point of use sections were deparaffinised using 1.7% dishwasher soap and processed following the same procedure as in **2.2.2** with the exception that Hoechst 33342 was applied as a positive nuclear stain in place of haematoxylin counterstaining. Sections were labelled with polyclonal TMEM119 raised in rabbit to allow microglia to be identified. Sections were airdried and stored at -80°C.

Table 3.1. IHC antibodies

Antigen	Host species	Antigen-retrieval	Dilution	Supplier	Catalogue number
TMEM119	Rabbit	Autoclave Ttis-EDTA (pH 9.0)	1:1500	Sigma	HPA-0511870

3.2.3 Laser-capture microdissection of layer 5 microglia in the motor cortex

TMEM199 stained sections were defrosted at room temperature prior to loading into a Leica LMD7 laser-capture microdissection microscope with fluorescent modules (Leica Microsystems). The DAPI channel was used to visualise nuclei and identify layer 5 of the motor cortex as the area adjacent to the dense band of nuclei seen in layer 4 and covering half of the distance to the WM. TMEM119+ cells were then identified using brightfield. Circular markers with a diameter of 90μm was placed to cover the microglial soma and processes. Approximately 1100 microglia were sampled per case, with the number of sections used variable by staining quality and microglial density. Cell regions were excised and collected directly into the cap of a 0.5ml Eppendorf tube containing RIPA lysis buffer (Thermo Fisher Scientific). Lysate was stored at -80°C until use.

3.2.4 Proteomic processing of microglial lysates

A modified single-pot solid-phased-enhanced sample-preparation (SP3) method was followed for purification and digestion of lysates[240]. Lysates were heated and subsequently incubated with benzonase, followed by separate dithiothreitol and iodoacetamide incubations. A 1:1 carboxylate-modified paramagnetic bead mix (Sera-Mag Speed Beads A: ThermoFisher Scientific, USA; 09-981-121; Sera-Mag Speed

Beads B: ThermoFisher Scientific, USA; 09-981-123) was then added and the lysate-bead mix digested overnight at 37°C using 5µl of 5ng/µl trypsin.

0.5µl of each post-trypsin digestion sample was combined to create a pooled sample to increase depth of later proteomic analysis

Peptides were analysed using an Evosep One (Evosep) coupled to a timsTOF Pro mass spectrometer (Bruker, USA) using a 75 µm x 150 mm C18 column packed with 1.9 µm beads (Evosep, EV1112). The pre-set "Whisper 20 samples per day" method was used, resulting in a method duration of 60 minutes at a flow rate of 100 nL/min. The mass spectrometer was operated in diaPASEF mode using 16 diaPASEF scans per TIMS-MS scan. The ion mobility range was set to 0.6 – 1.6 Vs/cm^2. Each mass window isolated was 25 m/z wide, ranging from 475-1000 m/z with an ion mobility-dependent collision energy that increased linearly from 20 eV to 59 eV between 0.6 – 1.6 Vs/cm^2.

Proteins samples acquired using DIA were analysed using DIA-NN's (v1.8.1) deep learning spectral prediction to generate an in-silico spectral library. The spectral prediction was based on the UniProt human database (20,421 sequences) with tryptic specificity allowing for two missed cleavages and a fixed modification of carbamidomethylation. Protein and peptide FDR were set to 1%, and the "match-between-runs" option was used. All remaining settings were left as default.

3.2.5 Quality control of proteomic data

Downstream analysis of the DIA-NN output .txt file performed using Python with the pandas. NumPy, and SciPy libraries. Raw intensity values were log2

transformed, low-coverage (<70% of cohort) proteins dropped, missing values median imputed, and samples normalised via subtraction of the median log2-transformed intensity of all proteins within the sample.

Following quality control 3729 proteins were present in the cleaned dataset.

Case metadata was merged with the cleaned proteomic data to give a single wide format data frame stored as a .tsv file.

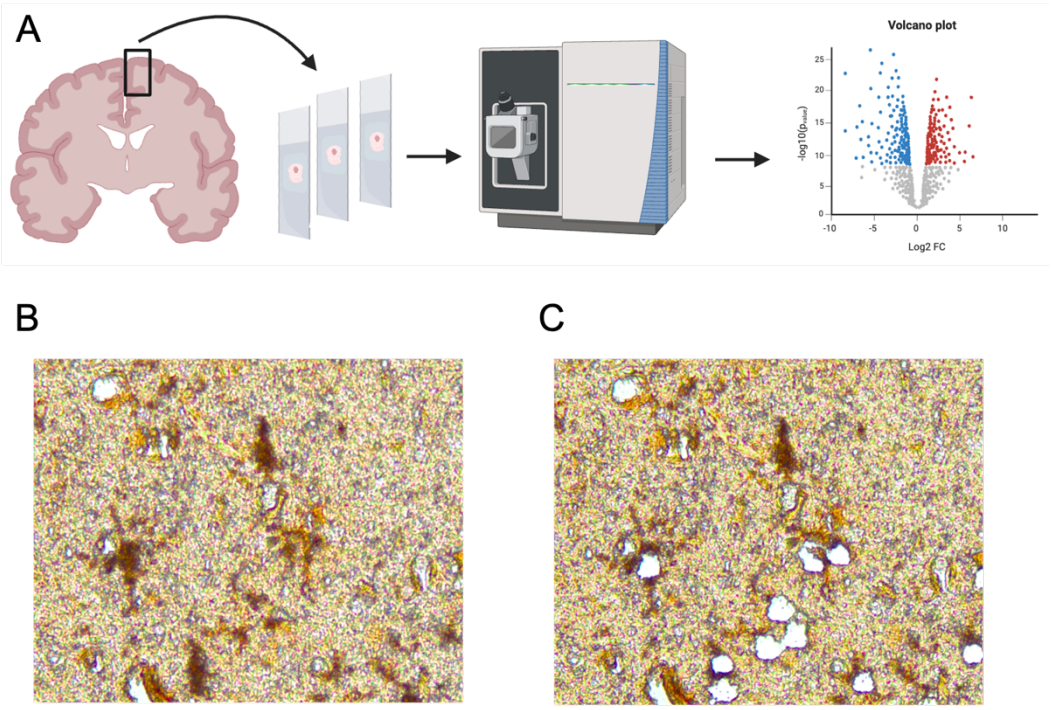

Figure 3.1. Proteomic analysis method. **A**, schematic of proteomic method. Sections of motor cortex were stained for TMEM119 and processed to isolate microglia-enriched environments prior to mass spectrometry processing and proteomic analyses. **B, C**, Representative pre (**A**) and post (**B**) laser-capture microdissection TMEM119 section.

3.2.6 Clustering and dimensionality reduction of proteomic data

The scikit-learn and scipy libraries were used for clustering analysis of normalised proteomic data.

Normalised protein expression data was standardised using the library StandardScaler. PCA using the top 3 principal components was then performed. K-means clustering using 3 clusters as defined by the input groups (F+, F-, control), and a random state of 42, was fitted to the PCA-transformed data.

OLS regression models using the principal components as the dependent variable and each demographic/clinical variable as intendent variables.

A t-SNE with perplexity 30, 3000 iterations, and random state of 42 was generated using the normalised and standardised data.

Spearman rank correlation coefficients were calculated between all pairs of samples and hierarchical clustering performed by deriving a distance matrix from the absolute correlation coefficients by subtracting from 1.

3.2.7 Proteomic differential expression analysis

The NumPy, pandas, scipy, statsmodels, and gseapy libraries were used for differential expression analysis.

Normalised proteomic data was loaded, and samples categorised into F+, F-, and control using the associated metadata. Differential expression analysis was

performed between specified groups, group means calculated, and lof2 fold change calculated as the difference between the group means. Independent two-sample t-tests for each protein were performed and BH correction applied at 0.1 to control for false discovery rate.

Following statistical advice from a senior domain-knowledgeable statistician, the F+ vs F- comparison involved an additional step in the differential expression analysis. A $\pm$ 0.5 log2 fold change filter was applied to restrict the comparisons between these groups to only large difference proteins, providing fewer hypotheses to test and increasing power amongst remaining proteins. Results were plotted as volcano plots.

3.2.8 Untargeted pathway enrichment analysis

Proteins identified as significantly differentially expressed between groups were assessed using human gene lists (GO biological process, GO molecular function, GO cellular component) and Enrichr (gseapy). Enrichr-produced combined scores using BH-corrected p values were used to select the top 10 pathways up and down regulated for each GO category. Results were plotted as bar plots.

3.2.9 Targeted pathway enrichment analysis

To provide targeted analysis of biologically relevant pathways a curated list of 46 GO terms and manually selected gene lists was used. Within each GO term

or gene list differential expression analysis between specified groups was performed as per **3.2.7**. Results were plotted as volcano plots and heatmaps.

3.2.10 STRING network analysis

Significant proteins from the untargeted differential expression analysis were assessed for interactivity by passing the list of proteins to the STRING API and recording only interactions with a combined score >700.

First-neighbour proteins, defined here as proteins not detected in our analysis but with direct interactions with our significant proteins, were identified by using the STRING API to return a list of all interacting proteins for each significant protein passed. This response was parsed and saved for future use.

3.2.11 Analysis of putative functional interactions between astrocyte subtypes and microglia from high fibrinogen contexts.

An unpublished dataset of LCM astrocyte data across all layers of the motor cortex was used to identify unique expression of proteins in the GFAP+, ALDHL1+, and GFAP+/ALDH1L1+ astrocyte subtypes. Differential expression analysis as in **2.2.6** (FDR 0.05) was performed between each unique astrocyte subtype pair. The lists of significantly upregulated proteins in each astrocyte subtype were then compared to identify significantly upregulated proteins unique to each astrocyte subtype.

Astrocyte subtype-unique proteins were then cross-referenced with the first neighbour network identified following **2.2.9**. Where a first neighbour match occurred the pair of proteins was saved. Matched astrocyte proteins were then mapped to GO terms from the GO biological processes category.

Outputs were visualised as a graph with nodes coloured by the average fold change of the microglial partner in each protein pair.

3.2.12 Gene set enrichment analysis

Normalised protein expression data was analysed using gene set enrichment analysis (GSEA) via the gseapy library. Differential expression analysis was performed between the F+ and F- groups to generate t-statistics and p values. A ranked list was then generated using the t-statistics. The ranked list was then processed for GSEA using gseapy for GO biological process, GO cellular component, and GO molecular function. Up and down regulated gene sets were identified via normalised enrichment score values. Gene sets were then filtered to ensure an FDR q-value of ≤ 0.25. Results were visualised as dot plots containing up to 20 significant gene sets.

3.3 Results

3.3.1 Study population

A sub-cohort of demographically and clinically matched MS cases and controls were used for proteomic analysis of layer 5 microglia. Details of cases are found in **Table 2.3**. Of this sub-cohort, one MS case (MS062) failed the proteomic processing and could not be included in subsequent analyses.

3.3.2 Clustering of layer 5 microglia from high and low fibrinogen multiple sclerosis motor cortex, and controls

Unsupervised PCA to identify principal components accounting for the greatest variation in the dataset was performed (**Figure 3.2A**). The resulting 2D PCA scatter plot accounting for 31.64% of variance in the dataset did not show clear separation of F+, F-, and control cases. To rule out the influence of demographic and clinical variables of this lack of group separation PC1 and PC2 were used as dependent variables in OLS regression models (**Figure3.2B-I**). CSF pH was identified as a significant negatively correlated variable with PC1 (R^2 = 0.16, r = -0.32, p = 0.0306), whilst all other demographic and clinically variables had nonsignificant effects on PC1 and PC2.

K-means clustering of the PCA output using a K of 3 did not group cases into intuitive groups (**Figure 3.2J**). Clusters did not differ with respect to any demographic or clinical variable as determined by one-way ANOVA (supplementary figure 6.1A-E) and did not show notably different proportions of F+, F-, or control cases (supplementary figure 6.1F).

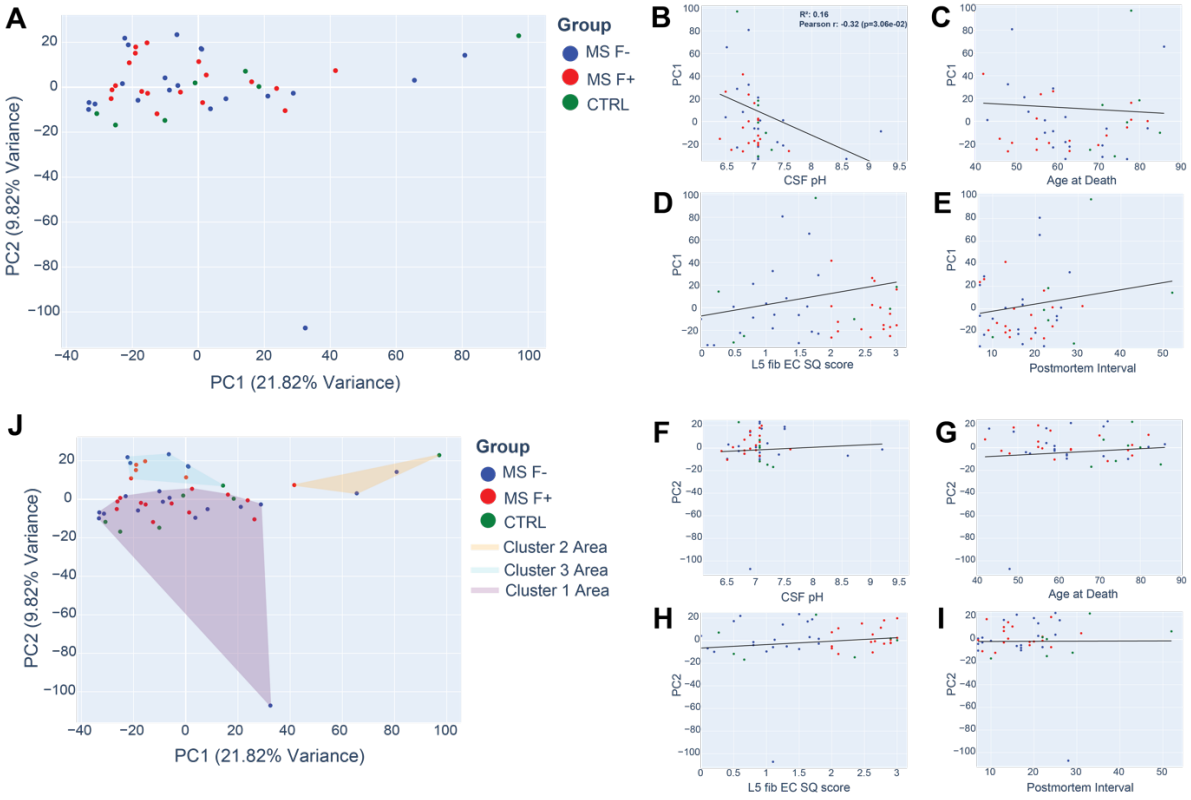

Figure 3.2. Laser-capture microdissection of microglia-enriched proteomes do not show clear clustering between high and low extracellular fibrinogen deposition MS cases and controls.

A, PCA of normalised protein expression levels (3729 proteins) of microglial-enriched proteomes obtained from layer 5 of the motor cortex of high (F+, n = 19) and low (F-, n = 19) extracellular fibrinogen deposition MS cases and controls. **B-E**, The influence of CSF pH, Age at Death, Layer 5 fibrinogen extracellular score, and postmortem interval on PC1. CSF pH (B) was significantly negatively associated with PC1 (R^2 = 0.16, r = -0.32, p = 0.0306). **F-I**, The influence of CSF pH, Age at death, Layer 5 fibrinogen extracellular score, and postmortem interval on PC2. **J**, k-means clustering of PCA scatterplot with k = 3. Clusters did not differ in clinical or demographic variables as determined by one-way ANOVA, or their F+/F-/control proportions.

3.3.3 Differential protein expression between MS and control cases

MS cases (F+ and F- grouped) did not show significant differentially expressed when compared to controls (**Figure 3.3A**).

F+ cases and high extracellular fibrinogen control cases (defined as a control case with a layer 5 fibrinogen extracellular semiquantitative score ≥ the minimum in the F+ group)

did show a small number (14) of significantly differentially expressed proteins (**Figure 3.3B**). The following proteins were upregulated: EFTUD2, GATD1, MACR0D1, RARS1, and downregulated: CNDP1, GIPC1, GPR37L1, KYAT3, MIEN1, NKRF, PCBD1, SH3GLB1, SORBS2, TKT.

3.3.4 Differential protein expression between high and low extracellular fibrinogen MS cases

Despite tends towards differential protein expression between F+ and F- cases, no significant differences were seen (**Figure 3.3C**). Potential contributors to this include the cell-type enrichment within a cortical subregion of the input samples and the variability in fibrinogen deposition along layer 5, together resulting in unexpectedly smaller proteomic differences between groups than our study was powered to detect.

Following guidance from a domain-expert statistician, the comparison between F+ and F- was repeated following filtering for large log2 fold change differences (± 0.5). This significantly reduced the number of hypotheses to test and improved power to detect significant differences between the remaining proteins. This approach identified significantly differentially expressed proteins between F+ and F- cases, with 11 upregulated and 38 downregulated proteins recorded after BH correction at a permissive value of 0.1. (**Figure 3.3D**).

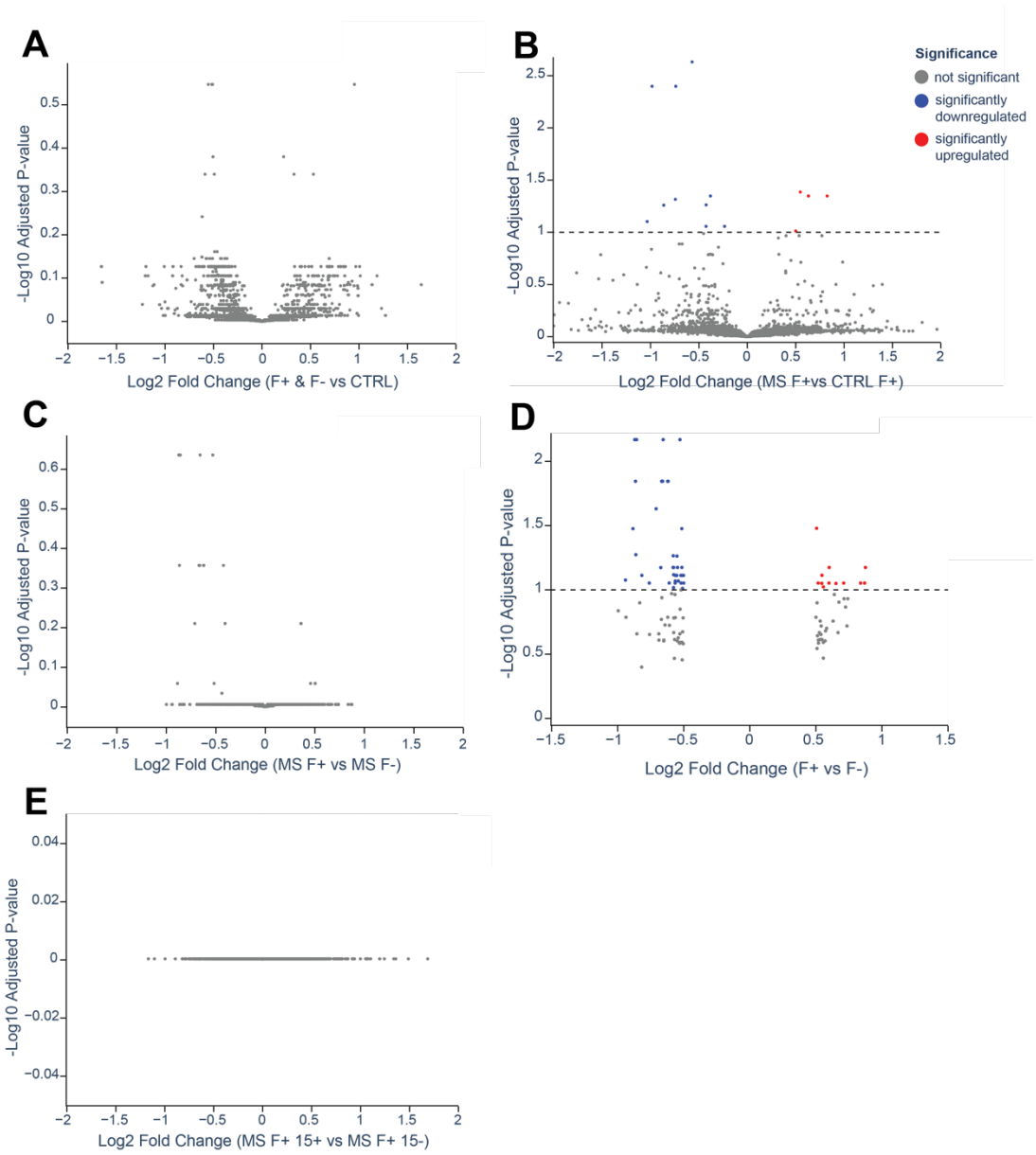

Figure 3.3. Differential expression analysis reveals subtle differences in protein expression between high and low extracellular fibrinogen deposition MS cases.

A, No significant differences were seen between all MS cases (n = 38) and controls (n = 7). **B**, 14 proteins were differentially expressed between F+ MS cases (n = 19) and high extracellular fibrinogen deposition controls (n = 3). **C**, No significant differences are seen in unfiltered differential expression analysis between F+ and F- (n = 19) MS cases. **D**, Differential expression analysis of proteins filtered by ± 0.5 log2 fold change identifies differences between F+ and F- MS cases, with 49 proteins differentially expressed. **E**, No significant differences were seen between HLA DRB1*1501+ (n = 10) and HLA DRB1*1501- (n = 9) F+ cases. Volcano plot blue dots indicate downregulation, red dots upregulation, and grey no difference. Differential expression calculated by two-way independent t test with BH multiple comparisons correction with FDR 0.1.

3.3.4.1 Analysis of significantly differentially expressed proteins between high and low extracellular fibrinogen MS cases

Given the tailored approach to differential expression analysis used in **3.3.4**, proteins identified as significantly differentially expressed were further investigated (**Figure 3.4A**).

The set of putative significantly differentially expressed proteins were assessed using two-way independent t-tests with a conventional BH-correction FDR of 0.05, and results plotted as box plots to provide insight into the data distribution within each group (**Figure 3.4B-F**). All proteins remained significantly differentially expressed between F+ and F- groups in this analysis. Across all proteins the average median difference in normalised expression level was 0.46.

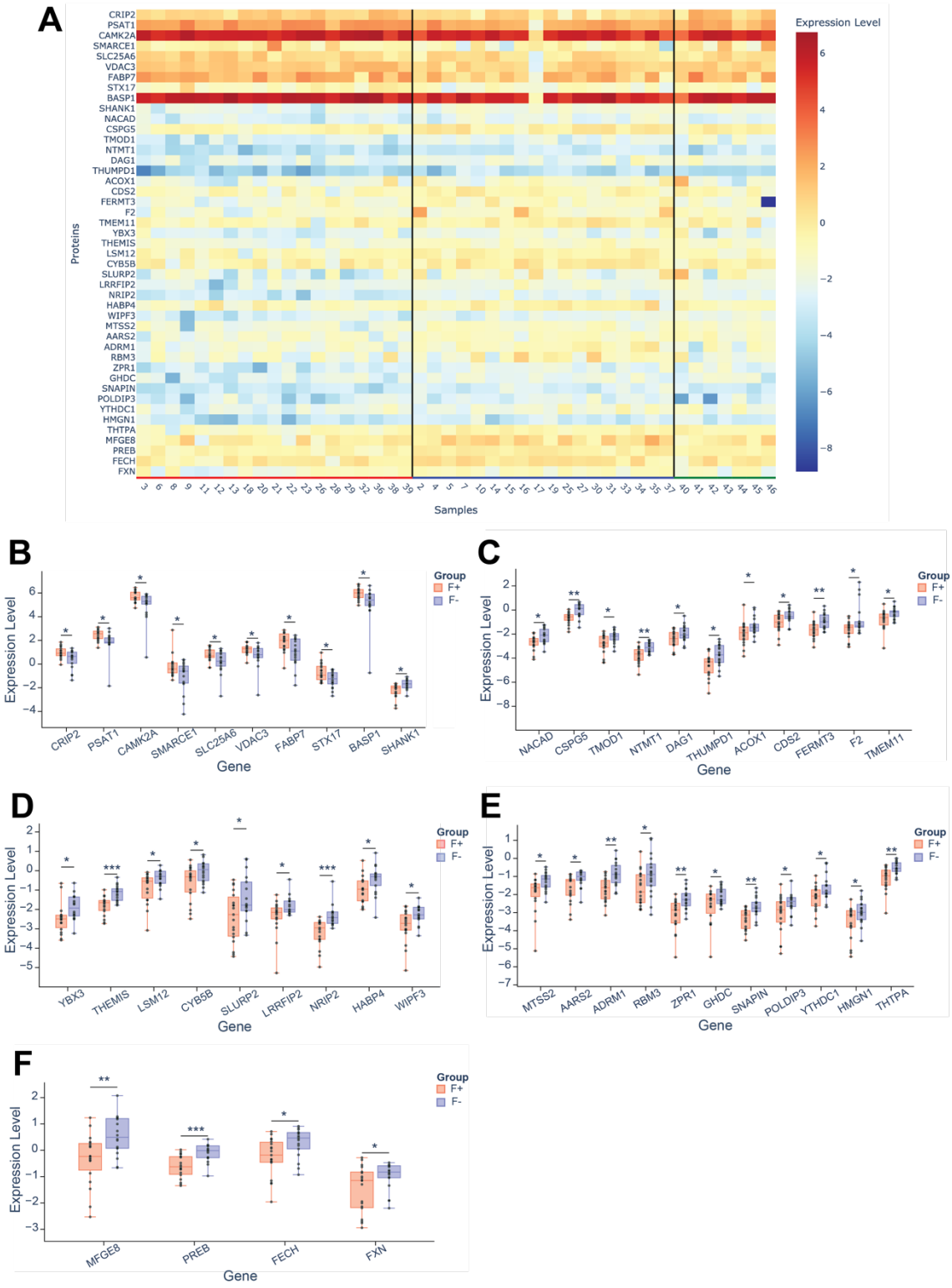

Figure 3.4. Significantly differentially expressed proteins between high and low extracellular fibrinogen deposition MS cases.

A, Heatmap of all normalised expression levels of differentially expressed proteins in F+ (bottom red bar) and F- (bottom blue bar), and control cases (green bar). **B-F**, Box plots showing normalised expression level of each protein in F+ and F- cases. Differences

assessed via two-way independent t test with BH correction at FDR 0.05. p □ 0.05 (*), p □ 0.01 (**), p < 0.001(***).

3.3.5 Pathway analysis of significantly differentially expressed genes between F+ and F- cases

The list of significantly differentially expressed proteins between the F+ and F- groups validated in **3.3.4.1**. was assessed for putative functional relevance via assessing the highest combined score terms for both up and down regulated proteins using the biological process, molecular function, and cellular component gene ontologies (**Figure 3.5A-F**).

Notable molecular function pathways among the up-regulated proteins were 'ADP transmembrane transporter activity', 'Calcium-dependent protein kinase activity', and 'Calcium-dependent protein serine/threonine kinase activity' (**Figure 3.5A**). Whilst amongst down-regulated proteins the terms 'Nitrite reductase activity', 'Ferric iron binding' and 'amino' (**Figure 3.5D**).

Cellular component pathways for up-regulated proteins included were 'Smooth endoplasmic reticulum membrane', 'Smooth endoplasmic reticulum' and 'Autophagosome membrane' (**Figure 3.5B**). For the down-regulated proteins 'Dystroglycan complex', 'Podosome', and 'Excitatory synapse' (**Figure 3.5E**).

Biological process pathways of note for upregulated proteins included 'Caveolin-mediated endocytosis' and 'Positive regulation of macrophage proliferation' (**Figure 3.5C**). 'Negative regulation of astrocyte differentiation' was a notable term in the downregulated proteins (**Figure 3.5F**).

3.3.6 STRING network analysis of significantly differentially expressed genes between F+ and F- cases

A protein interaction network was created between the significantly differentially expressed protein and selected proteins of relevance to the acute phase response (IL6R, PLAT), microglia/macrophage structure (TMEM119, AIF1, ITGAM), and fibrinogen binding (ITGB3, FGA, FGB, FGG, ITGA2B).

The resulting network (**Figure 3.5G**) was notable for most proteins lacking interactions between each other. The only interactions recorded between significant proteins were FECH-FXN, LSM12-ATXN, PEA15-MAPK1, and SLC25A6-VDAC3. Two interactions between significant proteins and selected proteins were identified, FERTM3-ITGB3, and F2-FGA/FGB/FGG.

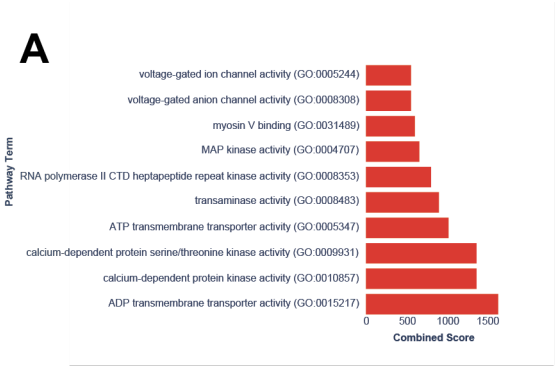
A
voltage-gated ion channel activity (GO:0005244)
voltage-gated anion channel activity (GO:0008308)
myosin V binding (GO:0031489)
MAP kinase activity (GO:0004707)
RNA polymerase II CTD heptapeptide repeat kinase activity (GO:0008353)
transaminase activity (GO:0008483)
ATP transmembrane transporter activity (GO:0005347)
calcium-dependent protein serine/threonine kinase activity (GO:0009931)
calcium-dependent protein kinase activity (GO:0010857)
ADP transmembrane transporter activity (GO:0015217)
Pathway Term
0 500 1000 1500
Combined Score

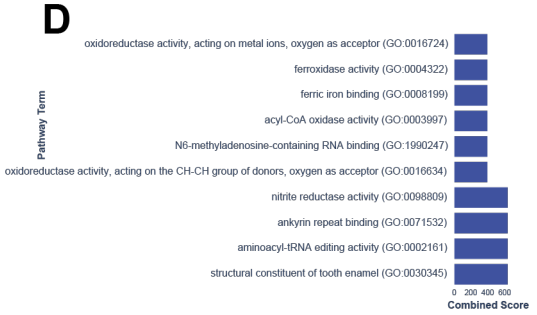
D
oxidoreductase activity, acting on metal ions, oxygen as acceptor (GO:0016724)
ferroxidase activity (GO:0004322)
ferric iron binding (GO:0008199)
acyl-CoA oxidase activity (GO:0003997)
N6-methyladenosine-containing RNA binding (GO:1990247)
oxidoreductase activity, acting on the CH-CH group of donors, oxygen as acceptor (GO:0016634)
nitrite reductase activity (GO:0098809)
ankyrin repeat binding (GO:0071532)
aminoacyl-tRNA editing activity (GO:0002161)
structural constituent of tooth enamel (GO:0030345)
Pathway Term
0 200 400 600
Combined Score

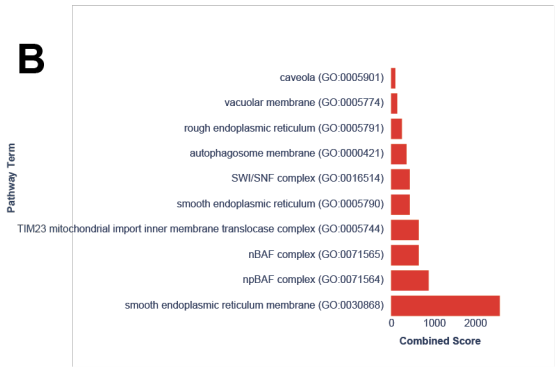
B
caveola (GO:0005901)
vacuolar membrane (GO:0005774)
rough endoplasmic reticulum (GO:0005791)
autophagosome membrane (GO:0000421)
SWI/SNF complex (GO:0016514)
smooth endoplasmic reticulum (GO:0005790)
TIM23 mitochondrial import inner membrane translocase complex (GO:0005744)
nBAF complex (GO:0071565)
npBAF complex (GO:0071564)
smooth endoplasmic reticulum membrane (GO:0030868)
Pathway Term
0 1000 2000
Combined Score

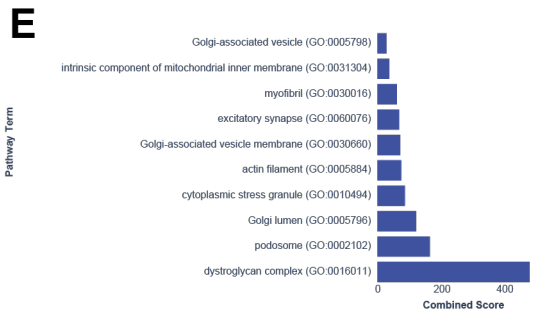
E
Golgi-associated vesicle (GO:0005798)
intrinsic component of mitochondrial inner membrane (GO:0031304)
myofibril (GO:0030016)
excitatory synapse (GO:0060076)
Golgi-associated vesicle membrane (GO:0030660)
actin filament (GO:0005884)
cytoplasmic stress granule (GO:0010494)
Golgi lumen (GO:0005796)
podosome (GO:0002102)
dystroglycan complex (GO:0016011)
Pathway Term
0 200 400
Combined Score

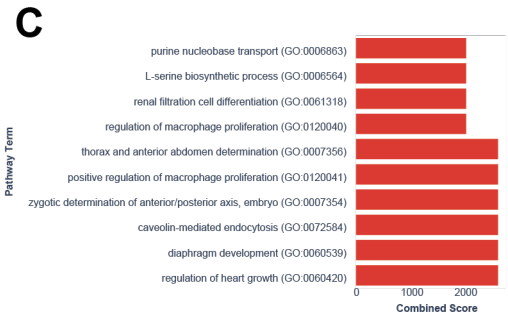
C
purine nucleobase transport (GO:0006863)
L-serine biosynthetic process (GO:0006564)
renal filtration cell differentiation (GO:0061318)
regulation of macrophage proliferation (GO:0120040)
thorax and anterior abdomen determination (GO:0007356)
positive regulation of macrophage proliferation (GO:0120041)
zygotic determination of anterior/posterior axis, embryo (GO:0007354)
caveolin-mediated endocytosis (GO:0072584)
diaphragm development (GO:0060539)
regulation of heart growth (GO:0060420)
Pathway Term
0 1000 2000
Combined Score

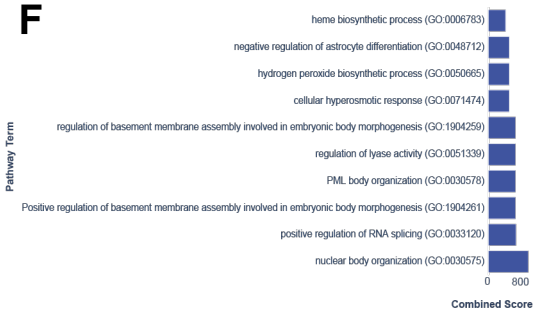
F
heme biosynthetic process (GO:0006783)
negative regulation of astrocyte differentiation (GO:0048712)
hydrogen peroxide biosynthetic process (GO:0050665)
cellular hyperosmotic response (GO:0071474)
regulation of basement membrane assembly involved in embryonic body morphogenesis (GO:1904259)
regulation of lyase activity (GO:0051339)
PML body organization (GO:0030578)
Positive regulation of basement membrane assembly involved in embryonic body morphogenesis (GO:1904261)
positive regulation of RNA splicing (GO:0033120)
nuclear body organization (GO:0030575)
Pathway Term
0 800
Combined Score

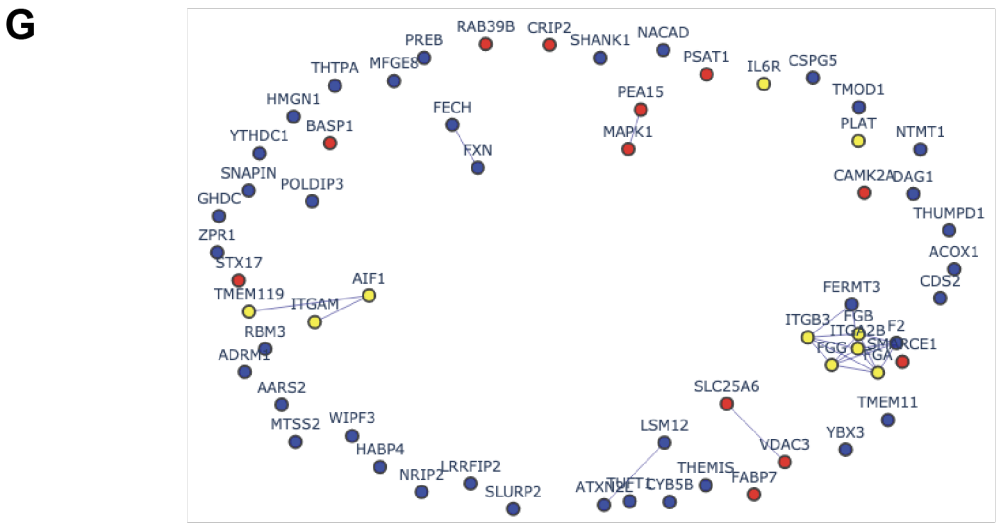
G
RAB39B
CRIP2
SHANK1
NACAD
PREB
PSAT1
IL6R
CSPG5
THTPA
MFGE8
TMOD1
PEA15
HMGN1
FECH
PLAT
NTMT1
BASP1
MAPK1
YTHDC1
FXN
CAMK2A
DAG1
SNAPIN
POLDIP3
THUMPD1
GHDC
ZPR1
ACOX1
STX17
AIF1
CDS2
FERMT3
TMEM119
ITGAM
ITGB3
F2
RBM3
ADRM1
SLC25A6
TMEM11
AARS2
LSM12
YBX3
MTSS2
WIPF3
VDAC3
HABP4
THEMIS
NRIP2
LRRFIP2
FABP7
SLURP2
CYB5B

Figure 3.5. Pathway analysis and protein-protein interactions of proteins significantly differentially expressed between high and low extracellular fibrinogen deposition MS cases.

A-C, Top 10 gene sets by combined score amongst upregulated proteins for biological process (A), cellular component (B), and molecular function (C) gene ontologies. **D-F**, Top 10 gene sets by combined score amongst downregulated proteins for biological process (D), cellular component (E), and molecular function (F) gene ontologies. **G**, STRING protein-protein interaction network of upregulated (red), downregulated (blue) and fibrinogen and microglia-relevant (yellow) proteins shows significant proteins to have limited protein-protein interactions.

3.3.7 Pathway analysis of significantly differentially expressed genes between high extracellular fibrinogen MS and control cases

The lower number of significantly differentially expressed proteins between high fibrinogen MS and control cases reduced the insights provided by pathway analysis (**Figure 3.6A-F**).

Spliceosome terms were frequent amongst the upregulated protein cellular component ontology (**Figure 3.6C**). Membrane-associated terms were frequent across the downregulated cellular component and biological function ontologies. 'Negative regulation of response to reactive oxygen species' was a particularly notable term in the set.

3.3.8 STRING network analysis of significantly differentially expressed genes between F+ and F- cases

All proteins in the protein interaction network of proteins significantly differentially expressed between high fibrinogen MS and control cases were isolated in the graph. No interactions with specified proteins of interest were seen (**Figure 3.6G**).

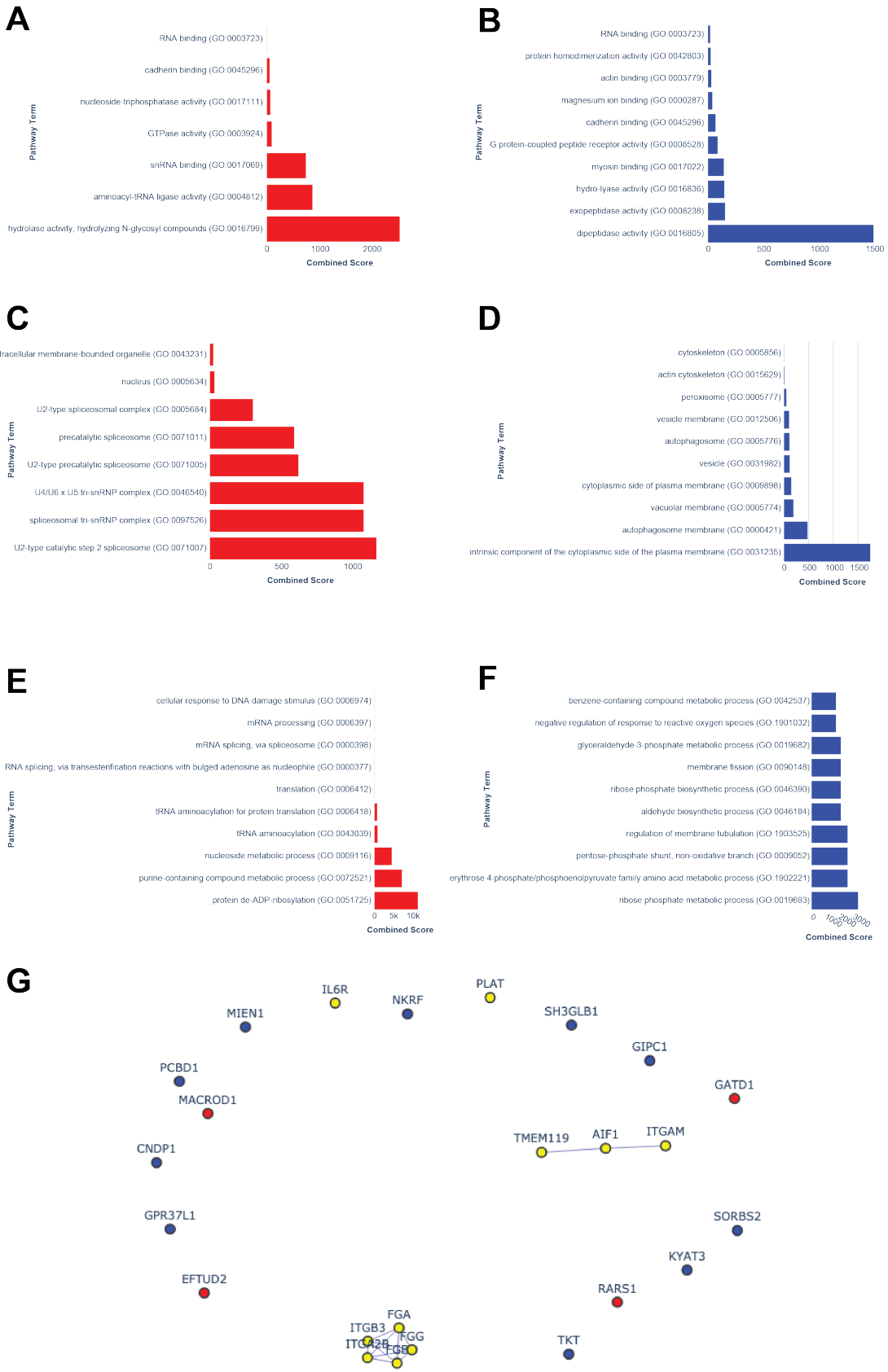
A
RNA binding (GO:0003723)
cadherin binding (GO:0045296)
nucleoside-triphosphatase activity (GO:0017111)
GTPase activity (GO:0003924)
snRNA binding (GO:0017069)
aminoacyl-tRNA ligase activity (GO:0004812)
hydrolase activity, hydrolyzing N-glycosyl compounds (GO:0016799)
Pathway Term
0
1000
2000
Combined Score
B
RNA binding (GO:0003723)
protein homodimerization activity (GO:0042803)
actin binding (GO:0003779)
magnesium ion binding (GO:0000287)
cadherin binding (GO:0045296)
G protein-coupled peptide receptor activity (GO:0008528)
myosin binding (GO:0017022)
hydro-lyase activity (GO:0016836)
exopeptidase activity (GO:0008238)
dipeptidase activity (GO:0016805)
Pathway Term
0
500
1000
1500
Combined Score
C
intracellular membrane-bounded organelle (GO:0043231)
nucleus (GO:0005634)
U2-type spliceosomal complex (GO:0005684)
precatalytic spliceosome (GO:0071011)
U2-type precatalytic spliceosome (GO:0071005)
U4/U6 x U5 tri-snRNP complex (GO:0046540)
spliceosomal tri-snRNP complex (GO:0097526)
U2-type catalytic step 2 spliceosome (GO:0071007)
Pathway Term
0
500
1000
Combined Score
D
cytoskeleton (GO:0005856)
actin cytoskeleton (GO:0015629)
peroxisome (GO:0005777)
vesicle membrane (GO:0012506)
autophagosome (GO:0005776)
vesicle (GO:0031982)
cytoplasmic side of plasma membrane (GO:0009898)
vacuolar membrane (GO:0005774)
autophagosome membrane (GO:0000421)
intrinsic component of the cytoplasmic side of the plasma membrane (GO:0031235)
Pathway Term
0
500
1000
1500
Combined Score
E
cellular response to DNA damage stimulus (GO:0006974)
mRNA processing (GO:0006397)
mRNA splicing, via spliceosome (GO:0000398)
RNA splicing, via transesterification reactions with bulged adenosine as nucleophile (GO:0000377)
translation (GO:0006412)
tRNA aminoacylation for protein translation (GO:0006418)
tRNA aminoacylation (GO:0043039)
nucleoside metabolic process (GO:0009116)
purine-containing compound metabolic process (GO:0072521)
protein de-ADP-ribosylation (GO:0051725)
Pathway Term
0
5k
10k
Combined Score
F
benzene-containing compound metabolic process (GO:0042537)
negative regulation of response to reactive oxygen species (GO:1901032)
glyceraldehyde-3-phosphate metabolic process (GO:0019682)
membrane fission (GO:0090148)
ribose phosphate biosynthetic process (GO:0046390)
aldehyde biosynthetic process (GO:0046184)
regulation of membrane tubulation (GO:1903525)
pentose-phosphate shunt, non-oxidative branch (GO:0009052)
erythrose 4-phosphate/phosphoenolpyruvate family amino acid metabolic process (GO:1902221)
ribose phosphate metabolic process (GO:0019693)
Pathway Term
0
1000
2000
3000
Combined Score
G
IL6R
NKRF
MIEN1
PCBD1
MACROD1
CNDP1
GPR37L1
EFTUD2
FGA
ITGB3
FGG
FGB
PLAT
SH3GLB1
GIPC1
GATD1
TMEM119
AIF1
ITGAM
SORBS2
KYAT3
RARS1
TKT

Figure 3.6. Pathway analysis and protein-protein interactions of proteins significantly differentially expressed between high extracellular fibrinogen deposition MS and control cases.

A-C, Top 10 gene sets by combined score amongst upregulated proteins for biological process (A), cellular component (B), and molecular function (C) gene ontologies. **D-F**, Top 10 gene sets by combined score amongst downregulated proteins for biological process (D), cellular component (E), and molecular function (F) gene ontologies. **G**, STRING protein-protein interaction network of upregulated (red), downregulated (blue) and fibrinogen and microglia-relevant (yellow) proteins shows significant proteins to have no protein-protein interactions with each other or fibrinogen or microglial-relevant proteins.

3.3.9 Gene set enrichment analysis between high and low extracellular fibrinogen MS cases

Given the low number of proteins identified as significantly different between the F+ and F- groups, GSEA was performed to leverage the collective effects of proteins within gene sets to better understand the likely functional differences between microglia in the F+ and F- groups, aiding in hypothesis generation. All gene sets within the biological process, molecular function, and cellular component gene ontologies were used.

Enriched gene sets in the biological process ontology showed particularly high NES for metabolism-related processes, particularly related to glycolysis with 9/11 terms with NES scores >2.0 metabolism-related. Other terms of particular interest include ‘Regulation of neuronal synaptic plasticity’, ‘Cellular response to oxidative stress’, ‘regulation of cellular response to heat’, ‘Cellular response to chemical stress’, Cellular response to amino acid starvation’ (**Figure 3.7A**). 10 Biological process gene sets were negatively enriched (**Figure 3.7D**), including innate immune related terms ‘Defence response to symbiont’ and ‘Defence response to virus’, and a variety of mitochondrial translation-related terms.

15 cellular component gene sets were significantly positively enriched (**Figure 3.7C**). Metabolism-related terms were again prevalent amongst these sets, with a notable number of lysosomal/vesicular terms such as ‘Lysosomal membrane’, and ‘Endocytic vesicle membrane’ amongst the remaining terms. No cellular component gene sets were negatively enriched.

7 Molecular function gene sets were significantly increased in the F+ group, of which 5 were related to oxidative phosphorylation (**Figure 3.7B**). 7 Molecular function gene sets were negatively enriched (**Figure 3.7E**), ‘Receptor ligand activity’ was the most significant and negatively enriched term, with 5 of the remaining terms peptidase related.

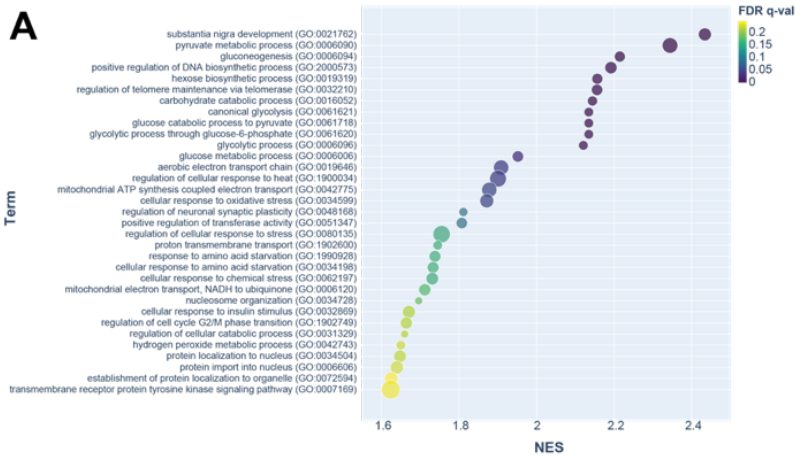
A
substantia nigra development (GO:0021762)
pyruvate metabolic process (GO:0006090)
gluconeogenesis (GO:0006094)
positive regulation of DNA biosynthetic process (GO:2000573)
hexose biosynthetic process (GO:0019319)
regulation of telomere maintenance via telomerase (GO:0032210)
carbohydrate catabolic process (GO:0016052)
canonical glycolysis (GO:0061621)
glucose catabolic process to pyruvate (GO:0061718)
glycolytic process through glucose-6-phosphate (GO:0061620)
glycolytic process (GO:0006096)
glucose metabolic process (GO:0006006)
aerobic electron transport chain (GO:0019646)
regulation of cellular response to heat (GO:1900034)
mitochondrial ATP synthesis coupled electron transport (GO:0042775)
cellular response to oxidative stress (GO:0034599)
regulation of neuronal synaptic plasticity (GO:0048168)
positive regulation of transferase activity (GO:0051347)
regulation of cellular response to stress (GO:0080135)
proton transmembrane transport (GO:1902600)
response to amino acid starvation (GO:1990928)
cellular response to amino acid starvation (GO:0034198)
cellular response to chemical stress (GO:0062197)
mitochondrial electron transport, NADH to ubiquinone (GO:0006120)
nucleosome organization (GO:0034728)
cellular response to insulin stimulus (GO:0032869)
regulation of cell cycle G2/M phase transition (GO:1902749)
regulation of cellular catabolic process (GO:0031329)
hydrogen peroxide metabolic process (GO:0042743)
protein localization to nucleus (GO:0034504)
protein import into nucleus (GO:0006606)
establishment of protein localization to organelle (GO:0072594)
transmembrane receptor protein tyrosine kinase signaling pathway (GO:0007169)
Term
1.6
1.8
2
2.2
2.4
NES
FDR q-val
0.2
0.15
0.1
0.05
0


B
hydro-lyase activity (GO:0016836)
oxidoreductase activity, acting on the CH-OH group of donors, NAD or NADP as acceptor (GO:0016616)
oxidoreduction-driven active transmembrane transporter activity (GO:0015453)
NAD binding (GO:0051287)
NADH dehydrogenase (quinone) activity (GO:0050136)
NADH dehydrogenase (ubiquinone) activity (GO:0008137)
calcium ion transmembrane transporter activity (GO:0015085)
Term
1.7
1.8
1.9
NES
FDR q-val
0.2
0.15
0.1
0.05

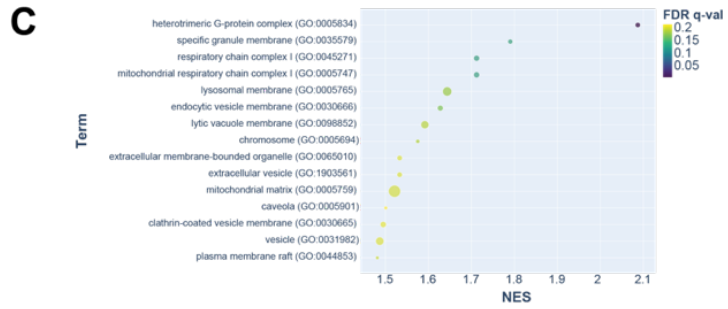
C
heterotrimeric G-protein complex (GO:0005834)
specific granule membrane (GO:0035579)
respiratory chain complex I (GO:0045271)
mitochondrial respiratory chain complex I (GO:0005747)
lysosomal membrane (GO:0005765)
endocytic vesicle membrane (GO:0030666)
lytic vacuole membrane (GO:0098852)
chromosome (GO:0005694)
extracellular membrane-bounded organelle (GO:0065010)
extracellular vesicle (GO:1903561)
mitochondrial matrix (GO:0005759)
caveola (GO:0005901)
clathrin-coated vesicle membrane (GO:0030665)
vesicle (GO:0031982)
plasma membrane raft (GO:0044853)
Term
1.5
1.6
1.7
1.8
1.9
2
2.1
NES
FDR q-val
0.2
0.15
0.1
0.05

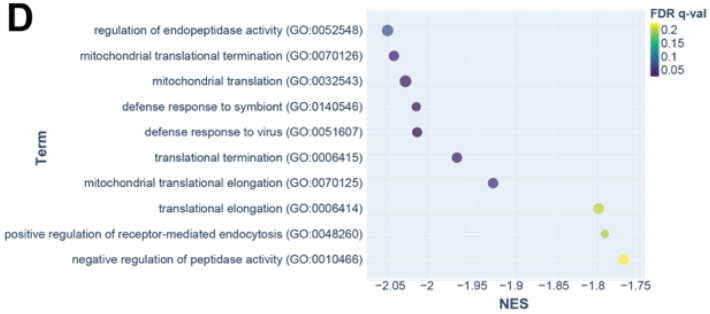
D
regulation of endopeptidase activity (GO:0052548)
mitochondrial translational termination (GO:0070126)
mitochondrial translation (GO:0032543)
defense response to symbiont (GO:0140546)
defense response to virus (GO:0051607)
translational termination (GO:0006415)
mitochondrial translational elongation (GO:0070125)
translational elongation (GO:0006414)
positive regulation of receptor-mediated endocytosis (GO:0048260)
negative regulation of peptidase activity (GO:0010466)
Term
−2.05
−2
−1.95
−1.9
−1.85
−1.8
−1.75
NES
FDR q-val
0.2
0.15
0.1
0.05

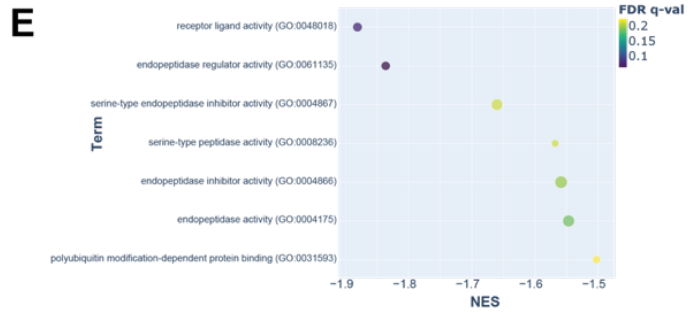
E
receptor ligand activity (GO:0048018)
endopeptidase regulator activity (GO:0061135)
serine-type endopeptidase inhibitor activity (GO:0004867)
serine-type peptidase activity (GO:0008236)
endopeptidase inhibitor activity (GO:0004866)
endopeptidase activity (GO:0004175)
polyubiquitin modification-dependent protein binding (GO:0031593)
Term
−1.9
−1.8
−1.7
−1.6
−1.5
NES
FDR q-val
0.2
0.15
0.1

Figure 3.7. Gene set enrichment analysis of suggests microglia from layer 5 of the motor cortex undergo a pro-glycolytic metabolic shift in high extracellular fibrinogen conditions.

A-C, significantly positively enriched gene sets in the F+ group from the biological process (A), molecular function (B) and cellular component (C) gene ontologies show a high proportion of metabolism-related terms alongside vesicle-regulatio terms. **D,E**, Significantly negatively enriched gene sets in the F+ group for the biological process (D) and molecular function (E) gene ontologies highlight receptor-ligand binding, endopeptidase activity and innate immune response as downregulated processes under high extracellular fibrinogen conditions. Dot size indicates percentage of gen set present in proteomic data.

3.3.10 Targeted differential expression analysis of synapse-related proteins

Building on the insights gained throughout this chapter, and considering fibrinogens established effects in the brain[233], a panel of synapse-related proteins were investigated (**Figure 3.8A**).

Expression levels of the inhibitory synapse proteins GAD1 (p = 0.034) and GABRB2 (p = 0.016) were significantly lower in F+ cases. The median expression value of all other proteins making up the $GABA_A$, bar GABRB1, were lower in the F+ group but did not reach significance (**figure 3.8B**). Other $GABA_A$ subunit proteins were not present in the dataset.

No significant differences in expression were seen between F+ and F- groups with regards to glutamate receptor components (**Figure 3.8C**).

Among general synapse markers (**Figure 3.*8D***), only SHANK1 was significantly reduced in the F+ group (p = 0.031).

CSPG5 (n = 0.008), was significantly reduced in F+ cases among the proteoglycans (**Figure 3.8E**).

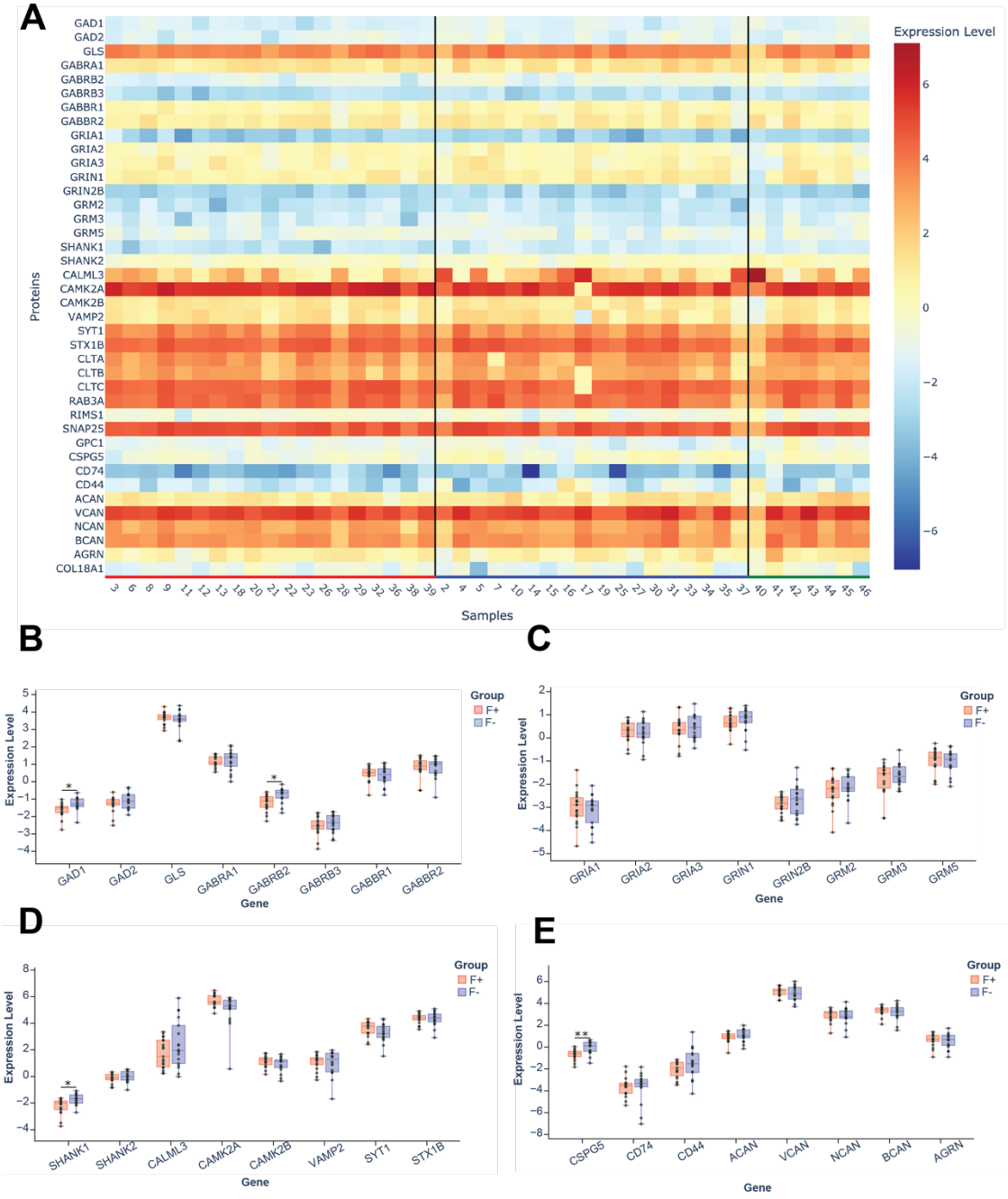

Figure 3.8. Inhibitory synapse-related proteins show lower expression in high compared to low extracellular fibrinogen MS cases.

A, heatmap of normalised expression levels for curated synapse-relevant proteins present in proteomic dataset in F+ (bottom red bar) and F- (bottom blue bar) MS cases, and controls. **B-E**, Normalised expression levels of selected synapse-related proteins in the F+ and F- MS groups. B, Inhibitory-synapse related proteins show a general reduction in $GABA_A$ components with GABRB2 reaching significance ($p = 0.016$) in the F+ group., GAD1 ($p = 0.034$) but not GAD 2. C, no significant differences are seen for excitatory synapse-related proteins. D, Amongst general synapse-related proteins, Shank1 ($p = 0.031$) shows lower expression in the F+ group. E, CSPG5 ($p = 0.008$) is the only proteoglycan to show altered

expression levels between the F= and F- MS groups. Differences assessed via two-way independent t test with BH correction at FDR 0.05. $p \leq 0.05$ (*), $p \leq 0.01$ (**), $p < 0.001$(***).

3.3.11 Putative functional overlap between microglia from high fibrinogen cases and a separate dataset of subtype-specific astrocyte proteomes

To determine if the microglial response to high extracellular fibrinogen might interact with unique astrocyte subtypes, the network of significantly differentially expressed proteins and first neighbours created in **3.3.5** was integrated with a list of proteins uniquely upregulated by each of the astrocyte subtypes GFAP+, ALDH1L1+, GFAP+/ALDH1L1+ (**Figure 3.9A-C**). 288 GFAP+, 316 ALDH1L1+, and 18 GFAP+/ALDH1L1+ uniquely upregulated proteins were identified. Where this list included first neighbours of the microglial proteins, a potential interaction was recorded, giving 16 GFAP+-microglia, and 34 ALDH1L1+-microglia pairs of protein-protein interaction (**Figure 3.9D**).

The astrocyte partners in each protein-protein interaction pair were assessed for functional relevance via the biological functions gene ontology, and the top 20 terms by combined score plotted as an interaction network for each astrocyte subtype (**Figure 3.9E, G**). Nodes in this interaction network were coloured by the fold change seen in the microglial partner for the F+ vs F- differential expression analysis performed in **3.3.4.1**.

The ALDH1L1+ interaction network (**Figure 3.9E, F**) included only terms related to translation/transcription and protein modification, likely representing protein-protein interactions between the datasets that occurred by chance.

In contrast, the GFAP+ interaction network (**Figure 3.9G, H**), included a variety of terms that likely represent functional overlap between GFAP+ astrocytes and microglia in high extracellular fibrinogen contexts. Notable terms included ‘Positive regulation of synapse structure’, ‘Positive regulation of synapse assembly’, ‘Positive regulation of synapse maturation’, and ‘Maintenance of blood-brain barrier’.

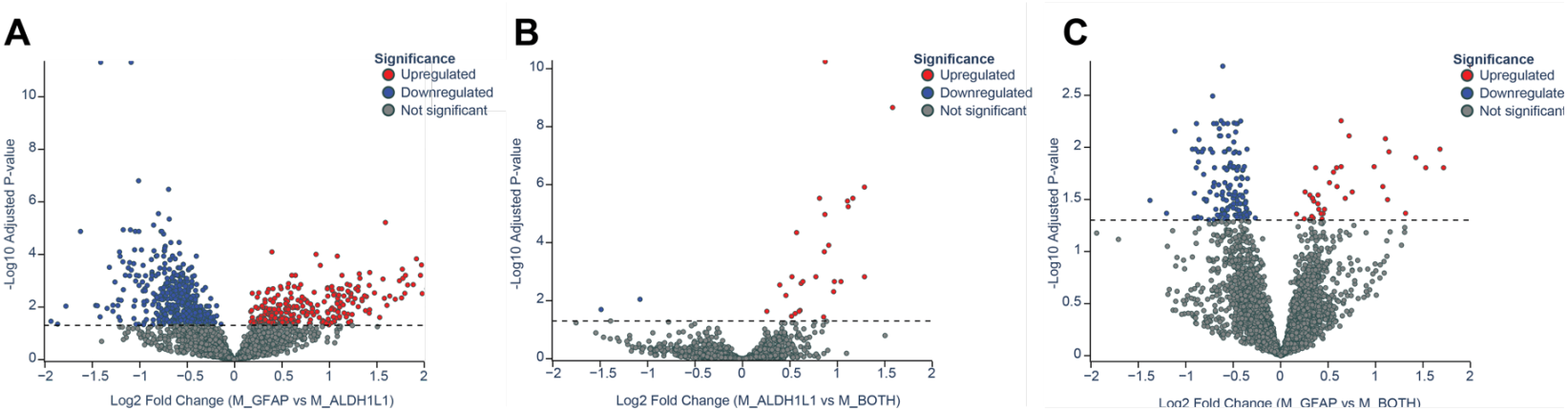

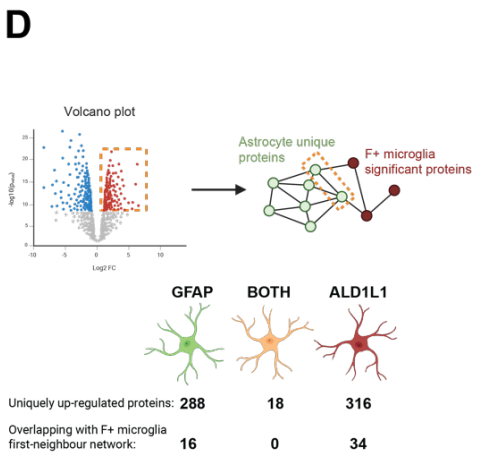

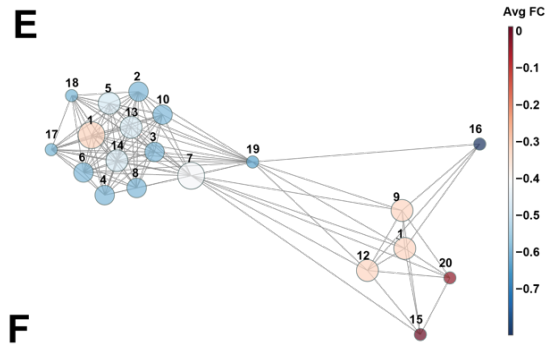

F

Number	GO Term	Gene Count
1	translation	11
2	SRP-dependent cotranslational protein targeting to membrane	8
3	cytoplasmic translation	8
4	cotranslational protein targeting to membrane	8
5	peptide biosynthetic process	9
6	protein targeting to ER	8
7	gene expression	11
8	nuclear-transcribed mRNA catabolic process, nonsense-mediated decay	8
9	RNA splicing, via transesterification reactions with bulged adenosine as nucleophile	9
10	nuclear-transcribed mRNA catabolic process	8
11	mRNA splicing, via spliceosome	9
12	mRNA processing	9
13	cellular macromolecule biosynthetic process	9
14	cellular protein metabolic process	9
15	RNA splicing	5
16	regulation of mRNA stability	5
17	rRNA metabolic process	5
18	rRNA processing	5
19	regulation of translation	5
20	RNA processing	5

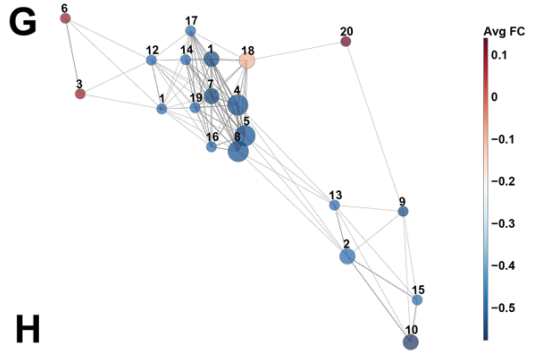

H

Number	GO Term	Gene Count
1	glycosaminoglycan catabolic process	3
2	muscle organ development	3
3	positive regulation of synapse maturation	2
4	extracellular structure organization	4
5	external encapsulating structure organization	4
6	regulation of synapse maturation	2
7	glycosaminoglycan biosynthetic process	3
8	extracellular matrix organization	4
9	negative regulation of peptidyl-serine phosphorylation	2
10	muscle contraction	3
11	receptor clustering	2
12	positive regulation of synapse assembly	2
13	maintenance of blood-brain barrier	2
14	aminoglycan catabolic process	2
15	regulation of sodium ion transmembrane transporter activity	2
16	aminoglycan biosynthetic process	2
17	glycosaminoglycan metabolic process	2
18	central nervous system development	3
19	diterpenoid metabolic process	2
20	positive regulation of cytoskeleton organization	2

Figure 3.9. Proteins showing increased expression uniquely in ALDH1L1+, GFAP+, and ALDH1L1+/GFAP+ astrocytes show distinct functional overlap with proteins significantly differentially expressed in microglia from high extracellular fibrinogen environments.

A-C, Differential expression of proteins between ALDH1L1+ and GFAP+ (A), ALDH1L1 and ALDH1L1+/GFAP+ (B), and GFAP+ and ALDH1L1+/GFAP+ (C) astrocytes. **D**, To assess pathway interaction between astrocyte subtypes and microglia from high extracellular fibrinogen deposition MS cases the proteins uniquely upregulated in each astrocyte subtype are cross referenced with the a list of proteins with direct interactions with proteins significantly differentially expressed by microglia. Astrocyte proteins that match this list are used for pathway analysis of the top 20 biological process gene ontology terms. **F**, ALDH1L1+ astrocytes show interaction with ribosomal and translational terms. **G**, GFAP+ astrocytes show interaction with synapse-related, receptor clustering, extracellular structure terms. Interaction network nodes are coloured by log2 fold change of the microglial partner in astrocyte-protein network matches, node size represents number of genes in the pathway present. Differential expression calculated by two-way independent t test with BH multiple comparisons correction with FDR 0.05.

3.4 Discussion

An understanding of the microglial response to fibrinogen in the context of the human brain is essential to determining why fibrinogen negatively associates with neuronal density in MS (**Table 2.4**)[191]. This chapter demonstrates that while overall differences between microglial proteomes of cases with high and low extracellular fibrinogen within layer 5 of the motor cortex are subtle, alterations in microglial interactions with inhibitory synapses, and changes in microglial metabolism, are intricately linked to this response. The proteins identified here provide crucial insight into the *in situ* structural changes that ultimately contribute to neurodegeneration in MS and serve as an invaluable dataset for hypothesis generation.

The subtle differences seen between F+, F-, and control proteomes in this study (**Figure 3.2**) are likely a function of the highly variable deposition of fibrinogen, which we earlier demonstrated to show significant spatial transitions in layer 5 of the motor cortex (**Figure 3.7**). Even within a targeted region of an individual case, levels of fibrinogen extravasation can vary significantly between vessel that are in close proximity. This suggests that at a fixed timepoint BBB integrity can vary locally. Indeed, in a study of 201 individuals with WMH where BBB integrity was measured at the millimetre scale, the NAWM showed a gradient of BBB leakage that increased with proximity to the WMH edge[241]. The causes of local-scale BBB integrity changes have been little explored, but mechanical[212], pressure-related[242], and inflammatory processes[243,244] all influence BBB integrity[232,245] and may contribute.

While mechanistic studies using direct fibrinogen injections provide valuable insights, they may not fully capture the nuanced dynamics of fibrinogen extravasation in the MS brain. This discrepancy could also contribute towards the smaller than expected effects seen in this study. Mechanistic studies of fibrinogen's effects in the brain have used levels of fibrinogen within the physiological range of ~1.5-4 g/L[246], which is directly injected into the site of interest[198,202,247]. This may not accurately reflect local fibrinogen levels following BBB integrity reductions and fibrinogen extravasation in the brain. Impaired BBB integrity does not constitute an absence of BBB integrity; correspondingly, only a proportion of fibrinogen from the plasma may extravasate at a given time, with diffusion into the larger extracellular space of the parenchyma, and uptake by CNS cells[211], decreasing deposition rate as distance from the vessel increases. Consequently, *in situ* in the MS motor cortex, the effects of fibrinogen are likely lower than in model systems.

The proteins identified as differentially expressed between the F+ and F- groups (**Figure 3.4A**) provide an intriguing insight into the microglial response to fibrinogen. These include proteins with known relevance to fibrinogen such as thrombin (F2), as well as proteins with well-established roles in synaptic remodelling (MFGE8), microglia/macrophage motility and structure (FERMT3, kindlin3), and microglia/macrophage metabolism (FXN, frataxin), that have not previously been linked to the microglial response to fibrinogen.

Thrombin not only regulates the conversion of fibrinogen to fibrin; the concentration of thrombin also influences the physical properties of resulting fibrin aggregates. Thrombin concentration is inversely correlated with the thickness of individual fibrin fibres, with thicker fibres more likely to elongate than thinner fibres, whilst thinner fibres

lyse more readily[248]. Fibrin clots composed of thicker fibrin fibres are more permeable and susceptible to fibrinolysis which may prolong bleeding[77]. Local mechanical factors, notably flow rate, further contribute to clot characteristics, with clots forming under low-flow conditions having larger pores and larger fibres, and reduced stiffness[249]. Thrombin may also be incorporated in its active form into fibrin clots, providing a mechanism for the removal of thrombin from the local environment by fibrin[250]. Given this complex set of possibilities, the interpretation of lower thrombin levels in the F+ group (**Figure 3.4C**) requires careful future investigation.

MFGE8 has recently emerged as a protein of interest in the phagocytosis of synapses, but this has not yet been reported in MS. In primary human astrocyte and microglial cultures AD synapses are phagocytosed, with this effect attenuated by blocking MFGE8[251]. A current preprint builds on this relationship in the NL-F mouse model of AD, showing astrocytes to be the primary expressor of MFGE8, with astrocyte-derived MFGE8 being required for microglial phagocytosis of excitatory synapses[252]. However, a separate study of AD using APP mice and a large human RNAseq dataset suggested MFGE8's role in AD is primarily via enhancing Aβ aggregation[253]. Outside of AD, MFGE8 has been demonstrated to have beneficial anti-inflammatory effects in murine models of ischemia-reperfusion in cutaneous ulcers[254] and the liver, where the number of apoptotic cells was reduced on recombinant MFGE8 administration[255]. In postischemic cerebral ischemic injury in mice, MFGE8 was shown to act downstream of ATP released by necrotic cells, with MFGE8 supplementation lessening IL-1β production and infarct size[256]. The static snapshot provided postmortem in our study therefore makes interpretation of MFGE8's role tricky but positions it firmly as a protein of interest.

Kindlin3 acts as an intracellular adapter for integrin binding[257,258] and plays a crucial role in leukocyte adhesion[257,259]. Microglial kindlin3 is required for mechanosensory sensing of tissue stiffness, which in the retina allows microglia to polarise and support normal vascular development[260]. This capacity to sense tissue stiffness triggers the upregulation of proinflammatory genes, morphological spreading, and migration towards stiff surfaces (durotaxis)[261,262]. In the 5xFAD mouse model of AD, the microglial mechanosensory capacity for stiffness, via Piezo1, enables microglial to locate Aβ fibrils via their mechanical properties and facilitates subsequent clearance[263]. Given the structural properties of fibrin aggregates, it is feasible microglia in a high fibrin aggregate environment might alter their interactions with surrounding surfaces. Notably, kindlin3's interactions with integrins[257,264] allows an indirect interaction with fibrinogen[265] (**Figure 3.5G**). In human atherosclerotic plaques, kindlin3 shows increased expression in monocytes associated with an anti-inflammatory phenotype, especially in unstable plaques[266]. Atherosclerotic plaques prone to instability have higher fibrin content than more stable plaques[267]. This suggests that in the context of atherosclerosis, kindin3 might influence monocyte-derived macrophage responses to fibrous structures via mechanosensory signalling. Our proteomic data (**Figure 3.4D**) shows kindlin3 to have significantly lower expression in the F+ group, suggesting significant alterations in the microglial-surface interaction.

GSEA of proteins in the F+ group compared to the F- group suggested a shift towards glycolytic metabolism in layer 5 microglia under high extracellular fibrinogen conditions (**Figure 3.7A**). In conjunction with the significantly lower expression of frataxin (**Figure 3.4F**), a protein interacting with respiratory complexes I, II, and III, deficiency in which causes the rare inheritable neurodegenerative disorder Friedreich's ataxia[268], this strongly suggests a metabolic shift in microglia. Frataxin deficiency directly increases

ROS production within mitochondria[269], providing a further link to mechanistic studies of fibrinogen and microglia. Very recently frataxin deficiency has been demonstrated to cause a proinflammatory and highly glycolytic phenotype amongst microglia derived from the cerebellum of a mouse model of Friedreich's ataxia[270], providing a putative mechanism for the metabolic shift suggested by our data.

GAD1 and GABRB2, both markers of inhibitory synaptic function, were significantly decreased in the F+ group compared to the F- group (**Figure 3.8B**). Whilst GABRB2 was the only protein to reach significance in our comparison, all other $GABA_A$ subunits of the predominant $GABA_A$ subtype ($\alpha_1\beta_2\gamma_2$)[271] showed lower median values in the F+ group. No such differences were apparent for the $GABA_B$ subunits GABBR1 and GABBR2. Given the differing roles of $GABA_A$ and $GABA_B$ in inhibitory synaptic transmission[272,273], as well as the differing properties of $GABA_A$ subtypes[274], it requires validation if the GABRB2 reduction is a specific loss of this β-subunit isoform, or merely the only protein to reach significance in a general reduction of $GABA_A$.

GAD1 (Gad67) represents the major source of GABA in the mammalian brain[275], where it is constituently active within the soma and has the capacity to localise to the pre-synapse[276]. In contrast, GAD2 represents a much smaller amount of GABA production and is localised pre-synoptically[277,278]. The reduction we see in GAD1, but not GAD2, in the F+ group (**Figure 3.8B**) therefore hints at a loss of GABA-containing cells in addition to a loss of GABA synapses.

Shank1 is a member of the Shank family of scaffolding proteins located at excitatory pre-synapses, which have been extensively investigated in autism spectrum disorders[279]. Shank1 has also been demonstrated to be highly expressed by

parvalbumin inhibitory interneurons of the mouse hippocampus, with loss of shank1 in these neurons reducing the excitatory inputs they can receive, and consequently their inhibitory output to pyramidal cells is reduced[280]. Parvalbumin expression was lower in the F+ group compared to F- (**Figure 3.8D**), however, this did not reach significance.

Overall, our data is supportive of mechanistic studies showing ROS production and synapse loss in response to fibrinogen extravasation into the brain parenchyma but suggests strength of this response may be locally variable. We add crucial detail to how this might occur *in situ*, identifying components related to mitochondrial dysfunction and increased glycolysis, and the response to altered tissue structure as relevant. We also present data suggesting that inhibitory synapses are preferentially affected by this in the MS motor cortex. Together this represents a rich dataset that will allow future work to further elucidate the microglial response to extracellular fibrinogen deposition.

Chapter 4 | Morphological and spatial analysis of novel proteomic hits and inhibitory synapses in the multiple sclerosis motor cortex

4.1 Introduction

This thesis has so far explored the heterogeneity of fibrinogen deposition and its relationship to neurons in MS and identified novel proteins from the local microglia environment of high and low extracellular fibrinogen deposition MS cases. This data strongly suggested a negative association between extracellular fibrinogen and neuronal density, with this predominantly affecting small and intermediate sized neurons. Our proteomic data built on this observation by suggesting a shift in microglial state, and a negative association with inhibitory synapses. These results did not however locally-resolve these associations, preventing their confirmation.

To determine if fibrinogen is locally associated with altered neuronal and microglial properties, I combined features of the image analysis pipelines developed in chapter 2. with the insights provided by the microglial-enriched proteomic data. This facilitated the validation and morphological quantification of novel proteomic hits, as well as the local quantification of fibrinogen's effects on neuronal density and inhibitory synaptic coverage across thousands of individual cells. Even within a small number of cases this provided an extremely rich dataset in which to determine if fibrinogen's effects at the local level drives the relationships we have previously observed.

4.2 Methods

4.2.1 Study population

A sub-cohort (n = 8) of the human autopsy cohort of pathologically confirmed MS cases (n = 40) obtained from the Multiple Sclerosis and Parkinson's Tissue Bank at Imperial College, London, and previously used in our proteomic analyses, was used. Appropriate ethical approval was obtained (REC 08/MRE09/31+5) and all tissue was used in strict compliance with the conditions of the UK Human Tissue Act (2004).

Cases within this sub-cohort were matched for demographic and clinical variables, as well as HLA DRB1*1501 status. MS cases were grouped as F+ or F- as determined by extracellular fibrinogen deposition semi-quantitative score in layer 5. Details of this cohort are shown in **Table 4.1**.

4.2.2 Immunohistochemistry/immunofluorescence

Immunohistochemistry for fibrinogen was performed as described in **2.2.2**.

Immunofluorescent staining was performed using 4μm-thick FFPE sections of the motor cortex were cut using a microtome prior to air-drying and storage. During the staining protocol sections were quenched using TrueBlack lipofuscin autofluorescence quencher (Biotium) and treated with serum-free protein block (Agilent). Sections were multi-labelled for DAPI, NeuN, Iba1 and GAD65/67.

WSIs at 40X magnification were obtained for each section at the Oxford Translational Histopathology Lab using an Akoya Biosciences Vector Polaris slide scanner (Akoya biosciences).

Table 4.1. Staining antibodies

Antigen	Host species	Antigen-retrieval	Dilution	Supplier	Catalogue number
NeuN	Guinea pig	Autoclave Tris-EDTA (pH 9.0)	1:500	Merck	APN90P
Iba1	Chicken	Autoclave Tris-EDTA (pH 9.0)	1:1000	Synaptic systems	234-009
GAD65/67	Rabbit	Autoclave Tris-EDTA (pH 9.0)	1:500	Millipore	AB1511
MFGE8	Mouse	Autoclave Tris-EDTA (pH 9.0)	1:500	R&D Systems	MAB27671
Kindlin3	Mouse	Autoclave Tris-EDTA (pH 9.0)	1:400	Thermofisher Scientific	MA5-26932

4.2.3 Image segmentation of DAB WSIs

WSIs were manually annotated using QuPath, with ROIs placed according to the regime outlined in **2.2.5**, with the addition of additional ROIs in the white matter. ROIs were then exported as geoJSON files.

WSIs were loaded using OpenSlide Python and annotation images extracted by applying annotation geoJSON masks to obtain the annotation bounding box. Pixels outside of the annotation ROI were set to black to preserve only data from within the ROI. The DAB channel was then extracted and enhanced using PIL's PIL.ImageEnhance.Contrast function with a value of 2.5. Enhanced images were then inverted to give strong DAB areas high intensity values. Gaussian blurring (sigma 1.0) was subsequently performed using scikit-image's gaussian filter. Pixel dimensions were derived from the WSI metadata.

Pixel intensities from each enhanced-inverted-smoothed ROI were aggregated at the case level, and a case-wide Otsu threshold determined. Otsu's method was then applied to each ROI to identify objects and create a binary mask. Pixel areas of small objects <150 were removed and the remaining objects cleaned via morphological closing followed by opening (disk size 1.3).

Objects were grouped into <1500 and >1500 pixel area categories, and a separate binary mask created for each. Objects were then skeletonised using the skimage.morphology skeletonize function. Features including branch length, triple points, quad points, end points, and the bounding box were extracted. Data was recorded as individual objects at the case level, and as aggregated at ROI level for the full cohort. Aggregated ROI data was merged with metadata containing demographic and clinical variables. Outlier ROIs were removed from the aggregated data by applying an interquartile range * 1.5 filter to the relevant object density column. This reduced the size of the data set from 2207 to 2104 ROIs. Data was saved as .csv files for later analysis.

Visualisations were created for 10 ROIs per case and visually inspected to ensure quality of segmentation and skeletonization.

4.2.4 Quantification of MFGE8 pixels

MFGE8 did not display a staining pattern that would benefit from object segmentation and morphological quantification, it was therefore analysed by simple positive pixel count using QuPath.

ROIs were transposed from kindlin3 WSIs onto MFGE8 WSIs directly in QuPath via copy and paste. ROIs were then adjusted to account for tissue damage/artefact/large vessels. A pixel thresholder (threshold 0.25) was applied to the DAB channel at full resolution with a gaussian filter.

Data was exported as a .csv file for later analyses.

4.2.5 DAB-IF tissue section alignment

Tissue sections from DAB WSIs were aligned to an adjacent IF tissue section WSI following a procedure modified from **2.2.6**. This differed from the earlier method in that the FIRC channel was extracted and used to extract tissue outlines from IF WSIs.

Following tissue alignment, geoJSONs of annotations from the IF image were applied to the aligned DAB tissue section, with these ROIs extracted as .png files. The corresponding ROIs were then extracted at full resolution from each channel of the IF WSI. This gave sets of matched IF and DAB ROI images, allowing DABs native intensity distribution to be directly used with the IF markers.

4.2.6 Analysis of aligned DAB and IF images

4.2.6.1 NeuN object segmentation

NeuN IF images extracted from the releavant channel of the WSI were processed following a modified version of the method in **2.2.10**.

.png files were loaded using PIL and pixel dimensions extracted from the metadata. NeuN staining within the image was then enhanced via OpenCV Python's contrast limited adaptive histogram equalisation (CLAHE) function (clip limit = 2.5, tile grid size

= 8, 8) within non-black pixels of the image. All enhanced NeuN images within a case were then aggregated and an Otsu threshold determined, and objects segmented using this to generate a binary mask. Masks were cleaned by morphological opening (disk radius 3.0), small object <50 pixel area removal, binary hole filling, and morphological smoothing (disk radius 12.0). Connected components were uniquely labelled, and morphological properties extracted. Object area in μm^2 was measured and object classified as in 1.2.10. To remove doublets that were occasionally present in the DAB NeuN segmentation, objects classified as very large were further segmented via watershed segmentation with 5 iterations, or until objects could not be split further. Objects split this way were added to the binary mask and classified.

Binary masks for all NeuN objects, as well as segmented small, intermediate, large, and very large objects were saved. Visualisations were generated at each stage of the process and visually inspected to ensure quality.

4.2.6.2 DAPI object segmentation

DAPI .png images were loaded using PIL and pixels normalised. The image was then segmented using StarDist with the 2D_versitle_fluo model. Objects resulting from this segmentation were filtered by pixel area(>1000) to remove unsegmented objects. Objects >500 pixel area were assessed with an aspect ratio filter of 3.0 to remove smaller objects consisting of multiple unsegmented nuclei in a line. Cleaned and segmented nuclei were then saved as a binary mask.

4.2.6.3 GAD pixel normalisation

GAD .png images were loaded using PIL. Images were minorly enhanced via CLAHE (clip limit = 0.5, tile grid size = 8, 8). Enhanced images were then min-max normalised at the case level to account for intra-slide intensity variations, and then globally min-max normalised to improve case-case comparability by collecting all case-normalised images across the cohort and performing the normalisation on the aggregated intensity data. Cohort-normalised images were saved as .png files.

4.2.6.4 Iba1 object segmentation

Iba1 .png images were processed to generate initial objects as in **4.2.6.1**, but with less intensive CLAHE (clip limit = 0.5). Following initial object segmentation, binary masks were refined through 5 iterations of morphological closing with disks sizes 3, 3, 2, 2, 1. This was done to connect processes to their parent cell, which the IF signal and thin tissue section often separated. Cleaned binary masks were saved as .png files.

4.2.6.5 Fibrinogen pixel normalisation

Aligned greyscale fibrinogen ROI .png images were loaded using OpenCV, and inverted. Inverted images were then intra-case and cohort-wide normalised as in **4.2.6.3**.

4.2.6.6 Integration of segmented masks and normalised pixel data and neuron-local measurement generation

The output files of **4.2.6.1-5** were matched into per ROI sets by parsing file names to identify case ID, layer annotation type, and unique object ID. Sets of these

measurements were collected and processed sequentially. A cohort-wide GAD threshold was then calculated as 0.8 of the maximum value in the dataset.

NeuN mask of labelled objects. Morphological properties including centroid coordinates, area, perimeter, circularity, and aspect ratio were recorded for all objects. GAD coverage of neurons was then determined by separating the NeuN objects into edge (perimeter thickened to 3px) and interior compartments, and the proportion of each compartment containing GAD over the threshold recorded.

Local NeuN object environments were then recorded within an 80μm radius of the object centroid. This area was split into 5 concentric rings to provide a bulk measure of proximity to neuron, as essential feature due to the large number of objects processed. Within each ring iba1 objects were identified and area and perimeter recorded. GAD proportions within iba1 objects were then recorded as done for NeuN objects. Within the 80μm radius the mean fibrinogen pixel intensity value, and standard deviation of this, were recorded. NeuN objects falling within this radius were identified via KDTree, and the morphological/GAD coverage data, and standard deviation of each measure, of each neighbour objects recorded per neuron size class.

Outliers were removed from the dataset by applying an IQR * 1.5 filter to the overall neuronal density. This generated a comprehensive set of data, with 139,612 individual neurons measured to determine individual and local properties.

To generate non-overlapping regions within ROIs, a random neuron was selected and the Euclidian distance to all other neurons in the ROI calculated. Neurons within 320px (80μm) were removed. This process was repeated per ROI until no neurons were

removed, giving an ROI tiled with non-overlapping measurement areas. Over the cohort this gave 26,008 measurement areas.

4.2.7 Linear mixed models

Linear mixed models were performed as outlined in **2.2.11**.

Briefly, continuous predictors were standardised via z-score transformation, data filtered to match model specification, predictors assessed for multicollinearity with predictors with a VIF > 5.0 removed, and the model specified to minimise AIC and BIC. Resulting coefficient *p* values were corrected for multiple comparisons using BH correction.

4.2.8 Ordinary least squares models

Partial OLS regression models were performed using FOV ROI data aggregated at the cortical layer level for each case ID. Object-level measurements were first aggregated by cortical layer. Numeric columns were standardised via z-score transformation, and categorical variables (e.g., HLA status and sex) were recoded into binary indicators.

Models were fitted using the statsmodels smf.ols function on two aggregated datasets: layers 1–3, and layers 4–6. In each model, cortical layer was included as a categorical fixed effect along with relevant demographic and clinical covariates. Prior to model estimation, predictors with variance inflation factors (VIF) greater than 5.0 were removed to mitigate multicollinearity, and model selection was guided by minimizing AIC and BIC. Finally, coefficient *p* values were adjusted for multiple comparisons using BH correction.

4.2.9 Statistical tests

Statistical tests of group comparisons and regression results were performed as in **2.2.12**.

Briefly, groups were assessed for normality via Shapiro-Wilk test, and Mann-Witney U test performed if one group was non-normally distributed. If both groups were normally distributed a two-way independent t test was performed.

All *p* values were corrected for multiple comparisons using BH correction with an FDR of 0.05.

4.3 Results

4.3.1 Immunohistochemical characterisation of kindlin3 in the multiple sclerosis motor cortex

Kindlin3 was characterised in the sub-cohort of cases used for proteomics. Kindlin3 demonstrated well-defined staining of cells with a microglial/macrophage morphology in the motor cortex (Figure 4.1). Staining was consistent and responsive to the local environment, as demonstrated by the pronounced rim of kindlin3^{+} cells observed around a subpial lesion (**Figure 4.1A, B**). Staining within the grey matter (**Figure 4.1B**) and white matter (**Figure 4.1C**) was similar, with the soma and complex branches of microglia/macrophage outlined. Staining of cells with a monocytic morphology were seen within vessels in each of these locations. No staining of cells with neuronal, astrocytic, oligodendroglial, or endothelial morphologies was seen.

4.3.2 Immunofluorescent characterisation of kindlin3 in the multiple sclerosis motor cortex

IF double labelling of kindlin3 along with either the microglial marker TMEM119 (**Figure 4.1F-H**) or microglia/monocyte-derived macrophage marker iba1 (**Figure 4.1I-K**) showed apparently universal co-expression with each of these markers. Quality of staining was comparable to both TMEM119 and iba1 in terms of structural delineation

4.3.3 Segmentation of kindlin3 and morphological quantification

To determine if kindin3^{+} microglia/macrophage morphology differed depending on extracellular fibrinogen status, a novel segmentation and analysis pipeline was developed (**Figure 4.1E**).

Briefly, ROIs were placed in each cortical layer following the placement strategy/ROI dimensions outlined in **2.2.5.** Full-resolution DAB channel images of each ROI were extracted and contrast enhanced, prior to object segmentation. Objects were classified by size (<1500px area, >1501px area) and each size category separated. Objects were then skeletonised and all individual skeletons quantified.

4.3.4 Kindlin3^{+} cell morphological differences between extracellular fibrinogen deposition conditions

Only large kindin3 objects were used to compare morphological features between F+ and F- cases. This was to allow full cells to have a greater contribution to the analysis.

The density of large kindlin3 objects did not differ between F+ and F- groups in layers 1, 4, 5, and 6, but was significantly higher in the F+ group in the WM ($p = 0.021$), and lower in layers 2 ($p < 0.001$) and 3 ($p = 0.005$) (**Figure 4.1L**).

Within the F+ group large kindlin3 objects on average had significantly more triple points (**Figure 4.1M**) in layers 2 (p = 0.004), 3 (p < 0.001), 4 (p = 0.001), and 6 (p + 0.007).

Mean branch length was shorter in the F+ group across layers 3-6 (all p < 0.001), but showed no differences in layers 1 and 2, or in the WM (**Figure 4.1N**). Variability in branch length was also lower in these layers (layer 3 p = 0.004, layer 4 p = 0.022, layer 5 p = 0.007, layer 6 p = 0.10). Variability was however higher in layer 1 (p = 0.004) in the F+ group (**Figure 4.1O**).

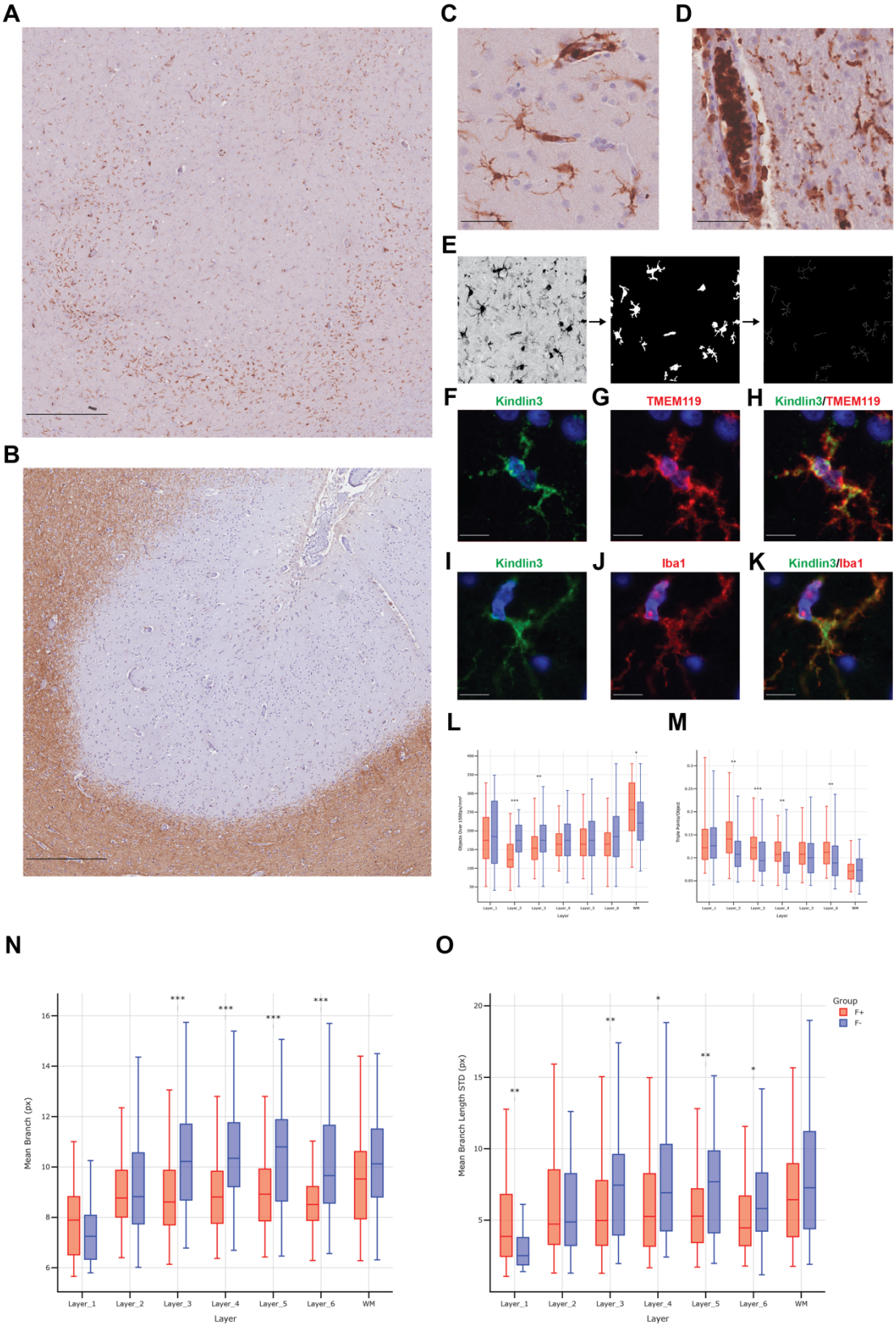

Figure 4.1. Characterisation of kindlin3 in the multiple sclerosis motor cortex. A, B, Kindlin3 shows well-delineated microglial/macrophage staining.

Kindlin3 is strongly expressed at the border of a subpial lesion (**A**), with demyelination demonstrated in an earlier section (**B**). **C**, **D**, kindlin3 expression in the grey matter (**C**) and white matter (**D**) is consistent, with microglia/macrophages in the parenchyma and

probable monocytes within vessels. **E**, image segmentation pipeline for morphological analysis. **F-K**, kindlin3 colocalises with both TMEM119 (**F-H**) and iba1 (**I-K**). **L**, within high (F+) and low (F-) extracellular fibrinogen deposition cases density of large kindlin3 objects does not vary across cortical layers 1 and 4-6, but is lower in layers 2/3, and higher in the white matter. **M**, large kindlin3 objects have more triple points in layers 2, 3, 4, 6 in F+ cases. **N**, **O**, large kindlin3 objects have shorter (N) and less variable (**O**) branch lengths across layers 3-6 in F+ cases. Statistical analyses performed within each layer were selected by testing for normality via Shapiro-Wilk test followed by independent t-test or Mann-Whitney U test. BH correction for multiple comparisons (FDR = 0.05) was applied to all tests. Scale bars represent: 500μm (**A**, **B**), 50μm (**C**, **D**) and 10μm (**F – K**)

4.3.5 Linear mixed effects models of kindlin3$^+$ cell morphology

Table 4.2 shows the outputs of linear mixed effects models of kindlin3$^+$ cell morphology accounting for the extracellular fibrinogen deposition score within the case and demographic and clinical variables.

Layers 1-3 and layers 4-6 were grouped for this analysis. The effect of layer was assessed by including layers as a categorical fixed effect predictor. Total number of cases in these groups differed following the data cleaning process outlined in **4.2.3**.

4.3.5.1 Kindlin3$^+$ cell branch length models

The mean branch length model of layers 1-3 showed a significant effect of layer 1/3 in relation to layer 2, with layer 1 associated with a shorter branch length (β = -0.465, p < 0.001) and layer 3 longer (β = 0.218, p = 0.018). Within these layers the mean number of triple points per object was linked to shorter branch length (β = -1.041, p < 0.001) and bounding box area with greater branch length (β - 1.010, p < 0.001).

The layer 4-6 model did not show a significant effect related to cortical layer. Similar effects to the layer 1-3 model were seen for triple points and bounding box area. Within

this model mean branch length was significantly negatively associated with the layer 5 extracellular fibrinogen deposition semiquantitative score (β = -0.166, p = 0.023), providing support for the group-group comparisons seen discussed in **4.3.5**.

4.3.5.2 Kindlin3^{+} cell bounding box area models

The layer 1-3 model and layer 4-6 did not show significant effects for cortical layer on bounding box area.

Both models displayed similar positive associations between the triple points per object and bounding box area (layer 1-3 model β = 1.019, p < 0.001, layer 4-6 model β = 1.926, p < 0.001), and mean branch length (layer 1-3 model β = 0.083, p < 0.001, layer 4-6 model β = 0.072, p < 0.001).

Both models also showed a positive effect of postmortem interval on bounding box area. This effect was stronger in the layer 4-6 model (β = 0.121, p = 0.011) than the layer 1-3 model (β = 0.063, p = 0.027).

4.3.5.3 Kindlin3^{+} cell end points models

Layer showed significant effects in the layer 1-3 model (layer 1 β = 0.119, p < 0.001, layer 3 β = -0.057, p <0.001)

Triple points per object and bounding box area were positively associated with the number of end points in both models (triple points: layer 1-3 model β = 0.521, p < 0.001,

layer 4-6 model β = 0.401, p < 0.001, bounding box area: layer 1-3 model β = 1.339, p < 0.001, layer 4-6 model β = 0.238, p < 0.001).

Layer 5 extracellular fibrinogen deposition semiquantitative score showed a weak positive association with the number of end points per object (β = 0.014, p = 0.009).

Table 4.2. Extracellular fibrinogen and kindlin3 morphology linear mixed models

Kindlin3 mean branch length models	Layers 1-3 (n = 31)		Layers 4-6 (n = 34)	
	β (95% CI)	Adj *p* value	β (95% CI)	Adj *p* value
Fixed effect: layer 1/4	-0.465 (-0.682 - 0.248)	<0.001	0.107 (-0.019 - 0.232)	0.174
Fixed effect: layer 3/6	0.218 (0.054 - 0.318)	0.018	-0.057 (-0.182 - 0.069)	0.537
Triple points	-1.041 (0.054 - 0.381)	<0.001	-5.610 (-6.503 - -4.717)	<0.001
Bounding box area	1.010 (0.682 - 1.338)	<0.001	1.316 (0.971 - 1.661)	<0.001
Postmortem interval	0.067 (-0.174 - 0.309)	0.713	0.028 (-0.150 - 0.206)	0.842
EC SQ score L2/5	-0.044 (-0.229 - 0.141)	0.713	-0.166 (-0.290 - -0.041)	0.023
Age at death	0.067 (-0.122 - 0.256)	0.698	-0.001 (-0.140 - 0.139)	0.988
HLA-DRB1*1501 positive	-0.039 (-0.418 - 0.339)	0.838	-0.220 (-0.486 - 0.046)	0.174
Sex	0.310 (-0.151 - 0.771)	0.312	-0.123 (-0.466 - 0.220)	0.602
Group Var	0.369 (0.130 - 0.608)	0.006	0.342 (0.114 - 0.570)	0.011
Kindlin3 bounding box area mean models				
Fixed effect: layer 1/4	-0.036 (-0.096 - 0.024)	0.400	0.011 (-0.018 - 0.040)	0.763
Fixed effect: layer 3/6	-0.018 (-0.064 - 0.027)	0.532	0.005 (-0.024 - 0.034)	0.780
Triple points	1.019 (1.004 - 1.033)	<0.001	1.926 (1.676 - 2.175)	<0.001
Mean branch length	0.083 (0.059 - 0.108)	<0.001	0.072 (0.051 - 0.093)	<0.001
Postmortem interval	0.063 (0.016 - 0.110)	0.027	0.121 (0.038 - 0.205)	0.011
EC SQ score L2/5	-0.012 (-0.047 - 0.023)	0.562	-0.011 (-0.070 - 0.049)	0.780
Age at death	0.015 (-0.020 - 0.051)	0.532	0.018 (-0.051 - 0.087)	0.780
HLA-DRB1*1501 positive	-0.003 (-0.075 - 0.068)	0.925	-0.018 (-0.148 - 0.111)	0.780
Sex	0.074 (-0.017 - 0.165)	0.226	0.085 (-0.078 - 0.248)	0.610
Group Var	0.128 (0.013 - 0.243)	0.073	2.058 (0.821 - 3.294)	0.004
Kindlin3 mean end points models				
Fixed effect: layer 1/4	0.119 (0.081 - 0.156)	<0.001	-0.002 (-0.010 - 0.006)	0.664
Fixed effect: layer 3/6	-0.057(-0.085 - -0.028)	<0.001	0.003 (-0.005 - 0.011)	0.660
Triple points	0.521 (0.461 - 0.581)	<0.001	1.339 (1.276 - 1.402)	<0.001
Bounding box area mean	0.401 (0.344 - 0.459)	<0.001	0.128 (0.105 - 0.150)	<0.001
Postmortem interval	-0.045 (-0.090 - 0.001)	0.076	-0.008 (-0.022 - 0.006)	0.478
EC SQ score L2/5	0.009 (-0.026 - 0.044)	0.663	0.014 (0.005 - 0.024)	0.009
Age at death	-0.026 (-0.062 - 0.010)	0.202	-0.001 (-0.012 - 0.010)	0.809
HLA-DRB1*1501 positive	-0.016 (-0.088 - 0.056)	0.663	-0.008 (-0.028 - 0.013)	0.660
Sex	-0.100 (-0.186 - -0.013)	0.041	0.009 (-0.018 - 0.035)	0.660
Group Var	0.461 (0.158 - 0.764)	0.006	0.592 (0.217 - 0.967)	0.007

4.3.6 Ordinary least squares models of the relationship between TMEM119 and iba1 morphologies with kindlin3$^+$ cell morphology

To further explore how kindlin3 related to TMEM119 and iba1, TMEM119 and iba1 DAB WSIs were processed to obtain skeletons and partial OLS models were developed. The outputs of these models are show in **Table 4.3**.

Layers were grouped in these models as in **4.3.6.1**. Layer 1 and layer 4 were used as reference layers for the layer fixed effects.

4.3.6.1 TMEM119/iba1 branch length models

The TMEM119 layer 1-3 model assessing kindlin3$^+$ object branch length was powerfully predictive (adjusted R^2 = 0.780). Layer was a significant effect in this model. (layer 2 β = 0.546, p = 0.036, layer 3 β = 1.002, p < 0.001). TMEM119 mean branch length showed a marginally nonsignificant association with kindlin3 mean branch length (β = 0.248, p = 0.061). The TMEM119 layer 4-6 model was less predictive (adjusted R^2 = 0.286), but did show a significant positive association between TMEM119 and kindlin3 mean branch lengths (β = 0.619, p = 0.033). HLA DRB1*1501 positive status was positively associated with kindin3 mean branch length (β = 0.977, p = 0.050).

The iba1 models did not show a significant effect of layer. The layer 1-3 iba1 model did not have any significant predictors of kindin3 mean branch length. The layer 4-6 iba1 model provided a better account for kindlin3 branch length variation (adjusted R^2 = 0.538) than the TMEM119 model for these layers. Within this model iba1 mean branch length was strongly associated with kindlin3 mean branch length (β = 1.366, p < 0.001).

Age at death (β = -0.498, p = 0.048) and HLA DRB1*1501 positivity (β = -0.795, p 0.029) were additional negative predictors.

4.3.6.2 TMEM119/iba1 triple point models

Within layers 1-3 the TMEM119 model was similarly predictive to the mean branch length model (adjusted R^2 = 0.701). Cortical layer showed a negative effect (layer 2 β = -0.215, p = 0.035, layer 3 β = -0.186, p = 0.001). CSF pH (β = -0.287, p = 0.003) and time from onset to wheelchair (β = -0.065, p = 0.021) were additional negative predictors. No significant predictors were recorded in the TMEM119 layer 4-6 model.

The iba1 layer 1-3 model showed similar relationships to the TMEM119 layer 1-3 model, but was less predictive (R^2 = 0.409) , with layer 3 (β = -0.189, p = 0.018), and time from onset to wheelchair (β = -0.117, p = 0.034) having significant negative effects. Brain weight also emerged as a significant negative predictor (β = -0.155, p = 0.008). As with the TMEM119 model, no significant predictors were seen in the iba1 layer 4-6 model.

Table 4.3. Kindlin3 and TMEM119/Iba1 morphology partial OLS models

	TMEM119				Iba1			
Kindlin3 mean branch length models	Layers 1-3 (n = 23) β (95% CI)	Adj R^2 = 0.780 Adj *p* value	Layers 4-6 (n = 20) β (95% CI)	Adj R^2 = 0.286 Adj *p* value	Layers 1-3 (n = 23) β (95% CI)	Adj R^2 = 0.373 Adj *p* value	Layers 4-6 (n = 28) β (95% CI)	Adj R^2 = 0.538 Adj *p* value
Layer fixed effect: layer 2/5	0.546 (0.041 - 1.051)	0.036	-0.587 (-1.669 - 0.495)	0.257	0.671 (-0.139 - 1.483)	0.097	0.100 (-0.577 - 0.777)	0.761
Layer fixed effect: layer 3/6	1.002 (0.533 - 1.471)	<0.001	-0.729 (-1.667 - 0.209)	0.115	0.521 (-0.542 - 1.584)	0.311	-0.308 (-0.988 - 0.372)	0.355
Mean branch length: Alt marker	0.248 (0.066 - 0.357)	0.061	0.619 (0.061 - 1.177)	0.033	1.139 (-0.086 - 2.364)	0.066	1.366 (0.854 - 1.878)	<0.001
Brain weight	0.473 (0.033 - 0.913)	0.037	0.857 (0.038 - 1.676)	0.042	0.025 (-0.772 - 0.821)	0.948	0.114 (-0.350 - 0.577)	0.613
Age at death	0.057 (-0.262 - 0.376)	0.707	0.401 (-0.404 - 1.207)	0.296	-0.242 (-0.894 - 0.410)	0.440	-0.498 (-0.991 - -0.006)	0.048
CSF pH	0.777 (-0.101 - 1.657)	0.079	-0.223 (-0.695 - 0.249)	0.322	0.011 (-0.578 - 0.601)	0.968	0.105 (-0.304 - 0.515)	0.597
Time onset to wheelchair	0.062 (-0.182 - 0.305)	0.595	0.072 (-0.478 - 0.622)	0.779	-0.323 (-0.863 - 0.218)	0.221	-0.157 (-0.510 - 0.197)	0.366
HLA-DRB1*1501 positive	-0.537 (-1.378 - 0.305)	0.193	0.977 (-0.002 - 1.957)	0.050	-0.604 (-1.638 - 0.430)	0.231	-0.795 (-1.501 - -0.088)	0.029
Kindlin3 mean triple points models		Adj R^2 = 0.701		Adj R^2 = 0.114		Adj R^2 = 0.409		Adj R^2 = 0.232
Layer fixed effect: layer 2/5	-0.112 (-0.215 - 0.009)	0.035	0.036 (-0.096 - 0.169)	0.558	-0.087 (-0.232 - 0.058)	0.219	-0.007 (-0.220 - 0.025)	0.864
Layer fixed effect: layer 3/6	-0.186 (-0.285 - -0.087)	0.001	0.064 (-0.053 - 0.182)	0.252	-0.189 (-0.341 - -0.037)	0.018	0.012 (-0.076 - 0.100)	0.778
Mean triple points: Alt marker	-0.019 (-0.128 - 0.089)	0.706	0.005 (-0.058 - 0.069)	0.861	-0.078 (-0.301 - 0.145)	0.466	0.128 (-0.005 - 0.261)	0.059
Brain weight	-0.034 (-0.131 - 0.064)	0.469	-0.070 (-0.175 - 0.035)	0.169	-0.155 (-0.264 - -0.047)	0.008	-0.030 (-0.092 - 0.032)	0.329
Age at death	0.028 (-0.042 - 0.099)	0.400	-0.045 (-0.140 - 0.051)	0.323	0.002 (-0.084 - 0.088)	0.964	0.028 (-0.028 - 0.085)	0.302
CSF pH	-0.287 (-0.444 - -0.113)	0.003	0.010 (-0.053 - 0.072)	0.735	0.057 (-0.-27 - 0.142)	0.168	0.016 (-0.033 - 0.065)	0.499
Time onset to wheelchair	-0.065 (-0.119 - -0.011)	0.021	-0.036 (-0.099 - 0.026)	0.223	-0.117 (-0.223 - -0.010)	0.034	-0.022 (-0.074 - -0.030)	0.384
HLA DRB1*1501 positive	0.160 (-0.020 - 0.340)	0.077	-0.087 (-0.219 - 0.044)	0.172	-0.117 (-0.333 - 0.099)	0.266	0.030 (-0.060 - 0.120)	0.491

4.3.7 Immunohistochemical characterisation of MFGE8 in the multiple sclerosis motor cortex

MFGE8 was characterised in the sub-cohort used for proteomics. DAB IHC of MFGE8 (**Figure 4.2**) showed a sparse and granular staining pattern across the grey matter (**Figure 4.2A**) and white matter (**Figure 4.2B**). Parenchymal staining in these locations appeared to be glial, with notable neuronal cell surface staining seen consistently. Endothelial cells were occasionally positive, although we did not see the significant vessel-related staining reported in AD[281,282].

4.3.8 Immunofluorescent characterisation of MFGE8 in the multiple sclerosis motor cortex

IF triple labelling with MFGE8, iba1, and NeuN was performed to provide insight into the DAB staining seen (**Figure 4.2C-J**).

MFGE8 did not colocalise with iba1 in either the white matter (**Figure 4.2F**) or grey matter (**Figure 4.2J**) in both normal-appearing and lesional tissue areas. Similar staining to that observed in the DAB was seen for colocalization with NeuN (**Figure 4.2J**), with cell surface granular staining a moderately common phenomenon of variable extent. IF staining of MFGE8 showed striking staining of cells with a fibrous astrocytic morphology in the WM (**Figure 4.2E, F**). Similar astrocytic staining was not observed in the GM.

Double labelling with GFAP unfortunately resulted in high bleed through in the channels used, requiring future experiments to confirm the astrocytic identity of the cells seen in the WM. However, given the lack of iba1 colocalization, and the characteristic morphology, we can be highly confident that these are astrocytes.

4.3.9 Analysis of MFGE8 deposition differences between high and low extracellular fibrinogen deposition multiple sclerosis cases

MFGE8 did not show significant differences between F+ and F- groups with regards to percentage area coverage (**Figure 4.2K**) or variability in percentage area coverage (**Figure 4.2L**).

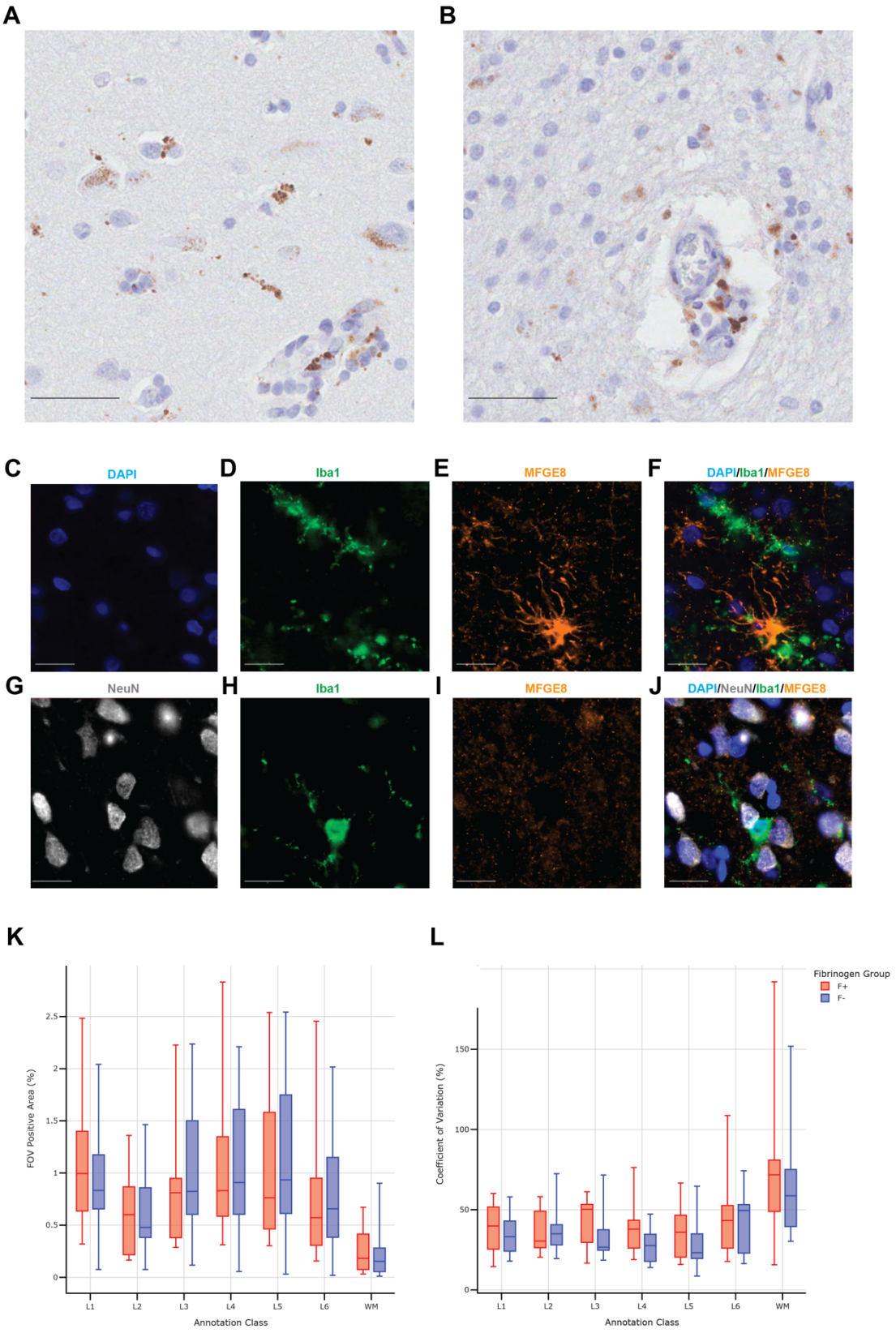

Figure 4.2 Characterisation of MFGE8 in the multiple sclerosis motor cortex.

A, B, MFGE8 displays sparse granular staining in the grey matter (**A**) and white matter (**B**). Staining occurs within glial cells, processes, and on neuronal surfaces. Endothelial staining was occasionally seen. **C – J**, representative images of immunofluorescent

staining of MFGE8 in the white matter (**C – F**) and grey matter (**G – J**). MFGE8 does not colocalise with microglia/macrophages, but does occasionally mark neuronal cell surfaces. MFGE8^{+} cells in the white matter (**E, F**) show a clearly astrocytic morphology. **K, L**, MFGE8 does not significantly vary between high (F+) and low (F-) extracellular fibrinogen deposition cases in area coverage (**K**), or variability of area coverage (**L**). Statistical analyses performed within each layer were selected by testing for normality via Shapiro-Wilk test followed by independent t-test or Mann-Whitney U test. BH correction for multiple comparisons (FDR = 0.05) was applied to all tests. Scale bars represent: 50μm (**A, B**) and 20μm (**C-J**).

4.3.10 Local environment analysis study population

Demographic and clinical features of the MS cases (n = 8) used for IF quantification of NeuN, GAD65/67, and iba1 are shown in **Table 4.4**. Groups did not significantly differ in any of the demographic or clinical variables measured. Of note, all cases were SPMS.

Table 4.4. Local quantification sub-cohort

	F+ (*n* = 4)	F- (*n* = 4)	*P* value
Sex (% female)	50	100	0.55
Disease subtype	SPMS = 4	SPMS = 4	-
Brain weight (g)	1159 (*n* = 4, 995 – 1310)	1047 (*n* = 4, 891 – 1380)	0.43
Postmortem interval (yrs)	19 (*n* = 4, 8.0 – 31.0)	13.5 (*n* = 4, 7.0 – 21.0)	0.40
CSF pH	6.45 (*n* = 2, 6.4 – 6.5)	7.71 (*n* = 3, 6.52 – 9.2)	0.31
Disease duration (yrs)	30 (*n* = 4, 22.0 – 47.0)	32.8 (*n* = 4, 19.0 – 56.0)	0.51
Time onset – wheelchair (yrs)	16.3 (*n* = 3, 5.0 – 23.0)	25.75 (*n* = 4, 12.0 – 30.0)	0.39
Age at death (yrs)	59.5 (*n* = 4, 46.0 – 78.0)	64.75 (*n* = 4, 52.0 – 86.0)	0.62

4.3.11 NeuN – iba1 – GAD65/67 triple immunofluorescent labelling

To determine if the case and group level effects of fibrinogen are a result of local fibrinogen deposition or an effect of some other unknown feature associated with the case, a panel of NeuN, iba1, and GAD65/67 was used for triple labelling (Figure 4.3A-E). Staining was clear throughout all sections used, with minimal intensity variations.

4.3.12 Segmentation of triple labelled immunofluorescent WSIs

Crucial to being able to quantify the effect of fibrinogen on these markers, the IF WSIs obtained from this has an adjacent fibrinogen DAB section aligned to them, allowing the continuous fibrinogen pixel values to be used directly alongside other measurements.

This resulted in an exceptionally rich dataset, with individual neuron measurements recorded following an enhanced NeuN segmentation pipeline to the one used earlier for DAB analysis (**Figure 2.7**). A schematic overlaid onto a multi-labelled image outlines some of these measurements (**Figure 4.3F**) Briefly, for each NeuN object in an image morphology, GAD perimeter coverage, and GAD interior coverage was quantified within the NeuN object, with corresponding measurements taken for all NeuN objects within an 80μm radius of the central object's centroid. Measurements were taken in bulk, and segregated per neuron size class. Iba1 objects were also quantified for morphology and GAD perimeter and interior coverage were also recorded in this area. Fibrinogen was recorded as mean pixel intensity and standard deviation of mean pixel intensity for this area. Once all NeuN object had local environmental conditions measured, NeuN objects were filtered to give individual neuron data (181,132 individual neurons) and data for non-overlapping local areas,

providing comprehensive local-scale coverage of individual ROIs, with this approach applied to millimetres of cortex per layer. Overall, post data cleaning, 23.110 local areas were quantified, representing 464.65mm^2.

Example images of segmented small neurons and iba1 are shown in Figure **4.3G**, **H**.

4.3.13 Group comparisons of triple labelling local measurements

To compare the F+ and F- groups for local measurements data was aggregated at the layer and case level to maximise independence of samples.

Between the 4 F+ and F- cases used in these experiments, local fibrinogen pixel intensity was higher in the F+ group across all cortical layers (**Figure 4.3I**, all p <0.05), but was not more variable (**Figure 4.3J**).

Despite a large median difference across all neuronal cortical layers, the F+ and F- groups did not significantly differ with regards to the proportions of GAD perimeter (**Figure 4.3K**) coverage or GAD interior coverage (**Figure 4.3L**).

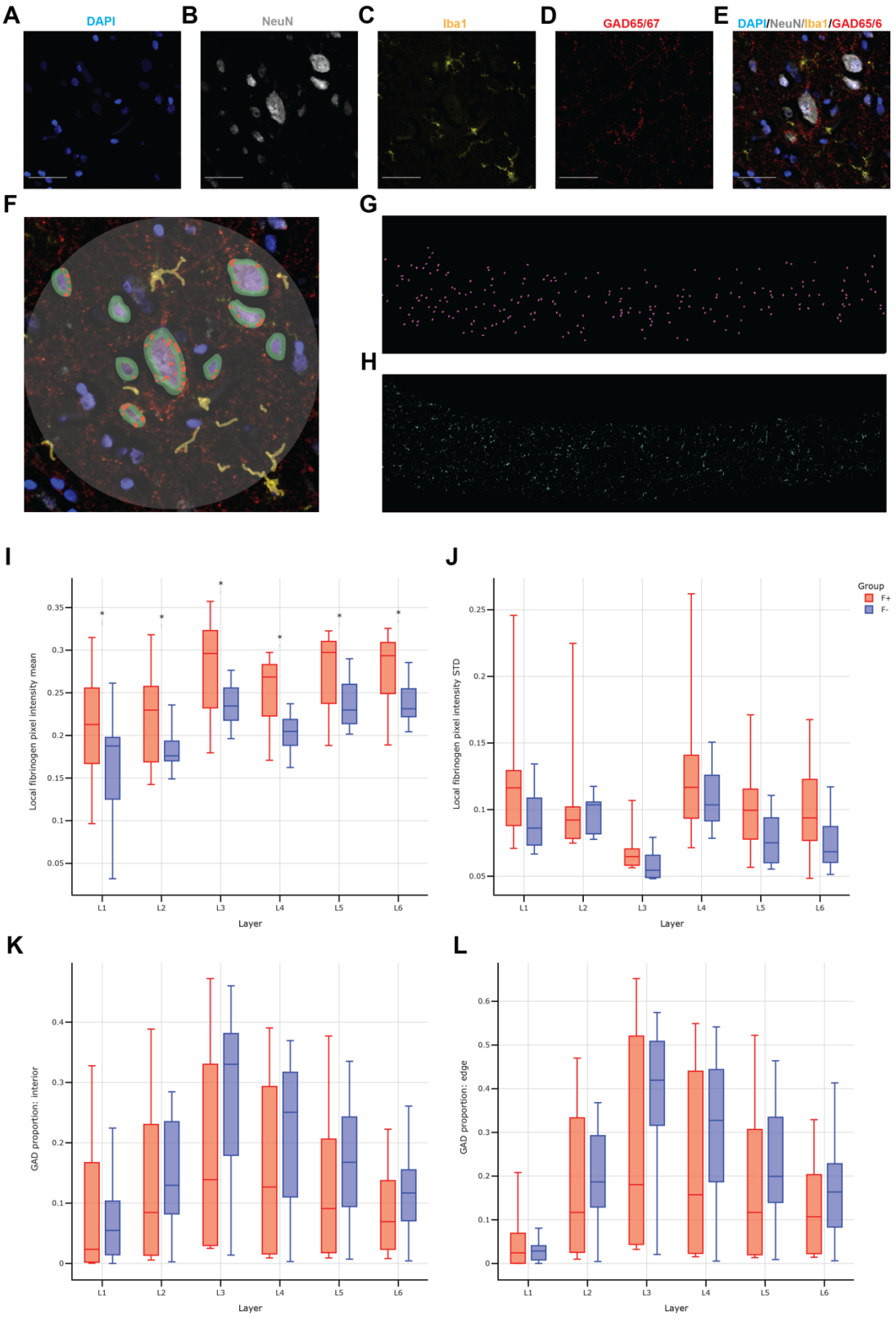

Figure 4.3. Segmentation of NeuN/Iba1/GAD triple labelled immunofluorescent WSIs and group level comparisons of local features.

A – E, representative immunofluorescent images of DAPI (**A**), NeuN (**B**), iba1 (**C**), and GAD65/67 (**D**) used in image segmentation. **F**, example of local measurements.

Measurements were at individual neurons within an 80μm radius of the neuron's centroid. Measurement areas did not overlap. Neuron size, morphology, and local measurements of each of these was recorded. Neurons were classed into distinct size buckets (small 30 - 90μm^2, intermediate 91 - 150μm^2, large 150 - 250μm^2, very large 251μm^2+). GAD coverage for all neurons was recorded along the neuron perimeter (green outline) and interior (purple outline), with equivalent measurements taken in iba1 objects. The top 20% of GAD pixel intensities were classed as positive for this. Local fibrinogen deposition within the radius was recorded from an adjacent aligned fibrinogen DAB section. **G, H**, representative segmentation images of a layer 5 region of interest for small neurons (**G**) and iba1 (**H**). **I, J,** local fibrinogen pixel intensity was higher in high (F+) compared to low (F-) extracellular fibrinogen deposition cases (**I**) but was not significantly more variable (**J**). **K, L**, for all neuron sizes the proportion of the neuron's interior (**K**) and exterior (**L**) was lower in F+ cases, but this did not reach significance. Statistical analyses performed within each layer were selected by testing for normality via Shapiro-Wilk test followed by independent t-test or Mann-Whitney U test. BH correction for multiple comparisons (FDR = 0.05) was applied to all tests. Scale bars represent 20μm.

4.3.14 Linear mixed effects models of the influence of local fibrinogen, microglia/macrophage, neuron, and inhibitory synapse measurements on neuronal densities

Table 4.5 shows the outputs of linear mixed effects models of local neuronal density using a variety of other local measures.

Layer 1 was not included in the analysis due to largely being absent of neurons.

4.3.14.1 Small local neuron density models

Local fibrinogen intensity was positively associated with small neuron density within local areas across layers 2(β = 0.378, p <0.001), 4 (β = 0.155, p < 0.001), 5 (β = 0.038, p < 0.001), and 6 (β = 0.022, p = 0.022). In contrast, local fibrinogen variability was negatively associated with small neuronal density in layers 2 (β = -0.168, p < 0.001), 4 (β = -0.061, p = 0.011), and 6 (β = -0.017, p = 0.024). Layer 3 showed a positive

association between local fibrinogen variability and small neuron density (β = 0.047, p < 0.001).

The total amount of GAD65/67 pixels within iba1 objects in the local area was significantly positively associated with local small neuronal density in layers 2 (β = 0.174, p = 0.037), 3 (β = 0.021, p = 0.040), 4 (β = 0.083, p = 0.013), and 6 (β = 0.064, p < 0.001). The total iba1 area in isolation was negatively associated with small neuron density across layers 3 (β = -0.036, p < 0.001) and 6 (β = -0.016, p < 0.001), and on the threshold of significance in layer 2 (β = -0.100, p = 0.053).

Local intermediate neuronal density was positively associated with local small neuronal density in layers 3-6, with decreasing coefficients over this range (layer 3: β = 0.118 p < 0.001, layer 4: β = 0.108, p < 0.001, layer 5: β = 0.071, p < 0.001, layer 6: β = 0.044 $p,$ < 0.001). local intermediate GAD65/67 perimeter coverage also positively associated with small neuronal density, with this significant in layer 4 (β = 0.089 p < 0.001). the circularity of local intermediate neurons negatively associated with small neuronal density in layers 3 (β = -0.066, p = 0.03), 4 (β = -0.231, p < 0.001), and 6 (β = -0.050, p = 0.022).

GAD perimeter coverage of small neurons within the same local environment negatively associated with small neuronal density in layer 2 (β = -0.130, p = 0.037), but was weakly positively associated in layer 6 (β = 0.029, p = 0.002).

Circularity of small neurons within a local environment was robustly positively associated with small neuronal density (all p < 0.001).

4.3.14.2 Intermediate local neuron density models

Local fibrinogen intensity showed a positive relationship with local intermediate neuronal density in layers 2 (β = 0.187, p < 0.001), 4 (β = 0.184, p < 0.001), and 6 (β = 0.139, p < 0.001). The variability of local fibrinogen intensity was significantly negatively associated with local intermediate neuronal density across all cortical layers (layers 2, 3, 5, 6 p < 0.001, layer 4, p = 0.005).

GAD within iba1 objects demonstrated a positive relationship with intermediate neuron density in layers 5 (β = 0.058, p = 0.008) and 6 (β = 0.142, p < 0.001). Total iba1 area was negatively associated with neuronal density, but only reached significance in layer 6 (β = -0.039, p < 0.001).

The density of local small neurons positively associated with local intermediate neuron density in layers 3 – 6 (all p < 0.001). Local small neuron GAD perimeter coverage was positively related to local intermediate neuron density in all layers other than 4. Circularity of local small neurons was significantly negatively associated with local intermediate neuron density in layer 6 β = 0.108, p < 0.001) but showed a trend towards a similar relationship in layer 3-5.

Local GAD perimeter coverage of intermediate neurons positively associated with intermediate neuron density in layer 2 (β = 0.109 p = 0.005), 3 (β = 0.032, p < 0.001), and 6 (β = 0.150, p < 0.001).

Circularity of local intermediate neurons was powerfully positively related to their density (all β > 1.00, all p < 0.001).

4.3.14.3 Large local neuron models

Local fibrinogen intensity positively related to local large neuron density, with this reaching significance in layers 3 (β = 0.034, p = 0.022) and 4 (β = 0.045, p = 0.015). As with the models for neurons of other sizes, the variability in fibrinogen intensity was negatively associated with local large neuronal density (layer 2: β = -0.030, p = 0.035, layer 3: β = -0.082, p < 0.001, layer 4: β = -0.030, p = 0.032, layer 5: β = -0.043, p = 0.001, layer 6: β = -0.116, p < 0.001).

GAD within iba1 objects showed positive relationships in layers 2 (β = 0.086, p = 0.030) and 6 (β = 0.104, p < 0.001). Total iba1 area only demonstrated a negative relationship in layer 6 (β = -0.025, p = 0.012).

The density of small neurons in the local environment was negatively associated with the density of large neurons (layer 2: β = -0.039, p < 0.001, layer 3: β = -0.062, p < 0.001, layer 6: β = -0.116, p = 0.004). GAD perimeter coverage of local small neurons was only significant in layer 6 (β = -0.166, p = 0.023). Circularity of small neurons showed no significant relationships to large neuron local densities.

GAD perimeter coverage demonstrated a positive relationship over layers 2-5 (all p , 0.001), and was marginally nonsignificant in layer 6 (β = 0.075, p = 0.080). As with all other models, circularity of large neurons positively associated with their density (all β > 1.000, all p < 0.001).

Table 4.5. Local fibrinogen, inhibitory synapse, iba1, and neuronal density linear mixed models

Regression coefficients from linear mixed models to assess the influence fibrinogen, Iba1, morphology, and inhibitory synapses on local neuronal densities

	Layer 2 (n = 2099)		Layer 3 (n = 9938)		Layer 4 (n = 2464)		Layer 5 (n = 4358)		Layer 6 (n = 4251)	
Small local neuron models	β (95% CI)	Adj *p* value	β (95% CI)	Adj *p* value	β (95% CI)	Adj *p* value	β (95% CI)	Adj *p* value	β (95% CI)	Adj *p* value
Local fibrinogen intensity SD	-0.168 (-0.602 - -0.112)	<0.001	0.047 (0.030 - 0.065)	<0.001	-0.061 (-0.104 - -0.017)	0.011	0.001 (-0.015 - 0.016)	0.948	-0.017 (-0.031 - 0.-0.003	0.024
Local fibrinogen intensity mean	0.378 (0.303 - 0.452)	<0.001	0.003 (-0.019 - 0.024)	0.818	0.155 (0.102 - 0.207)	<0.001	0.038 (0.018 - 0.057)	<0.001	0.022 (0.022 - 0.040)	0.022
Local GAD/Iba1 area	0.174 (0.029 - 0.320)	0.037	0.021 (0.003 - 0.039)	0.040	0.083 (0.020 - 0.145)	0.013	0.015 (-0.009 - 0.039)	0.318	0.064 (0.037 - 0.091)	<0.001
Local iba1 area	-0.100 (-0.193 - -0.006)	0.053	-0.036 (-0.052 - -0.019)	<0.001	-0.007 (-0.063 - 0.050)	0.819	-0.008 (-0.028 - 0.013)	0.563	-0.016 (-0.023 - -0.008)	<0.001
Local int neuron density	-0.054 (-0.111 - 0.003)	0.078	0.118 (0.101 - 0.134)	<0.001	0.108 (0.068 - 0.149)	<0.001	0.071 (0.053 - 0.090)	<0.001	0.044 (0.028 - 0.059)	<0.001
Local int neuron GAD cover	0.102 (0.010 - 0.195)	0.051	0.004 (-0.012 - 0.019)	0.698	0.089 (0.044 - 0.135)	<0.001	0.011 (-0.006 - 0.029)	0.315	0.021 (0.000 - 0.043)	0.057
Local int neuron circularity	-0.026 (-0.250 - 0.197)	0.817	-0.066 (-0.119 - -0.012)	0.032	-0.231 (-0.375 - -0.088)	0.003	-0.040 (-0.084 - 0.004)	0.194	-0.050 (-0.090 - 0.010)	0.022
Local small neuron GAD cover	-0.130 (-0.237 - -0.024)	0.037	-0.013 (-0.028 - 0.003)	0.164	-0.040 (-0.086 - 0.006)	0.114	0.004 (-0.012 - 0.020)	0.694	0.029 (0.012 - 0.047)	0.002
Local small neuron circularity	1.410 (1.102 - 1.718)	<0.001	0.855 (0.812 - 0.899)	<0.001	0.916 (0.002 - 0.669)	<0.001	0.635 (0.603 - 0.667)	<0.001	0.588 (-0.003 - 0.062)	<0.001
Group var	0.815		0.115		0.335		0.031		0.030	
Intermediate local neuron models										
Local fibrinogen intensity SD	-0.094 (-0.135 - -0.053)	<0.001	-0.095 (-0.116 - 0.075)	<0.001	-0.066 (-0.108 - -0.025)	0.005	-0.061 (-0.086 - 0.036)	<0.001	-0.079 (-0.107 - -0.050)	<0.001
Local fibrinogen intensity mean	0.187 (0.132 - 0.243)	<0.001	-0.003 (-0.028 - 0.022)	0.829	0.184 (0.134 - 0.235)	<0.001	0.029 (-0.004 - 0.061)	0.107	0.139 (0.103 - 0.175)	<0.001
Local GAD/Iba1 area	0.096 (-0.013 - 0.206)	0.122	0.006 (-0.015 - 0.027)	0.728	-0.025 (-0.085 - 0.036)	0.530	0.058 (0.019 - 0.096)	0.008	0.142 (0.090 - 0.194)	<0.001
Local iba1 area	0.021 (-0.050 - 0.091)	0.624	-0.014 (-0.033 - 0.005)	0.233	-0.007 (-0.062 - 0.048)	0.886	-0.033 (-0.065 - 0.000)	0.080	-0.039 (-0.054 - -0.024)	<0.001
Local small neuron density	-0.031 (-0.063 - 0.001)	0.100	0.159 (0.136 - 0.182)	<0.001	0.104 (0.066 - 0.142)	<0.001	0.176 (0.130 - 0.223)	<0.001	0.162 (0.103 - 0.221)	<0.001
Local small neuron GAD cover	0.103 (0.022 - 0.183)	0.024	0.048 (0.029 - 0.066)	<0.001	0.032 (-0.013 - 0.077)	0.322	0.031 (0.006 - 0.056)	0.032	0.063 (0.029 - 0.097)	<0.001
Local small neuron circularity	0.034 (-0.203 - 0.271)	0.779	-0.032 (-0.086 - 0.022)	0.357	-0.062 (-0.204 - 0.080)	0.530	-0.055 (-0.114 - 0.004)	0.095	-0.108 (-0.169 - -0.047)	<0.001
Local int neuron GAD cover	0.109 (0.040 - 0.179)	0.005	0.032 (0.014 - 0.050)	<0.001	0.001 (-0.043 - 0.046)	0.959	0.021 (-0.006 - 0.048)	0.143	0.150 (0.108 - 0.192)	<0.001
Local int neuron circularity	1.251 (1.090 - 1.411)	<0.001	1.247 (1.190 - 1.304)	<0.001	1.260 (1.129 - 1.391)	<0.001	1.089 (1.027 - 1.151)	<0.001	1.051 (0.980 - 1.122)	<0.001
Group var	0.151		0.081		0.165		0.104		0.052	
Large local neuron models										
Local fibrinogen intensity SD	-0.030 (-0.054 - -0.005)	0.035	-0.082 (-0.103 - -0.061)	<0.001	-0.030 (-0.054 - -0.006)	0.032	-0.043 (-0.067 - -0.019)	0.001	-0.116 (-0.148 - 0.084)	<0.001
Local fibrinogen intensity mean	0.009 (-0.054 - -0.005)	0.740	0.034 (0.008 - 0.060)	0.022	0.045 (0.014 - 0.076)	0.015	0.011 (-0.020 - 0.043)	0.813	0.034 (-0.007 - 0.074)	0.133
Local GAD/Iba1 area	0.086 (0.019 - 0.153)	0.030	-0.003 (-0.025 - 0.018)	0.792	0.015 (-0.028 - 0.057)	0.719	0.009 (-0.030 - 0.047)	0.665	0.104 (0.040 - 0.167)	0.003
Local iba1 area	0.034 (-0.009 - 0.077)	0.196	0.009 (-0.029 - 0.011)	0.540	-0.014 (-0.053 - 0.026)	0.719	0.006 (-0.027 - 0.039)	0.732	-0.025 (-0.044 - -0.007)	0.012
Local small neuron density	-0.039 (0.058 - 0.020)	<0.001	-0.062 (-0.086 - -0.038)	<0.001	0.016 (--0.012 - 0.043)	0.515	0.003 (-0.045 - 0.050	0.915	-0.116 (-0.189 - -0.043)	0.004
Local small neuron GAD cover	0.001 (-0.045 - 0.047)	0.970	0.014 (-0.005 - 0.033)	0.228	0.002 (-0.030 - 0.033)	0.948	-0.004 (-0.029 - 0.021)	0.731	-0.166 (-0.290 - 0.041)	0.023
Local small neuron circularity	0.047 (-0.105 - 0.196)	0.740	0.020 (-0.037 - 0.077)	0.605	0.005 (-0.098 - 0.108)	0.925	0.029 (-0.30 - 0.088)	0.988	0.001 (-0.042 - 0.043)	0.977
Local large neuron GAD cover	0.139 (0.101 - 0.177)	<0.001	0.128 (0.109 - 0.148)	<0.001	0.100 (0.069 - 0.130)	<0.001	0.059 (0.029 - 0.089)	<0.001	0.075 (-0.002 - 0.152)	0.080
Local large neuron circularity	1.469 (1.391 - 1.547)	<0.001	1.569 (1.518 - 1.622)	<0.001	1.519 (1.444 - 1.594)	<0.001	1.617 (1.564 - 1.671)	<0.001	1.864 (1.788 - 1.940)	<0.001
Group var	0.010		0.029		0.010		0.022		0.014	

4.4 Discussion

Previous research has demonstrated that at the case level fibrinogen is associated with reduced neuronal density in cases with high extracellular fibrinogen deposition[191], and that in model systems application of fibrinogen is sufficient to induce demyelination[247], axonal damage[198], and promote synapse loss[202]; however, these effects have not been demonstrated to occur locally in the human brain in altered fibrinogen environment. This chapter accomplishes this by leveraging prior results that showed altered morphology, inhibitory synapses, and microglia/macrophages associate with neuronal loss in high fibrinogen cases, and isolating the effect of local-scale fibrinogen deposition by rigorously accounting for these variables. I demonstrate here that high variability in fibrinogen deposition, as opposed to high total deposition, negatively associates with loss of small, intermediate, and large neurons in the motor cortex of MS cases.

Additionally, I validate two novel markers in the context of the MS motor cortex, kindlin3, and MFGE8. Demonstrating morphological changes indicative of more, but shorter, branches in microglia/macrophages in high fibrinogen conditions.

Kindlin3 has not previously been characterised in the MS brain. **Figure 4.1** shows kindlin3 to be an equally well delineating marker of microglia/macrophages to the gold-standard TMEM119 and iba1 markers. However, kindlin3 morphology does not correlate exactly to TMEM119 or iba1 morphology (**Table 4.3**), suggesting it may at least in part perform a different function to these markers. Indeed, while iba1 is commonly considered a microglia-specific marker, it is expressed by the monocyte lineage[283–285]. Kindlin3 has been shown to play different roles in microglia and

monocyte-derived macrophages, with kindlin3 deficiency severely impairing the migratory capabilities of monocyte-derived macrophages, but not microglia, *in vivo* in a mouse model. This study also demonstrated kindlin3 to regulate the speed of microglial process extension towards focal injury site, with deficiency slowing this response[286]. However, this study used iba1 as a microglia-specific marker, which may not be completely accurate, and complicates considering its results in the context of the results presented in this chapter. Intriguingly, postmortem interval was associated with increased bounding box area of kindlin3 objects in this study (**Table 4.2**). Given kindlin3's position as a key integrin adapter, which independently facilitates microglia tissue stiffness sensing[260], it is possible that changes in tissue integrity postmortem might influence the observed microglia/macrophage morphologies. Kindlin3's relevance to motility and phagocytosis within microglia/macrophages is increasingly recognised[260,287] making further analysis of differential responses/expression/location in $TMEM119^{+}$ and $iba1^{+}$ cells crucial.

The lack of significant difference between the F+ and F- groups for MFGE8 (**Figure 4.2**) is likely a result of a small absolute difference, possibly compounded by the fibrinogen effect on this marker altering the cellular compartment MFGE8 resides in. MFGE8's role in synapse loss in AD models occurs following astrocytic secretion of MFGE8[251,252]. Therefore, as our microglia-enriched proteomic data showed reduced MFGE8 expression in F+ cases, along with reduced inhibitory synaptic markers, the state *in situ* postmortem could be either that synapses have already been lost at the point of study and MFGE8 is correspondingly lost from synapses only, or that MFGE8 is reduced in astrocytes and by extension synapses. If the first option were true, this would make detecting differences in overall expression difficult without quantifying

MFGE8 in different cell types. This was an attempted experiment in this study, but issues with channel bleed through could not be resolved at point of thesis submission.

The effect direction of fibrinogen on inhibitory synapse expression in the motor cortex was validated in this chapter (**Figure 4.3K, L**). Whilst this did not reach significance, the large differences in median coverage of neurons between F+ and F-, with F- case neurons having ~90% more GAD coverage, is supportive of the effect seen in the proteomics. That a large median difference was observed in a small cohort is hopeful for a true difference across a larger cohort. Mechanistically, the removal of inhibitory inputs to cortical neurons might promote cell survival by increasing synchronised firing rates and resultant increases in CREB activity[288] or further neuronal activity-related survival genes[289,290]. During development this is a crucial mechanism of neuron death[291,292], but within the neurodegenerative context it is little studied.

Most notable of the results in this chapter is that the negative association between fibrinogen deposition and neuronal density extends from the case/large region level to the local level (**Table 4.5**). Surprisingly, this effect was related to the variability in local fibrinogen deposition as opposed to simply high fibrinogen deposition. Whilst this confirms the association between fibrinogen and neuronal density, at this stage it requires careful consideration. High overall fibrinogen intensity was associated with increased neuronal density in the local analysis here, after accounting for a wide variety of other factors. Given the possibility for cellular fibrinogen uptake (demonstrated in **Figure 2.1** and extensively discussed in **2.4**) which might not be inflammation-provoking, and could skew local intensity measurements to be very high, caution is required. Alternatively, this effect could be real but difficult to identify without accounting for the wide range of contributory factors as was done here.

That the negative association between fibrinogen persists at small local scales ($0.02mm^2$), which suggests local vascular damage is sufficient to cause local neuronal loss, raises an important question; could any functional loss caused by fibrinogen's neuronally deleterious effects be mitigated by careful vascular management? Limited evidence suggests that vascular dysfunction, might influence clinical outcomes in MS[293], with arterial stiffness negatively associated with cognition as measured by the symbol digit modalities test[294]. Systemic circulatory dysfunction can lead to cerebrovascular changes[295], with murine work linking stiffness of the carotid artery with BBB integrity reductions and cognitive impairment[296]. Given the possibility of this being a modifiable severity factor in MS, and also in other neurodegenerative diseases, attempts should be made to assess the systemic vascular contribution to clinical and pathological outcomes.

Overall, this chapter has increased the resolution of our understanding of fibrinogen and neurodegeneration in the human brain. The analysis methods developed here have broad potential to incorporate new features, and cover larger cohorts, further refining our understanding of a crucial, but often overlooked, source of neuronal loss.

Chapter 5 | Final conclusions and future directions

5.1 Thesis summary

This thesis aimed to determine how fibrinogen relates to neuronal density in the MS motor cortex, and how this effect might be mediated. To achieve this aim, a variety of novel analysis methods were developed to directly complement the extensive collection of well-defined postmortem MS tissue available for study. Further insights were gained by a unique anatomically and cell type enriched approach to proteomics. It is only through the combination of these techniques that novel observations have been made.

Summaries of the main findings of this thesis are found below:

5.1.1 Fibrinogen deposition in the multiple sclerosis motor cortex is heterogenous and relates to neuronal density in a partially neuron size dependant manner

This thesis extensively characterised the deposition patterns of fibrinogen in the MS motor cortex. This demonstrated that multiple fibrinogen deposition patterns can occur in proximity, and that the type of deposition is crucial for pathological outcome.

Even within a single deposition type, fibrinogen can show large effect size differences over relatively short distances of cortex. This is exemplified here by extracellular fibrinogen deposition in the grey matter, which could range in effect size by >1SD over distances in the 10s of μm. It is therefore obvious that for the true effect of fibrinogen to be quantified it must be done at local scale.

Our understanding of the effect of fibrinogen on neuronal density was extended to consider size of neuron as a factor, with this revealing that small and intermediate neurons appear particularly susceptible to the injurious effects of fibrinogen. Also included here is the novel observation that after accounting for other important factors such as fibrinogen and neuronal morphology, HLA DRB1*1501 has a negative association with neuronal density.

5.1.2 The microglial proteome is distinct, and inhibitory synapses are lost, in high extracellular fibrinogen environments

By combining proteomics with anatomical focus and cell type-enrichment, this thesis identified several candidate proteins and processes altered by high extracellular fibrinogen deposition.

In the high extracellular fibrinogen context microglia appear to shift towards glycolysis and may lose electrons from within the electron transport chain, contributing to the production of radical oxygen species known to occur in response to fibrinogen. Frataxin deficiency was identified as a potential contributor to this phenomenon. Further, MFGE8, a protein of recent interest to the neurodegeneration research community due to its role in synapse removal, and kindlin3, an integrin binding protein with roles in microglial motility and tissue sensing, were identified as linked to the microglial response to fibrinogen.

Kindln3 was validated across our postmortem cohort, with alterations in kindlin3^{+} cells seen in high extracellular fibrinogen cases. This provides evidence for microglia/macrophages in the human brain being responsive to extravasated plasma proteins.

5.1.3 The negative association between fibrinogen features and neuronal density extends to the cell-local scale

Most importantly, by building on the insights gained earlier in the study, and maximising the use of the resources available, the resolution at which we could confirm fibrinogen as negatively associated with neuronal density has been increased from the level of group comparisons to local neuronal environments.

This not only confirmed the relationship between fibrinogen and neurons to occur at small scales, but it also further underlined the role of fibrinogen deposition type, with variability in staining emerging as the relevant predictor of lower neuronal density. We also further confirm our proteomics data by observing GAD65/67 neuron coverage to be associated with increased neuronal density. Surprisingly, local GAD65/67 within iba1 objects also positively associated with neuronal density, whilst total iba1 had a negative relationship with neuronal density across a range of cortical layers and neuron size classes.

This work provides a springboard for future detailed studies of the relationship between different morphological and spatial features in relation to neurodegeneration.

5.2 Study limitations

Whilst every effort was made during this study to overcome limitations, it is evident that limitations remain.

The primary limitation of this work is that it exclusively relied on postmortem tissue. Postmortem tissue provides a rich landscape for understanding the final state of a neurodegenerative disease, but it lacks the crucial timeseries required to see how a

factor influences the change in a variable. Whilst pathology is often the only way to understand the *in situ* cellular environment, it can be supplanted with data from other sources such as neuroimaging to add a timeseries component to structural/spatial analyses. However, even this cannot truly model the dynamic processes of neuron-glia interactions, necessitating the integration of model systems to understand potential mechanisms incompletely explored in the literature, such as those proposed in this study.

It is also important to recognise the limitations of sample size in this study. Unexpected variability between cases resulted in a relatively low number of proteins being identified in our proteomic analyses. It is likely this was due to the cumulative effect of fibrinogen variation along layer 5 of the motor cortex over several slides reducing the total fibrinogen difference between high and low fibrinogen cases. Despite this, by seeking expert collaborator guidance some insight was gained from the proteomics. Future targeted proteomic work can mitigate this issue by properly modelling the fibrinogen variation along the cortex in the cases to be studied instead of relying on a single case level static score.

I am also aware of the potential for spatial distorting in the analyses related to normalised fibrinogen images. The motor cortex is an exceptionally varied structure when processed as FFPE blocks, therefore, to perform spatial analyses images had to be normalised to a common space. This issue is being actively resolved via the development of non-scaling cortical flattening pipeline.

5.3 Future work

This study has provided a rich dataset for investigating focussed research questions and has provided a variety of image analysis pipelines that can be expanded to quantify further hard to measure phenomena in the brain. Future work to develop the existing analyses and add new data are briefly discussed here:

5.3.1 Astrocyte MFGE8 relationships in the multiple sclerosis motor cortex

To further validate MFGE8 as a protein of relevance to fibrinogen extravasation and MS, the IF analysis pipeline used in **chapter 4** will be adapted for use with further distinct markers (GFAP, MFGE8, NeuN, GAD65/67). Quantification and segmentation of $GFAP^+$ astrocyte morphology over large areas represents a particular challenge for this analysis. However, ongoing work to develop a cost-based approach to reconstructing skeleton structures offers a solution to this problem. Briefly, this involves first segmenting all nuclei in an IF WSI, prior to cell type assignment based on the marker panel used. Cell-specific nuclei are then iterated through and a cost-based function to trace intensity structures is run. This requires significant knowledge of $GFAP^+$ astrocyte morphology to implement. Colleagues within the DeLuca lab will prove to be an invaluable resource for this.

5.3.2 Neuronal density and synapse measurement cohort expansion

The results provided in **chapter 4** serve as a proof of concept of local density measurements. However, to confirm the findings a larger cohort is required. It is anticipated that this will be sourced from within the well-characterised cohort of 71 MS

and 7 control cases outlined in **chapter 2.** This is a simple goal of cohort expansion, for which the existing panel of markers (NeuN, iba1, GAD65/67) will be used.

5.3.3 Large-scale cortical spatial analyses

The image analysis methods developed and used within this study serve as a starting point for continuous iterative refinement. Refinement of the cortical ROI normalisation code is required to minimise any influence of scaling. To achieve this, work on a large-scale cortical flattening pipeline is ongoing. This uses a modified version of the approach used in this study to receive a series of complex and large polygon, tile the ROIs, flatten the columns, split shapes to a common size, join adjacent ROIs, and perform a minimal cropping/interpolation step. It is anticipated that this will allow for spatial analyses within and between cases with significantly less distortion than introduced in this study.

5.3.4 Functional assessment of the effect of fibrinogen on neuronal morphology and inhibitory synapse coverage

To test the effect of fibrinogen/fibrin administration on neuronal morphologies and densities, alongside inhibitory synapse coverage, dynamically, use of a model system is required. Advances in *in vitro* have produced relevant synaptic co-culture systems[297] that can be adapted for this purpose. Indeed, Dr Jonathan Pansieri a trusted lab colleague has been working with collaborators on similar approaches for some time, providing direct expertise to achieve this goal. This would allow us to quantify in real time how neurons and microglia respond to fibrinogen together, and how this relates to morphology and density.

5.4 Concluding thoughts

To summarise briefly, this thesis used a large postmortem cohort of MS cases to characterise and quantify fibrinogen deposition in the motor cortex, with this serving a tool for proteomic analyses, and subsequent detailed image analysis. By using this approach, I have shown:

1) Fibrinogen is extensively and heterogeneously deposited across the motor cortex, with this variability being key to pathological outcomes.
2) The proteome of microglia is responsive to extracellular fibrinogen deposition and suggests a glycolytic shift and the generation of ROS. This phenotype associates with reduced inhibitory synapse coverage.
3) The negative association between fibrinogen deposition and neuronal density persists at small scales and after accounting for a diverse range of additional factors. This association varies slightly by cortical layer, but more prominently by size of affected neuron.

Together this data confirms fibrinogen as a protein associated with neuronal loss and outlines how this end state may develop via altered microglia responses. This thesis provides a wealth of data for integration into new research questions and advances our understanding of a crucial and potential modifiable degenerative process in the human brain.

Chapter 6 Appendix

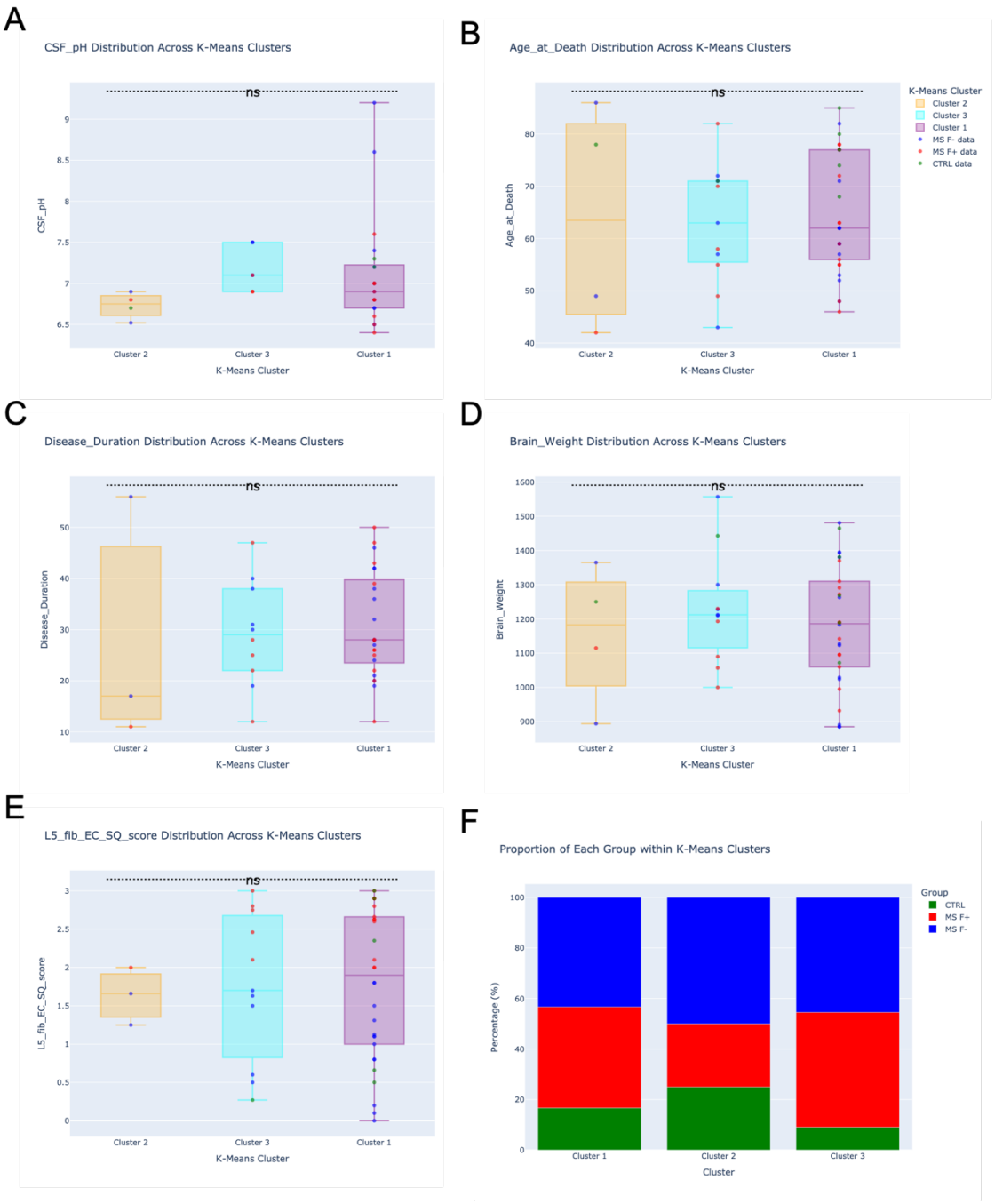

Figure 6.1 Proteomic k means clusters do not vary with regards to demographic or clinical factors. **A – E,** one-way ANOVA results of the effect of cluster on CSF pH (**A**), age at death (**B**), disease duration (**C**), brain weight (**D**), and layer 5 fibrinogen semiquantitative score (**E**). **F**, clusters do not differ with regard to MS subtype or control inclusion. Differences assessed via one-way ANOVA.

Chapter 7 | References

1. Kant, J. A. *et al.* Evolution and organization of the fibrinogen locus on chromosome 4: gene duplication accompanied by transposition and inversion. *Proc. Natl. Acad. Sci. U. S. A.* **82**, 2344–2348 (1985).
2. Roy, S. N., Mukhopadhyay, G. & Redman, C. M. Regulation of fibrinogen assembly. Transfection of Hep G2 cells with B beta cDNA specifically enhances synthesis of the three component chains of fibrinogen. *J. Biol. Chem.* **265**, 6389–6393 (1990).
3. Roy, S., Overton, O. & Redman, C. Overexpression of any fibrinogen chain by Hep G2 cells specifically elevates the expression of the other two chains. *J. Biol. Chem.* **269**, 691–695 (1994).
4. Wolberg, A. S. Fibrinogen and fibrin: synthesis, structure, and function in health and disease. *J. Thromb. Haemost.* **21**, 3005–3015 (2023).
5. Fish, R. J. & Neerman-Arbez, M. Fibrinogen gene regulation. *Thromb. Haemost.* **108**, 419–426 (2012).
6. Espitia Jaimes, C., Fish, R. J. & Neerman-Arbez, M. Local chromatin interactions contribute to expression of the fibrinogen gene cluster. *J. Thromb. Haemost.* **16**, 2070–2082 (2018).
7. Courtois, G., Morgan, J. G., Campbell, L. A., Fourel, G. & Crabtree, G. R. Interaction of a liver-specific nuclear factor with the fibrinogen and alpha 1-antitrypsin promoters. *Science* **238**, 688–692 (1987).
8. Bach, I., Mattei, M. geneviéve, Cereghini, S. & Yaniv, M. Two members of an HNF1 homeoprotein family are expressed in human liver. *Nucleic Acids Res.* **19**, 3553–3559 (1991).
9. Takiguchi, M. The C/EBP family of transcription factors in the liver and other organs. *Int. J. Exp. Pathol.* **79**, 369 (1998).
10. Hu, C.-H., Harris, J. E., Davie, E. W. & Chung, D. W. Characterization of the 5′-Flanking Region of the Gene for the α Chain of Human Fibrinogen (*). *J. Biol. Chem.* **270**, 28342–28349 (1995).
11. Dalmon, J., Laurent, M. & Courtois, G. The human beta fibrinogen promoter contains a hepatocyte nuclear factor 1-dependent interleukin-6-responsive element. *Mol. Cell. Biol.* **13**, 1183 (1993).
12. Kuo, C. J. *et al.* A transcriptional hierarchy involved in mammalian cell-type specification. *Nature* **355**, 457–461 (1992).
13. Fort, A. *et al.* A liver enhancer in the fibrinogen gene cluster. *Blood* **117**, 276 (2010).
14. Fish, R. J. & Neerman-Arbez, M. A novel regulatory element between the human FGA and FGG genes. *Thromb. Haemost.* **108**, 427–434 (2012).
15. Hu, C.-H., Harris, J. E., Davie, E. W. & Chung, D. W. Characterization of the 5′-Flanking Region of the Gene for the α Chain of Human Fibrinogen. *J. Biol. Chem.* **270**, 28342–28349 (1995).
16. Anderson, G. M., Shaw, A. R. & Shafer, J. A. Functional characterization of promoter elements involved in regulation of human B beta-fibrinogen expression. Evidence for binding of novel activator and repressor proteins. *J. Biol. Chem.* **268**, 22650–22655 (1993).
17. Zhang, Z. & Fuller, G. M. Interleukin 1β inhibits interleukin 6–mediated rat γ fibrinogen gene expression. *Blood* **96**, 3466–3472 (2000).
18. Albrecht, U. *et al.* Activation of NF-kappaB by IL-1beta blocks IL-6-induced

sustained STAT3 activation and STAT3-dependent gene expression of the human gamma-fibrinogen gene. *Cell. Signal.* **19**, 1866–1878 (2007).
19. Radtke, S. *et al.* Cross-regulation of cytokine signalling: pro-inflammatory cytokines restrict IL-6 signalling through receptor internalisation and degradation. *J. Cell Sci.* **123**, 947–959 (2010).
20. Woodward, R. N., Li, M. & Holland, L. J. Novel Accessory Factor-Binding Site Required for Glucocorticoid Regulation of the γ-Fibrinogen Subunit Gene from Xenopus laevis. *Mol. Endocrinol.* **11**, 563–576 (1997).
21. Roberts, L. R. & Holland, L. J. Coordinate transcriptional regulation of the three fibrinogen subunit genes by glucocorticoids in cultured primary liver cells from Xenopus laevis. *Endocrinology* **132**, 2563–2570 (1993).
22. Pindyck, J. *et al.* CONTROL OF FIBRINOGEN SYNTHESIS BY GLUCOCORTICOIDS IN THE ACUTE PHASE RESPONSE*. *Ann. N. Y. Acad. Sci.* **408**, 660–661 (1983).
23. Otto, J. M., Grenett, H. E. & Fuller, G. M. The coordinated regulation of fibrinogen gene transcription by hepatocyte-stimulating factor and dexamethasone. *J. Cell Biol.* **105**, 1067–1072 (1987).
24. Huber, P., Laurent, M. & Dalmon, J. Human beta-fibrinogen gene expression. Upstream sequences involved in its tissue specific expression and its dexamethasone and interleukin 6 stimulation. *J. Biol. Chem.* **265**, 5695–5701 (1990).
25. Dobson, D. A. *et al.* Novel genetic regulators of fibrinogen synthesis identified by an in vitro experimental platform. *J. Thromb. Haemost.* **21**, 522–533 (2023).
26. Arbustini, E., Narula, N. & D'Armini, A. M. Fibrinogen: A circulating factor in search of its genetic architecture. *Circulation* **128**, 1276–1280 (2013).
27. De Lange, M., Snieder, H., Ariëns, R. A. S., Spector, T. D. & Grant, P. J. The genetics of haemostasis: a twin study. *Lancet* **357**, 101–105 (2001).
28. May, J. E., Wolberg, A. S. & Lim, M. Y. Disorders of fibrinogen and fibrinolysis. *Hematol. Oncol. Clin. North Am.* **35**, 1197 (2021).
29. Hanss, M. & Biot, F. A Database for Human Fibrinogen Variants. *Ann. N. Y. Acad. Sci.* **936**, 89–90 (2001).
30. Sovova, Z., Pecankova, K., Majek, P. & Suttnar, J. Extension of the human fibrinogen database with detailed clinical information—The αc-connector segment. *Int. J. Mol. Sci.* **23**, 132 (2022).
31. Huffman, J. E. *et al.* Whole-genome analysis of plasma fibrinogen reveals population-differentiated genetic regulators with putative liver roles. *Blood* **144**, 2248–2265 (2024).
32. De Vries, P. S. *et al.* A meta-analysis of 120 246 individuals identifies 18 new loci for fibrinogen concentration. *Hum. Mol. Genet.* **25**, 358–370 (2016).
33. Hahn, J. *et al.* DNA methylation analysis is used to identify novel genetic loci associated with circulating fibrinogen levels in blood. *J. Thromb. Haemost.* **21**, 1135–1147 (2023).
34. Chaves De Souza, J. A. *et al.* SOCS3 Expression Correlates with Severity of Inflammation, Expression of Proinflammatory Cytokines, and Activation of STAT3 and p38 MAPK in LPS-Induced Inflammation In Vivo. *Mediators Inflamm.* **2013**, 650812 (2013).
35. Salloum-Asfar, S. *et al.* Regulation of coagulation factor XI expression by MicroRNAs in the human liver. *PLoS One* **9**, (2014).
36. Fort, A. *et al.* Regulation of fibrinogen production by microRNAs. *Blood* **116**, 2608–2615 (2010).

37. Brock, M. *et al.* MicroRNA-18a Enhances the Interleukin-6-mediated Production of the Acute-phase Proteins Fibrinogen and Haptoglobin in Human Hepatocytes. *J. Biol. Chem.* **286**, 40142–40150 (2011).
38. Grieninger, G. & Kimball, L. F. Contribution of the αEC Domain to the Structure and Function of Fibrinogen-420. *Ann. N. Y. Acad. Sci.* **936**, 44–64 (2001).
39. Mosesson, M. W. *et al.* The ultrastructure of fibrinogen-420 and the fibrin-420 clot. *Biophys. Chem.* **112**, 209–214 (2004).
40. Lishko, V. K., Yakubenko, V. P., Hertzberg, K. M., Grieninger, G. & Ugarova, T. P. The alternatively spliced αEC domain of human fibrinogen-420 is a novel ligand for leukocyte integrins αMβ2 and αXβ2. *Blood* **98**, 2448–2455 (2001).
41. Francis, C. W., Marder, V. J. & Martin, S. E. Demonstration of a large molecular weight variant of the gamma chain of normal human plasma fibrinogen. *J. Biol. Chem.* **255**, 5599–5604 (1980).
42. Chung, D. W. & Davie, E. W. γ and γ Chains of Human Fibrinogen Are Produced by Alternative mRNA Processing. *Biochemistry* **23**, 4232–4236 (1984).
43. Fornace, A. J., Cummings, D. E., Comeau, C. M., Kant, J. A. & Crabtree, G. R. Structure of the human gamma-fibrinogen gene. Alternate mRNA splicing near the 3' end of the gene produces gamma A and gamma B forms of gamma-fibrinogen. *J. Biol. Chem.* **259**, 12826–12830 (1984).
44. Wolfenstein-Todel, C. & Mosesson, M. W. Human plasma fibrinogen heterogeneity: evidence for an extended carboxyl-terminal sequence in a normal gamma chain variant (gamma'). *Proc. Natl. Acad. Sci. U. S. A.* **77**, 5069 (1980).
45. Rein-Smith, C. M., Anderson, N. W. & Farrell, D. H. Differential regulation of fibrinogen γ chain splice isoforms by interleukin-6. *Thromb. Res.* **131**, 89–93 (2013).
46. Pieters, M., Kotze, R. C., Jerling, J. C., Kruger, A. & Ariëns, R. A. S. Evidence that fibrinogen γ′ regulates plasma clot structure and lysis and relationship to cardiovascular risk factors in black Africans. *Blood* **121**, 3254–3260 (2013).
47. Huang, S., Cao, Z., Chung, D. W. & Davie, E. W. The role of betagamma and alphagamma complexes in the assembly of human fibrinogen. *J. Biol. Chem.* **271**, 27942–27947 (1996).
48. Redman, C. M. & Xia, H. Fibrinogen Biosynthesis. *Ann. N. Y. Acad. Sci.* **936**, 480–495 (2001).
49. Yu, S., Kong, V., Kudryk, B., Redman, C. & Kimball, L. F. Endogenous forms of fibrinogen in hep g2 cells. *Thromb. Res.* **46**, 281–293 (1987).
50. Danishefsky, K., Hartwig, R., Banerjee, D. & Redman, C. Intracellular fate of fibrinogen Bβ chain expressed in COS cells. *BBA - Gene Struct. Expr.* **1048**, 202–208 (1990).
51. Pieters, M. & Wolberg, A. S. Fibrinogen and fibrin: An illustrated review. *Res. Pract. Thromb. Haemost.* **3**, 161–172 (2019).
52. Yermolenko, I. S., Lishko, V. K., Ugarova, T. P. & Magonov, S. N. High-resolution visualization of fibrinogen molecules and fibrin fibers with atomic force microscopy. *Biomacromolecules* **12**, 370–379 (2011).
53. Litvinov, R. I. & Weisel, J. W. Shear strengthens fibrin: The knob-hole interactions display 'catch-slip' kinetics. *J. Thromb. Haemost.* **11**, 1933–1935 (2013).
54. Averett, L. E., Akhremitchev, B. B., Schoenfisch, M. H. & Gorkun, O. V. Calcium dependence of fibrin nanomechanics: the γ1 calcium mediates the unfolding of fibrinogen induced by force applied to the 'A-a' bond. *Langmuir* **26**, 14716–14722 (2010).

55. Weisel, J. W. & Litvinov, R. I. Mechanisms of fibrin polymerization and clinical implications. *Blood* **121**, 1712 (2013).
56. Tsurupa, G., Mahid, A., Veklich, Y., Weisel, J. W. & Medved, L. Structure, stability, and interaction of fibrin αC-domain polymers. *Biochemistry* **50**, 8028–8037 (2011).
57. Weisel, J. W. & Medved, L. The structure and function of the alpha C domains of fibrinogen. *Ann. N. Y. Acad. Sci.* **936**, 312–327 (2001).
58. Weisel, J. W. & Litvinov, R. I. Fibrin Formation, Structure and Properties. *Subcell. Biochem.* **82**, 405 (2017).
59. Mosesson, M., DiOrio, J., Siebenlist, K., Wall, J. & Hainfeld, J. Evidence for a Second Type of Fibril Branch Point in Fibrin Polymer Networks, the Trimolecular Junction. *Blood* **82**, 1517–1521 (1993).
60. Mosesson, M. W., Siebenlist, K. R., Amrani, D. L. & DiOrio, J. P. Identification of covalently linked trimeric and tetrameric D domains in crosslinked fibrin. *Proc. Natl. Acad. Sci. U. S. A.* **86**, 1113–1117 (1989).
61. Tanaka, K. A., Key, N. S. & Levy, J. H. Blood coagulation: Hemostasis and thrombin regulation. *Anesth. Analg.* **108**, 1433–1446 (2009).
62. Houser, J. R. *et al.* Evidence that αC Region Is Origin of Low Modulus, High Extensibility, and Strain Stiffening in Fibrin Fibers. *Biophys. J.* **99**, 3038 (2010).
63. Lorand, L. Factor XIII: Structure, Activation, and Interactions with Fibrinogen and Fibrin. *Ann. N. Y. Acad. Sci.* **936**, 291–311 (2001).
64. Kurniawan, N. A., Grimbergen, J., Koopman, J. & Koenderink, G. H. Factor XIII stiffens fibrin clots by causing fiber compaction. *J. Thromb. Haemost.* **12**, 1687–1696 (2014).
65. Carlisle, C. R., Sparks, E. A., Der loughian, C. & Guthold, M. Strength and failure of fibrin fiber branchpoints. *J. Thromb. Haemost.* **8**, 1135–1138 (2010).
66. Helms, C. C., Ariëns, R. A. S., Uitte De Willige, S., Standeven, K. F. & Guthold, M. α−α Cross-Links Increase Fibrin Fiber Elasticity and Stiffness. *Biophys. J.* **102**, 168–175 (2012).
67. Weisel, J. W. Structure of fibrin: impact on clot stability. *J. Thromb. Haemost.* **5 Suppl 1**, 116–124 (2007).
68. Hoylaerts, M., Rijken, D. C., Lijnen, H. R. & Collen, D. Kinetics of the activation of plasminogen by human tissue plasminogen activator. Role of fibrin. *J. Biol. Chem.* **257**, 2912–2919 (1982).
69. Longstaff, C. & Kolev, K. Basic mechanisms and regulation of fibrinolysis. *J. Thromb. Haemost.* **13**, S98–S105 (2015).
70. Collet, J. P. *et al.* Influence of fibrin network conformation and fibrin fiber diameter on fibrinolysis speed: dynamic and structural approaches by confocal microscopy. *Arterioscler. Thromb. Vasc. Biol.* **20**, 1354–1361 (2000).
71. Blinc, A., Magdič, J. & Fric, J. Atomic force microscopy of fibrin networks and plasma clots during fibrinolysis. *Fibrinolysis and Proteolysis* **14**, 288–299 (2000).
72. Bannish, B. E., Chernysh, I. N., Keener, J. P., Fogelson, A. L. & Weisel, J. W. Molecular and Physical Mechanisms of Fibrinolysis and Thrombolysis from Mathematical Modeling and Experiments. *Sci. Reports 2017 71* **7**, 1–11 (2017).
73. Lynch, S. R., Laverty, S. M., Bannish, B. E. & Hudson, N. E. Microscale Structural Changes of Individual Fibrin Fibers During Fibrinolysis. *Acta Biomater.* **141**, 114 (2022).
74. Ouedraogo, R. R., Sowers, H. K., Lynch, S. R., Hudson, N. E. & Bannish, B. E. A mathematical model of plasmin-mediated fibrinolysis of single fibrin fibers. *PLOS Comput. Biol.* **20**, e1012684 (2024).

75. Chapin, J. C. & Hajjar, K. A. Fibrinolysis and the control of blood coagulation. *Blood Rev.* **29**, 17 (2014).
76. Domingues, M. M. *et al.* Thrombin and fibrinogen γ′ impact clot structure by marked effects on intrafibrillar structure and protofibril packing. *Blood* **127**, 487–495 (2016).
77. Wolberg, A. S. Thrombin generation and fibrin clot structure. *Blood Rev.* **21**, 131–142 (2007).
78. Ugarova, T. P. *et al.* Sequence gamma 377-395(P2), but not gamma 190-202(P1), is the binding site for the alpha MI-domain of integrin alpha M beta 2 in the gamma C-domain of fibrinogen. *Biochemistry* **42**, 9365–9373 (2003).
79. Lishko, V. K., Kudryk, B., Yakubenko, V. P., Yee, V. C. & Ugarova, T. P. Regulated unmasking of the cryptic binding site for integrin alpha M beta 2 in the gamma C-domain of fibrinogen. *Biochemistry* **41**, 12942–12951 (2002).
80. Smiley, S. T., King, J. A. & Hancock, W. W. Fibrinogen Stimulates Macrophage Chemokine Secretion Through Toll-Like Receptor 4. *J. Immunol.* **167**, 2887–2894 (2001).
81. Kuhns, D. B., Priel, D. A. L. & Gallin, J. I. Induction of human monocyte interleukin (IL)-8 by fibrinogen through the toll-like receptor pathway. *Inflammation* **30**, 178–188 (2007).
82. Sitrin, R. G., Pan, P. M., Srikanth, S. & Todd III, R. F. Fibrinogen Activates NF-κB Transcription Factors in Mononuclear Phagocytes. *J. Immunol.* **161**, 1462–1470 (1998).
83. Rubel, C. *et al.* Fibrinogen Promotes Neutrophil Activation and Delays Apoptosis. *J. Immunol.* **166**, 2002–2010 (2001).
84. Kuijper, P. H. M. *et al.* Neutrophil Adhesion to Fibrinogen and Fibrin Under Flow Conditions Is Diminished by Activation and L-Selectin Shedding. *Blood* **89**, 2131–2138 (1997).
85. Coden, M. E. *et al.* Fibrinogen is a specific trigger for cytolytic eosinophil degranulation. *J. Immunol.* **204**, 438 (2019).
86. Languino, L. R. *et al.* Fibrinogen mediates leukocyte adhesion to vascular endothelium through an ICAM-1-dependent pathway. *Cell* **73**, 1423–1434 (1993).
87. Kobelt, G., Thompson, A., Berg, J., Gannedahl, M. & Eriksson, J. New insights into the burden and costs of multiple sclerosis in Europe. *Mult. Scler.* **23**, 1123–1136 (2017).
88. Jakimovski, D. *et al.* Multiple sclerosis. *Lancet* **403**, 183–202 (2024).
89. Yeshokumar, A. K., Narula, S. & Banwell, B. Pediatric multiple sclerosis. *Curr. Opin. Neurol.* **30**, 216–221 (2017).
90. Thompson, A. J. *et al.* Diagnosis of multiple sclerosis: 2017 revisions of the McDonald criteria. *Lancet Neurol.* **17**, 162–173 (2018).
91. Scalfari, A. *et al.* The natural history of multiple sclerosis: a geographically based study 10: relapses and long-term disability. *Brain* **133**, 1914–1929 (2010).
92. Scalfari, A. *et al.* Early Relapses, Onset of Progression, and Late Outcome in Multiple Sclerosis. *JAMA Neurol.* **70**, 214–222 (2013).
93. Cree, B. A. C. *et al.* Silent progression in disease activity–free relapsing multiple sclerosis. *Ann. Neurol.* **85**, 653 (2019).
94. Tur, C. *et al.* Association of Early Progression Independent of Relapse Activity With Long-term Disability After a First Demyelinating Event in Multiple Sclerosis. *JAMA Neurol.* **80**, 151 (2022).
95. Rocca, M. A. *et al.* Spinal cord lesions and brain grey matter atrophy

independently predict clinical worsening in definite multiple sclerosis: a 5-year, multicentre study. *J. Neurol. Neurosurg. Psychiatry* **94**, 10–18 (2023).
96. Miller, D. H. & Leary, S. M. Primary-progressive multiple sclerosis. *Lancet Neurol.* **6**, 903–912 (2007).
97. Braune, S. *et al.* The natural history of primary progressive multiple sclerosis: insights from the German NeuroTransData registry. *BMC Neurol.* **23**, 1–12 (2023).
98. Lunde, H. M. B., Assmus, J., Myhr, K. M., Bø, L. & Grytten, N. Survival and cause of death in multiple sclerosis: a 60-year longitudinal population study. *J. Neurol. Neurosurg. Psychiatry* **88**, 621–625 (2017).
99. Leray, E. *et al.* Excess Mortality in Patients with Multiple Sclerosis Starts at 20 Years from Clinical Onset: Data from a Large-Scale French Observational Study. *PLoS One* **10**, e0132033 (2015).
100. Steinmetz, J. D. *et al.* Global, regional, and national burden of disorders affecting the nervous system, 1990–2021: a systematic analysis for the Global Burden of Disease Study 2021. *Lancet Neurol.* **23**, 344–381 (2024).
101. Amato, M. P. *et al.* Disease-modifying drugs can reduce disability progression in relapsing multiple sclerosis. *Brain* **143**, 3013–3024 (2020).
102. Rae-Grant, A. *et al.* Comprehensive systematic review summary: Disease-modifying therapies for adults with multiple sclerosis. *Neurology* **90**, 789–800 (2018).
103. Flemmen, H. Ø. *et al.* Prevalence of multiple sclerosis in rural and urban districts in Telemark county, Norway. *Mult. Scler. Relat. Disord.* **45**, 102352 (2020).
104. Wallin, M. T. *et al.* Global, regional, and national burden of multiple sclerosis 1990–2016: a systematic analysis for the Global Burden of Disease Study 2016. *Lancet Neurol.* **18**, 269–285 (2019).
105. Pearson, J. F. *et al.* Multiple sclerosis in New Zealand Māori. *Mult. Scler.* **20**, 1892–1895 (2014).
106. Taylor, B. V. *et al.* MS prevalence in New Zealand, an ethnically and latitudinally diverse country. *Mult. Scler.* **16**, 1422–1431 (2010).
107. Houzen, H., Kano, T., Kondo, K., Takahashi, T. & Niino, M. The prevalence and incidence of multiple sclerosis over the past 20 years in northern Japan. *Mult. Scler. Relat. Disord.* **73**, 104696 (2023).
108. Haak, W. *et al.* Massive migration from the steppe was a source for Indo-European languages in Europe. *Nat. 2015 5227555* **522**, 207–211 (2015).
109. Barrie, W. *et al.* Elevated genetic risk for multiple sclerosis emerged in steppe pastoralist populations. *Nat. 2024 6257994* **625**, 321–328 (2024).
110. Tian, C. *et al.* Genome-wide association and HLA region fine-mapping studies identify susceptibility loci for multiple common infections. *Nat. Commun. 2017 81* **8**, 1–13 (2017).
111. Simpson, S. *et al.* Latitude continues to be significantly associated with the prevalence of multiple sclerosis: an updated meta-analysis. *J. Neurol. Neurosurg. Psychiatry* **90**, 1193–1200 (2019).
112. Tao, C. *et al.* Higher latitude is significantly associated with an earlier age of disease onset in multiple sclerosis. *J. Neurol. Neurosurg. Psychiatry* **87**, 1343–1349 (2016).
113. Koch-Henriksen, N., Thygesen, L. C., Stenager, E., Laursen, B. & Magyari, M. Incidence of MS has increased markedly over six decades in Denmark particularly with late onset and in women. *Neurology* **90**, e1954–e1963 (2018).
114. Orton, S. M. *et al.* Sex ratio of multiple sclerosis in Canada: a longitudinal study.

Lancet. Neurol. **5**, 932–936 (2006).
115. Kotzamani, D. *et al.* Rising incidence of multiple sclerosis in females associated with urbanization. *Neurology* **78**, 1728–1735 (2012).
116. Rotstein, D. L. *et al.* Temporal trends in multiple sclerosis prevalence and incidence in a large population. *Neurology* **90**, E1435–E1441 (2018).
117. Grytten, N., Aarseth, J. H., Lunde, H. M. B. & Myhr, K. M. A 60-year follow-up of the incidence and prevalence of multiple sclerosis in Hordaland County, Western Norway. *J. Neurol. Neurosurg. Psychiatry* **87**, 100 (2015).
118. Trojano, M. *et al.* Geographical Variations in Sex Ratio Trends over Time in Multiple Sclerosis. *PLoS One* **7**, e48078 (2012).
119. Koch-Henriksen, N. & Sørensen, P. S. The changing demographic pattern of multiple sclerosis epidemiology. *Lancet Neurol.* **9**, 520–532 (2010).
120. Olsson, T., Barcellos, L. F. & Alfredsson, L. Interactions between genetic, lifestyle and environmental risk factors for multiple sclerosis. *Nat. Rev. Neurol. 2017 131* **13**, 25–36 (2016).
121. Bjornevik, K. *et al.* Longitudinal analysis reveals high prevalence of Epstein-Barr virus associated with multiple sclerosis. *Science (80-.).* **375**, 296–301 (2022).
122. Lanz, T. V. *et al.* Clonally expanded B cells in multiple sclerosis bind EBV EBNA1 and GlialCAM. *Nat. 2022 6037900* **603**, 321–327 (2022).
123. Tengvall, K. *et al.* Molecular mimicry between Anoctamin 2 and Epstein-Barr virus nuclear antigen 1 associates with multiple sclerosis risk. *Proc. Natl. Acad. Sci. U. S. A.* **116**, 16955–16960 (2019).
124. Lindsey, J. W. Antibodies to the Epstein-Barr virus proteins BFRF3 and BRRF2 cross-react with human proteins. *J. Neuroimmunol.* **310**, 131–134 (2017).
125. Munger, K. L., Levin, L. I., Hollis, B. W., Howard, N. S. & Ascherio, A. Serum 25-hydroxyvitamin D levels and risk of multiple sclerosis. *JAMA* **296**, 2832–2838 (2006).
126. Sandberg, L. *et al.* Vitamin D and axonal injury in multiple sclerosis. *Mult. Scler.* **22**, 1027–1031 (2016).
127. Tremlett, H., Zhu, F., Ascherio, A. & Munger, K. L. Sun exposure over the life course and associations with multiple sclerosis. *Neurology* **90**, E1191–E1199 (2018).
128. Adzemovic, M. Z., Zeitelhofer, M., Hochmeister, S., Gustafsson, S. A. & Jagodic, M. Efficacy of vitamin D in treating multiple sclerosis-like neuroinflammation depends on developmental stage. *Exp. Neurol.* **249**, 39–48 (2013).
129. Lucas, R. M., Byrne, S. N., Correale, J., Ilschner, S. & Hart, P. H. Ultraviolet Radiation, Vitamin D and Multiple Sclerosis. *Neurodegener. Dis. Manag.* **5**, 413–424 (2015).
130. Ghadirian, P., Dadgostar, B., Azani, R. & Maisonneuve, P. A case-control study of the association between socio-demographic, lifestyle and medical history factors and multiple sclerosis. *Can. J. Public Health* **92**, 281–285 (2001).
131. Hedström, A. K., Bäärnhielm, M., Olsson, T. & Alfredsson, L. Tobacco smoking, but not Swedish snuff use, increases the risk of multiple sclerosis. *Neurology* **73**, 696–701 (2009).
132. Hedström, A. K., Bäärnhielm, M., Olsson, T. & Alfredsson, L. Exposure to environmental tobacco smoke is associated with increased risk for multiple sclerosis. *Mult. Scler.* **17**, 788–793 (2011).
133. Hedström, A. K., Hillert, J., Olsson, T. & Alfredsson, L. Nicotine might have a protective effect in the etiology of multiple sclerosis. *Mult. Scler.* **19**, 1009–1013 (2013).

134. Mazzone, P. *et al.* Pathophysiological Impact of Cigarette Smoke Exposure on the Cerebrovascular System with a Focus on the Blood-brain Barrier: Expanding the Awareness of Smoking Toxicity in an Underappreciated Area. *Int. J. Environ. Res. Public Health* **7**, 4111 (2010).
135. Liu, Y. *et al.* Association of Cigarette Smoking With Cerebrospinal Fluid Biomarkers of Neurodegeneration, Neuroinflammation, and Oxidation. *JAMA Netw. Open* **3**, e2018777–e2018777 (2020).
136. Gons, R. A. R. *et al.* Cigarette smoking is associated with reduced microstructural integrity of cerebral white matter. *Brain* **134**, 2116–2124 (2011).
137. Munger, K. L., Chitnis, T. & Ascherio, A. Body size and risk of MS in two cohorts of US women. *Neurology* **73**, 1543–1550 (2009).
138. Wesnes, K. *et al.* Body size and the risk of multiple sclerosis in Norway and Italy: the EnvIMS study. *Mult. Scler.* **21**, 388–395 (2015).
139. Huppke, B. *et al.* Association of Obesity With Multiple Sclerosis Risk and Response to First-line Disease Modifying Drugs in Children. *JAMA Neurol.* **76**, 1157–1165 (2019).
140. Hedström, A. K. *et al.* Interaction between adolescent obesity and HLA risk genes in the etiology of multiple sclerosis. *Neurology* **82**, 865 (2014).
141. Gianfrancesco, M. A. *et al.* Obesity during childhood and adolescence increases susceptibility to multiple sclerosis after accounting for established genetic and environmental risk factors. *Obes. Res. Clin. Pract.* **8**, e435–e447 (2014).
142. Mokry, L. E. *et al.* Obesity and Multiple Sclerosis: A Mendelian Randomization Study. *PLoS Med.* **13**, (2016).
143. Guillemot-Legris, O. & Muccioli, G. G. Obesity-Induced Neuroinflammation: Beyond the Hypothalamus. *Trends Neurosci.* **40**, 237–253 (2017).
144. Miller, A. A. & Spencer, S. J. Obesity and neuroinflammation: a pathway to cognitive impairment. *Brain. Behav. Immun.* **42**, 10–21 (2014).
145. Schmitt, L. O. & Gaspar, J. M. Obesity-Induced Brain Neuroinflammatory and Mitochondrial Changes. *Metabolites* **13**, 86 (2023).
146. Goris, A., Vandebergh, M., McCauley, J. L., Saarela, J. & Cotsapas, C. Genetics of multiple sclerosis: lessons from polygenicity. *Lancet Neurol.* **21**, 830–842 (2022).
147. Patsopoulos, N. A. *et al.* Multiple Sclerosis Genomic Map implicates peripheral immune cells & microglia in susceptibility. *Science* **365**, 50 (2019).
148. Westerlind, H. *et al.* Modest familial risks for multiple sclerosis: a registry-based study of the population of Sweden. *Brain* **137**, 770–778 (2014).
149. Moutsianas, L. *et al.* Class II HLA interactions modulate genetic risk for multiple sclerosis. *Nat. Genet.* **47**, 1107 (2015).
150. Brownlee, W. J. *et al.* HLA-DRB1*1501 influences long-term disability progression and tissue damage on MRI in relapse-onset multiple sclerosis. *Mult. Scler.* **29**, 333–342 (2023).
151. Isobe, N. *et al.* Association of HLA Genetic Risk Burden With Disease Phenotypes in Multiple Sclerosis. *JAMA Neurol.* **73**, 795–802 (2016).
152. Hedström, A. K. *et al.* DRB1–environment interactions in multiple sclerosis etiology: results from two Swedish case–control studies. *J. Neurol. Neurosurg. Psychiatry* **92**, 717–722 (2021).
153. Barkhof, F. *et al.* Onset of clinical and MRI efficacy of ocrelizumab in relapsing multiple sclerosis. *Neurology* **93**, e1778 (2019).
154. Havrdová, E. *et al.* No evidence of disease activity (NEDA) analysis by epochs in patients with relapsing multiple sclerosis treated with ocrelizumab vs interferon

beta-1a. *Mult. Scler. J. - Exp. Transl. Clin.* **4**, 1–11 (2018).
155. Wolinsky, J. S. *et al.* Long-term follow-up from the ORATORIO trial of ocrelizumab for primary progressive multiple sclerosis: a post-hoc analysis from the ongoing open-label extension of the randomised, placebo-controlled, phase 3 trial. *Lancet. Neurol.* **19**, 998–1009 (2020).
156. Lamb, Y. N. Ocrelizumab: A Review in Multiple Sclerosis. *Drugs* **82**, 323–334 (2022).
157. Bar-Or, A. *et al.* Rituximab in relapsing-remitting multiple sclerosis: a 72-week, open-label, phase I trial. *Ann. Neurol.* **63**, 395–400 (2008).
158. Hauser, S. L. *et al.* B-cell depletion with rituximab in relapsing-remitting multiple sclerosis. *N. Engl. J. Med.* **358**, 676–688 (2008).
159. Von Büdingen, H. C. *et al.* B cell exchange across the blood-brain barrier in multiple sclerosis. *J. Clin. Invest.* **122**, 4533–4543 (2012).
160. Palanichamy, A. *et al.* Immunoglobulin class-switched B cells form an active immune axis between CNS and periphery in multiple sclerosis. *Sci. Transl. Med.* **6**, (2014).
161. Stern, J. N. H. *et al.* B cells populating the multiple sclerosis brain mature in the draining cervical lymph nodes. *Sci. Transl. Med.* **6**, (2014).
162. Louveau, A. *et al.* Structural and functional features of central nervous system lymphatic vessels. *Nature* **523**, 337–341 (2015).
163. Absinta, M. *et al.* Human and nonhuman primate meninges harbor lymphatic vessels that can be visualized noninvasively by MRI. *Elife* **6**, (2017).
164. Licastro, E. *et al.* Glymphatic and lymphatic communication with systemic responses during physiological and pathological conditions in the central nervous system. *Commun. Biol. 2024 71* **7**, 1–9 (2024).
165. Molnarfi, N. *et al.* MHC class II–dependent B cell APC function is required for induction of CNS autoimmunity independent of myelin-specific antibodies. *J. Exp. Med.* **210**, 2921–2937 (2013).
166. Wang, J. *et al.* HLA-DR15 Molecules Jointly Shape an Autoreactive T Cell Repertoire in Multiple Sclerosis. *Cell* **183**, 1264 (2020).
167. Serafini, B., Rosicarelli, B., Magliozzi, R., Stigliano, E. & Aloisi, F. Detection of Ectopic B-cell Follicles with Germinal Centers in the Meninges of Patients with Secondary Progressive Multiple Sclerosis. *Brain Pathol.* **14**, 164–174 (2004).
168. Magliozzi, R. *et al.* Meningeal B-cell follicles in secondary progressive multiple sclerosis associate with early onset of disease and severe cortical pathology. *Brain* **130**, 1089–1104 (2007).
169. Magliozzi, R. *et al.* A Gradient of neuronal loss and meningeal inflammation in multiple sclerosis. *Ann. Neurol.* **68**, 477–493 (2010).
170. Haugen, M., Frederiksen, J. L. & Degn, M. B cell follicle-like structures in multiple sclerosis—With focus on the role of B cell activating factor. *J. Neuroimmunol.* **273**, 1–7 (2014).
171. Diddens, J. *et al.* Single-Cell Profiling Indicates a Proinflammatory Role of Meningeal Ectopic Lymphoid Tissue in Experimental Autoimmune Encephalomyelitis. *Neurol. Neuroimmunol. neuroinflammation* **11**, e200185 (2024).
172. Baecher-Allan, C., Kaskow, B. J. & Weiner, H. L. Multiple Sclerosis: Mechanisms and Immunotherapy. *Neuron* **97**, 742–768 (2018).
173. Filippi, M. *et al.* Multiple sclerosis. *Nat. Rev. Dis. Prim. 2018 41* **4**, 1–27 (2018).
174. Lassmann, H., Brück, W. & Lucchinetti, C. F. The immunopathology of multiple sclerosis: an overview. *Brain Pathol.* **17**, 210–218 (2007).

175. Lassmann, H. Pathology and disease mechanisms in different stages of multiple sclerosis. *J. Neurol. Sci.* **333**, 1–4 (2013).
176. Lassmann, H. Multiple Sclerosis Pathology. *Cold Spring Harb. Perspect. Med.* **8**, a028936 (2018).
177. Lassmann, H. Pathogenic mechanisms associated with different clinical courses of multiple sclerosis. *Front. Immunol.* **10**, 428340 (2019).
178. Lassmann, H. The contribution of neuropathology to multiple sclerosis research. *Eur. J. Neurol.* **29**, 2869 (2022).
179. Grajchen, E., Hendriks, J. J. A. & Bogie, J. F. J. The physiology of foamy phagocytes in multiple sclerosis. *Acta Neuropathol. Commun. 2018 61* **6**, 1–21 (2018).
180. Fischer, M. T. *et al.* NADPH oxidase expression in active multiple sclerosis lesions in relation to oxidative tissue damage and mitochondrial injury. *Brain* **135**, 886 (2012).
181. Fawcett, J. W. & Asher, R. A. The glial scar and central nervous system repair. *Brain Res. Bull.* **49**, 377–391 (1999).
182. Kornek, B. *et al.* Multiple sclerosis and chronic autoimmune encephalomyelitis: a comparative quantitative study of axonal injury in active, inactive, and remyelinated lesions. *Am. J. Pathol.* **157**, 267–276 (2000).
183. Luchetti, S. *et al.* Progressive multiple sclerosis patients show substantial lesion activity that correlates with clinical disease severity and sex: a retrospective autopsy cohort analysis. *Acta Neuropathol.* **135**, 511 (2018).
184. Patrikios, P. *et al.* Remyelination is extensive in a subset of multiple sclerosis patients. *Brain* **129**, 3165–3172 (2006).
185. Kirk, J., Plumb, J., Mirakhur, M. & McQuaid, S. Tight junctional abnormality in multiple sclerosis white matter affects all calibres of vessel and is associated with blood–brain barrier leakage and active demyelination. *J. Pathol.* **201**, 319–327 (2003).
186. Plumb, J., McQuaid, S., Mirakhur, M. & Kirk, J. Abnormal endothelial tight junctions in active lesions and normal-appearing white matter in multiple sclerosis. *Brain Pathol.* **12**, 154–169 (2002).
187. Padden, M. *et al.* Differences in expression of junctional adhesion molecule-A and β-catenin in multiple sclerosis brain tissue: Increasing evidence for the role of tight junction pathology. *Acta Neuropathol.* **113**, 177–186 (2007).
188. Leech, S., Kirk, J., Plumb, J. & McQuaid, S. Persistent endothelial abnormalities and blood–brain barrier leak in primary and secondary progressive multiple sclerosis. *Neuropathol. Appl. Neurobiol.* **33**, 86–98 (2007).
189. Uchida, Y. *et al.* Involvement of Claudin-11 in Disruption of Blood-Brain, -Spinal Cord, and -Arachnoid Barriers in Multiple Sclerosis. *Mol. Neurobiol.* **56**, 2039–2056 (2019).
190. Vos, C. M. P. *et al.* Blood–brain barrier alterations in both focal and diffuse abnormalities on postmortem MRI in multiple sclerosis. *Neurobiol. Dis.* **20**, 953–960 (2005).
191. Yates, R. L. *et al.* Fibrin(ogen) and neurodegeneration in the progressive multiple sclerosis cortex. *Ann. Neurol.* **82**, 259–270 (2017).
192. Kermode, A. G. *et al.* BREAKDOWN OF THE BLOOD-BRAIN BARRIER PRECEDES SYMPTOMS AND OTHER MRI SIGNS OF NEW LESIONS IN MULTIPLE SCLEROSIS: PATHOGENETIC AND CLINICAL IMPLICATIONS. *Brain* **113**, 1477–1489 (1990).
193. Stone, L. A. *et al.* Blood-brain barrier disruption on contrast-enhanced MRI in

patients with mild relapsing-remitting multiple sclerosis: relationship to course, gender, and age. *Neurology* **45**, 1122–1126 (1995).
194. Zierfuss, B., Larochelle, C. & Prat, A. Blood–brain barrier dysfunction in multiple sclerosis: causes, consequences, and potential effects of therapies. *Lancet Neurol.* **23**, 95–109 (2024).
195. Petersen, M. A., Ryu, J. K. & Akassoglou, K. Fibrinogen in neurological diseases: Mechanisms, imaging and therapeutics. *Nature Reviews Neuroscience* vol. 19 283–301 (2018).
196. Sweeney, M. D., Sagare, A. P. & Zlokovic, B. V. Blood–brain barrier breakdown in Alzheimer disease and other neurodegenerative disorders. *Nat. Rev. Neurol. 2018 143* **14**, 133–150 (2018).
197. Lee, N. J. *et al.* Spatiotemporal distribution of fibrinogen in marmoset and human inflammatory demyelination. *Brain* **141**, 1637 (2018).
198. Davalos, D. *et al.* Fibrinogen-induced perivascular microglial clustering is required for the development of axonal damage in neuroinflammation. *Nat. Commun. 2012 31* **3**, 1–15 (2012).
199. Ahn, H. J., Chen, Z. L., Zamolodchikov, D., Norris, E. H. & Strickland, S. Interactions of β-Amyloid Peptide with Fibrinogen and Coagulation Factor XII may contribute to Alzheimer's Disease. *Curr. Opin. Hematol.* **24**, 427 (2017).
200. Hultman, K., Strickland, S. & Norris, E. H. The APOE ε4/ε4 genotype potentiates vascular fibrin(ogen) deposition in amyloid-laden vessels in the brains of Alzheimer's disease patients. *J. Cereb. Blood Flow Metab.* **33**, 1251–1258 (2013).
201. Ryu, J. K. & McLarnon, J. G. A leaky blood–brain barrier, fibrinogen infiltration and microglial reactivity in inflamed Alzheimer's disease brain. *J. Cell. Mol. Med.* **13**, 2911–2925 (2009).
202. Merlini, M. *et al.* Fibrinogen Induces Microglia-Mediated Spine Elimination and Cognitive Impairment in an Alzheimer's Disease Model. *Neuron* **101**, 1099-1108.e6 (2019).
203. Knox, E. G., Aburto, M. R., Clarke, G., Cryan, J. F. & O'Driscoll, C. M. The blood-brain barrier in aging and neurodegeneration. *Mol. Psychiatry 2022 276* **27**, 2659–2673 (2022).
204. McAleese, K. E. *et al.* Extravascular fibrinogen in the white matter of Alzheimer's disease and normal aged brains: implications for fibrinogen as a biomarker for Alzheimer's disease. *Brain Pathol.* **29**, 414–424 (2019).
205. Alruwaili, M. *et al.* Pathogenic Role of Fibrinogen in the Neuropathology of Multiple Sclerosis: A Tale of Sorrows and Fears. *Neurochem. Res. 2023 4811* **48**, 3255–3269 (2023).
206. Distéfano-Gagné, F., Bitarafan, S., Lacroix, S. & Gosselin, D. Roles and regulation of microglia activity in multiple sclerosis: insights from animal models. *Nat. Rev. Neurosci. 2023 247* **24**, 397–415 (2023).
207. Ponath, G., Park, C. & Pitt, D. The Role of Astrocytes in Multiple Sclerosis. *Front. Immunol.* **9**, 217 (2018).
208. Woo, M. S., Engler, J. B. & Friese, M. A. The neuropathobiology of multiple sclerosis. *Nat. Rev. Neurosci. 2024 257* **25**, 493–513 (2024).
209. Bankhead, P. *et al.* QuPath: Open source software for digital pathology image analysis. *Sci. Reports 2017 71* **7**, 1–7 (2017).
210. Prince. https://maxhalford.github.io/prince/.
211. Løberg, E. M. & Torvik, A. Uptake of plasma proteins into damaged neurons - An experimental study on cryogenic lesions in rats. *Acta Neuropathol.* **81**, 479–

485 (1991).
212. Johnson, V. E. *et al.* Mechanical disruption of the blood–brain barrier following experimental concussion. *Acta Neuropathol.* **135**, 711–726 (2018).
213. Liu, J. Y. W. *et al.* Neuropathology of the blood–brain barrier and pharmaco-resistance in human epilepsy. *Brain* **135**, 3115–3133 (2012).
214. Tomimoto, H. *et al.* Alterations of the blood-brain barrier and glial cells in white-matter lesions in cerebrovascular and Alzheimer's disease patients. *Stroke* **27**, 2069–2074 (1996).
215. Simpson, J. E. *et al.* White matter lesions in an unselected cohort of the elderly: astrocytic, microglial and oligodendrocyte precursor cell responses. *Neuropathol. Appl. Neurobiol.* **33**, 410–419 (2007).
216. Roseborough, A. D. *et al.* Microvessel stenosis, enlarged perivascular spaces, and fibrinogen deposition are associated with ischemic periventricular white matter hyperintensities. *Brain Pathol.* **32**, e13017 (2022).
217. Bridges, L. R. *et al.* Blood-Brain Barrier Dysfunction and Cerebral Small Vessel Disease (Arteriolosclerosis) in Brains of Older People. *J. Neuropathol. Exp. Neurol.* **73**, 1026 (2014).
218. Viggars, A. P. *et al.* Alterations in the blood brain barrier in ageing cerebral cortex in relationship to Alzheimer-type pathology: A study in the MRC-CFAS population neuropathology cohort. *Neurosci. Lett.* **505**, 25–30 (2011).
219. Brown, H. *et al.* Evidence of blood-brain barrier dysfunction in human cerebral malaria. *Neuropathol. Appl. Neurobiol.* **25**, 331–340 (1999).
220. Haas, J. *et al.* LRP1b shows restricted expression in human tissues and binds to several extracellular ligands, including fibrinogen and apoE – carrying lipoproteins. *Atherosclerosis* **216**, 342–347 (2011).
221. Gao, D. L. & Johal, M. S. LRP-1 Binds Fibrinogen in a Sialylation-Dependent Manner: A Quartz Crystal Microbalance Study. *Langmuir* **39**, 10375–10382 (2023).
222. Kanekiyo, T. *et al.* Neuronal Clearance of Amyloid-β by Endocytic Receptor LRP1. *J. Neurosci.* **33**, 19276–19283 (2013).
223. Liu, C. C. *et al.* Astrocytic LRP1 Mediates Brain Aβ Clearance and Impacts Amyloid Deposition. *J. Neurosci.* **37**, 4023 (2017).
224. Chen, K. *et al.* LRP1 is a neuronal receptor for α-synuclein uptake and spread. *Mol. Neurodegener.* **17**, 1–14 (2022).
225. Shinohara, M., Tachibana, M., Kanekiyo, T. & Bu, G. Role of LRP1 in the pathogenesis of Alzheimer's disease: evidence from clinical and preclinical studies: Thematic Review Series: ApoE and Lipid Homeostasis in Alzheimer's Disease. *J. Lipid Res.* **58**, 1267–1281 (2017).
226. Lin, J. P., Mironova, Y. A., Shrager, P. & Giger, R. J. LRP1 regulates peroxisome biogenesis and cholesterol homeostasis in oligodendrocytes and is required for proper CNS myelin development and repair. *Elife* **6**, (2017).
227. Auderset, L., Cullen, C. L. & Young, K. M. Low Density Lipoprotein-Receptor Related Protein 1 Is Differentially Expressed by Neuronal and Glial Populations in the Developing and Mature Mouse Central Nervous System. *PLoS One* **11**, e0155878 (2016).
228. Fernández-Castañeda, A. *et al.* The active contribution of OPCs to neuroinflammation is mediated by LRP1. *Acta Neuropathol.* **139**, 365 (2019).
229. Adams, D. L., Piserchia, V., Economides, J. R. & Horton, J. C. Vascular Supply of the Cerebral Cortex is Specialized for Cell Layers but Not Columns. *Cereb. Cortex (New York, NY)* **25**, 3673 (2014).

230. Schmid, F., Barrett, M. J. P., Jenny, P. & Weber, B. Vascular density and distribution in neocortex. *Neuroimage* **197**, 792–805 (2019).
231. Zierfuss, B., Larochelle, C. & Prat, A. Blood–brain barrier dysfunction in multiple sclerosis: causes, consequences, and potential effects of therapies. *Lancet Neurol.* **23**, 95–109 (2024).
232. Banks, W. A., Reed, M. J., Logsdon, A. F., Rhea, E. M. & Erickson, M. A. Healthy aging and the blood-brain barrier. *Nat. aging* **1**, 243 (2021).
233. Petersen, M. A., Ryu, J. K. & Akassoglou, K. Fibrinogen in neurological diseases: mechanisms, imaging and therapeutics. *Nat. Rev. Neurosci. 2018 195* **19**, 283–301 (2018).
234. Cortes-Canteli, M. *et al.* Fibrinogen and β-amyloid association alters thrombosis and fibrinolysis: a possible contributing factor to Alzheimer's disease. *Neuron* **66**, 695 (2010).
235. Singh, P. K. *et al.* Lecanemab blocks the effects of the Aβ/fibrinogen complex on blood clots and synapse toxicity in organotypic culture. *Proc. Natl. Acad. Sci. U. S. A.* **121**, e2314450121 (2024).
236. Dean, T. *et al.* Fibrin promotes oxidative stress and neuronal loss in traumatic brain injury via innate immune activation. *J. Neuroinflammation* **21**, 1–12 (2024).
237. Sulimai, N., Brown, J. & Lominadze, D. The effects of fibrinogen's interactions with its neuronal receptors, intercellular adhesion molecule-1 and cellular prion protein. *Biomolecules* **11**, 1381 (2021).
238. Lishko, V. K. *et al.* Multiple binding sites in fibrinogen for integrin αMβ 2 (Mac-1). *J. Biol. Chem.* **279**, 44897–44906 (2004).
239. Adams, R. A. *et al.* The fibrin-derived gamma377-395 peptide inhibits microglia activation and suppresses relapsing paralysis in central nervous system autoimmune disease. *J. Exp. Med.* **204**, 571–582 (2007).
240. Sielaff, M. *et al.* Evaluation of FASP, SP3, and iST Protocols for Proteomic Sample Preparation in the Low Microgram Range. *J. Proteome Res.* **16**, 4060–4072 (2017).
241. Wardlaw, J. M. *et al.* Blood-brain barrier failure as a core mechanism in cerebral small vessel disease and dementia: evidence from a cohort study. *Alzheimer's Dement.* **13**, 634–643 (2017).
242. van den Kerkhof, M. *et al.* Blood-Brain Barrier Integrity Decreases With Higher Blood Pressure: A 7T DCE-MRI Study. *Hypertension* **81**, 2162–2172 (2024).
243. Lee, M.-H. *et al.* Microvascular Injury in the Brains of Patients with Covid-19. *N. Engl. J. Med.* **384**, NEJMc2033369 (2020).
244. Greene, C. *et al.* Blood–brain barrier disruption and sustained systemic inflammation in individuals with long COVID-associated cognitive impairment. *Nat. Neurosci.* **27**, 421 (2024).
245. Sweeney, M. D., Zhao, Z., Montagne, A., Nelson, A. R. & Zlokovic, B. V. Blood-brain barrier: From physiology to disease and back. *Physiological Reviews* vol. 99 21–78 (2019).
246. Vilar, R., Fish, R. J., Casini, A. & Neerman-Arbez, M. Fibrin(ogen) in human disease: both friend and foe. *Haematologica* **105**, 284–296 (2020).
247. Ryu, J. K. *et al.* Blood coagulation protein fibrinogen promotes autoimmunity and demyelination via chemokine release and antigen presentation. *Nat. Commun.* **6**, (2015).
248. Bucay, I. *et al.* Physical Determinants of Fibrinolysis in Single Fibrin Fibers. *PLoS One* **10**, e0116350 (2015).
249. Eyisoylu, H., Hazekamp, E. D., Cruts, J., Koenderink, G. H. & de Maat, M. P. M.

Flow affects the structural and mechanical properties of the fibrin network in plasma clots. *J. Mater. Sci. Mater. Med.* **35**, 1–10 (2024).
250. Hulshof, A. M., Hemker, H. C., Spronk, H. M. H., Henskens, Y. M. C. & Cate, H. Ten. Thrombin-Fibrin(ogen) Interactions, Host Defense and Risk of Thrombosis. *Int. J. Mol. Sci.* **22**, 1–15 (2021).
251. Tzioras, M. *et al.* Human astrocytes and microglia show augmented ingestion of synapses in Alzheimer's disease via MFG-E8. *Cell Reports Med.* **4**, (2023).
252. Sokolova, D. *et al.* Astrocyte-derived MFG-E8 facilitates microglial synapse elimination in Alzheimer's disease mouse models. *bioRxiv Prepr. Serv. Biol.* (2024) doi:10.1101/2024.08.31.606944.
253. Wagner, J. *et al.* Medin co-aggregates with vascular amyloid-β in Alzheimer's disease. *Nat. 2022 6127938* **612**, 123–131 (2022).
254. Uchiyama, A. *et al.* Protective Effect of MFG-E8 after Cutaneous Ischemia–Reperfusion Injury. *J. Invest. Dermatol.* **135**, 1157–1165 (2015).
255. Matsuda, A. *et al.* Milk fat globule–EGF factor VIII ameliorates liver injury after hepatic ischemia-reperfusion. *J. Surg. Res.* **180**, e37–e46 (2013).
256. Deroide, N. *et al.* MFGE8 inhibits inflammasome-induced IL-1β production and limits postischemic cerebral injury. *J. Clin. Invest.* **123**, 1176–1181 (2013).
257. Moser, M., Nieswandt, B., Ussar, S., Pozgajova, M. & Fässler, R. Kindlin-3 is essential for integrin activation and platelet aggregation. *Nat. Med. 2008 143* **14**, 325–330 (2008).
258. Bialkowska, K. *et al.* The Integrin Co-activator Kindlin-3 Is Expressed and Functional in a Non-hematopoietic Cell, the Endothelial Cell. *J. Biol. Chem.* **285**, 18640 (2010).
259. Wen, L. *et al.* Kindlin-3 recruitment to the plasma membrane precedes high-affinity β2-integrin and neutrophil arrest from rolling. *Blood* **137**, 29–38 (2021).
260. Dudiki, T. *et al.* Microglia control vascular architecture via a TGFβ1 dependent paracrine mechanism linked to tissue mechanics. *Nat. Commun. 2020 111* **11**, 1–16 (2020).
261. Moshayedi, P. *et al.* The relationship between glial cell mechanosensitivity and foreign body reactions in the central nervous system. *Biomaterials* **35**, 3919–3925 (2014).
262. Bollmann, L. *et al.* Microglia mechanics: Immune activation alters traction forces and durotaxis. *Front. Cell. Neurosci.* **9**, 1–16 (2015).
263. Hu, J. *et al.* Microglial Piezo1 senses Aβ fibril stiffness to restrict Alzheimer's disease. *Neuron* **111**, 15-29.e8 (2023).
264. Moser, M. *et al.* Kindlin-3 is required for beta2 integrin-mediated leukocyte adhesion to endothelial cells. *Nat. Med.* **15**, 300–305 (2009).
265. Ferkowicz, M. J. *et al.* CD41 expression defines the onset of primitive and definitive hematopoiesis in the murine embryo. *Development* **130**, 4393–4403 (2003).
266. Oksala, N. *et al.* Kindlin 3 (FERMT3) is associated with unstable atherosclerotic plaques, anti-inflammatory type II macrophages and upregulation of beta-2 integrins in all major arterial beds. *Atherosclerosis* **242**, 145–154 (2015).
267. Sato, Y. *et al.* Proportion of fibrin and platelets differs in thrombi on ruptured and eroded coronary atherosclerotic plaques in humans. *Heart* **91**, 526–530 (2005).
268. Davide, D. *et al.* Human frataxin, the Friedreich ataxia deficient protein, interacts with mitochondrial respiratory chain. *Cell Death Dis. 2023 1412* **14**, 1–14 (2023).
269. Karthikeyan, G. *et al.* Reduction in frataxin causes progressive accumulation of mitochondrial damage. *Hum. Mol. Genet.* **12**, 3331–3342 (2003).

270. Sciarretta, F. *et al.* Frataxin deficiency shifts metabolism to promote reactive microglia via glucose catabolism. *Life Sci. Alliance* **7**, e202402609 (2024).
271. Sigel, E. & Steinmann, M. E. Structure, Function, and Modulation of GABAA Receptors. *J. Biol. Chem.* **287**, 40224 (2012).
272. Mann, E. O., Kohl, M. M. & Paulsen, O. Distinct Roles of GABAA and GABAB Receptors in Balancing and Terminating Persistent Cortical Activity. *J. Neurosci.* **29**, 7513–7518 (2009).
273. Khodaie, B., Edelmann, E. & Leßmann, V. Distinct GABAergic modulation of timing-dependent LTP in CA1 pyramidal neurons along the longitudinal axis of the mouse hippocampus. *iScience* **27**, 109320 (2024).
274. Olsen, R. W. & Sieghart, W. GABAA Receptors: Subtypes Provide Diversity of Function and Pharmacology. *Neuropharmacology* **56**, 141 (2008).
275. Asada, H. *et al.* Cleft palate and decreased brain gamma-aminobutyric acid in mice lacking the 67-kDa isoform of glutamic acid decarboxylase. *Proc. Natl. Acad. Sci. U. S. A.* **94**, 6496–6499 (1997).
276. Kanaani, J., Kolibachuk, J., Martinez, H. & Baekkeskov, S. Two distinct mechanisms target GAD67 to vesicular pathways and presynaptic clusters. *J. Cell Biol.* **190**, 911–925 (2010).
277. Kanaani, J. *et al.* A combination of three distinct trafficking signals mediates axonal targeting and presynaptic clustering of GAD65. *J. Cell Biol.* **158**, 1229–1238 (2002).
278. Tian, N. *et al.* The role of the synthetic enzyme GAD65 in the control of neuronal gamma-aminobutyric acid release. *Proc. Natl. Acad. Sci. U. S. A.* **96**, 12911–12916 (1999).
279. Monteiro, P. & Feng, G. SHANK proteins: roles at the synapse and in autism spectrum disorder. *Nat. Rev. Neurosci. 2017 183* **18**, 147–157 (2017).
280. Mao, W. *et al.* Shank1 regulates excitatory synaptic transmission in mouse hippocampal Parvalbumin-expressing inhibitory interneurons. *Eur. J. Neurosci.* **41**, 1025 (2015).
281. Marazuela, P. *et al.* MFG-E8 (LACTADHERIN): a novel marker associated with cerebral amyloid angiopathy. *Acta Neuropathol. Commun.* **9**, 1–17 (2021).
282. Wagner, J. *et al.* Medin co-aggregates with vascular amyloid-β in Alzheimer's disease. *Nat. 2022 6127938* **612**, 123–131 (2022).
283. Zhang, X., Wang, L. P., Ziober, A., Zhang, P. J. & Bagg, A. Ionized Calcium Binding Adaptor Molecule 1 (IBA1). *Am. J. Clin. Pathol.* **156**, 86–99 (2021).
284. Hopperton, K. E., Mohammad, D., Trépanier, M. O., Giuliano, V. & Bazinet, R. P. Markers of microglia in post-mortem brain samples from patients with Alzheimer's disease: a systematic review. *Mol. Psychiatry 2018 232* **23**, 177–198 (2017).
285. Satoh, J. ichi *et al.* TMEM119 marks a subset of microglia in the human brain. *Neuropathology* **36**, 39–49 (2016).
286. Meller, J. *et al.* Integrin-Kindlin3 requirements for microglial motility in vivo are distinct from those for macrophages. *JCI Insight* **2**, (2017).
287. Liu, H. *et al.* Macrophage migration and phagocytosis are controlled by Kindlin-3 link to cytoskeleton. *J. Immunol.* **204**, 1954 (2020).
288. Chen, Z. *et al.* Microglial displacement of inhibitory synapses provides neuroprotection in the adult brain. *Nat. Commun.* **5**, 4486 (2014).
289. Mao, Z., Bonni, A., Xia, F., Nadal-Vicens, M. & Greenberg, M. E. Neuronal activity-dependent cell survival mediated by transcription factor MEF2. *Science* **286**, 785–790 (1999).

290. Zhao, R. *et al.* Activity disruption causes degeneration of entorhinal neurons in a mouse model of Alzheimer's circuit dysfunction. *Elife* **11**, e83813 (2022).
291. Murase, S., Owens, D. F. & McKay, R. D. In the newborn hippocampus, neurotrophin-dependent survival requires spontaneous activity and integrin signaling. *J. Neurosci.* **31**, 7791–7800 (2011).
292. Wong, F. K. & Marín, O. Developmental Cell Death in the Cerebral Cortex. *Annu. Rev. Cell Dev. Biol.* **35**, 523–542 (2019).
293. DuBose, N. G., DeJonge, S. R., Jeng, B. & Motl, R. W. Vascular dysfunction in multiple sclerosis: Scoping review of current evidence for informing future research directions. *Mult. Scler. Relat. Disord.* **78**, 104936 (2023).
294. Zheng, P., Pilutti, L. A., DuBose, N. G. & Motl, R. W. Vascular function and cognition in persons with multiple sclerosis: Preliminary examination. *Mult. Scler. Relat. Disord.* **71**, 104578 (2023).
295. Winder, N. R., Reeve, E. H. & Walker, A. E. Large artery stiffness and brain health: insights from animal models. *Am. J. Physiol. - Hear. Circ. Physiol.* **320**, H424 (2020).
296. Muhire, G. *et al.* Arterial Stiffness Due to Carotid Calcification Disrupts Cerebral Blood Flow Regulation and Leads to Cognitive Deficits. *J. Am. Hear. Assoc. Cardiovasc. Cerebrovasc. Dis.* **8**, e011630 (2019).
297. Heider, J. *et al.* Defined co-cultures of glutamatergic and GABAergic neurons with a mutation in DISC1 reveal aberrant phenotypes in GABAergic neurons. *BMC Neurosci.* **25**, 1–20 (2024).